An Investigation of Singly and Doubly Tagged Photon-Photon Scattering Using the OPAL Detector at LEP

Edward Allen McKigney
Department of Physics and Astronomy
University College London

Submitted to the University of London
for the degree of
Doctor of Philosophy
1998

Abstract

The calibration of the OPAL Far Forward Monitor (FFM) system is described. This system consists of a set of four small electro-magnetic calorimeters with an angular acceptance of approximately 5 to 15 mrad. The FFM system is used for the OPAL online luminosity measurement and to tag electrons at small angles. Doubly Tagged Two-Photon events are selected from a sample of Singly Tagged Two-Photon events measured with the OPAL detector. This data was taken during 1997 when LEP operated with a beam energy of 91.5 GeV. A measurement of the cross section for the process $e^+e^- \rightarrow e^+e^- \ + \ \text{Hadrons}$ is made, with $\overline{Q}^2 = 20.4$ GeV^2 and $\overline{P}^2 = 0.27$ GeV^2. The measured cross section is $1.39 \pm 0.77(\text{stat}) \ \pm^{0.18}_{0.14} \ (\text{syst})$ pb, which is consistent with theoretical expectations. With 350 pb^{-1} and the upgraded FFMs, a statistical error of 10% and a systematic error of less than 10% will be possible for this measurement.

This thesis is dedicated to my family, without whose
love and support it would not have been possible.

Acknowledgements

For a genorous grant, I am indebted to the Elizabeth Spreadbury fund. This assistance was crucial in allowing me to pursue my degree.

I would like to thank my grandparents; Frank Allen, Mary Allen, Cliff McKigney, and Grace McKigney, for their love and support througout my life. We have had a special relationship, and I would not be the person I am without them. I would especially like to remember Grandpa Frank and Grandma Grace, who will not be able to celebrate with me. I hope that they are proud, though.

I would also like to thank my mother and stepfather; Brenda and Pierre Trolin, who have given me a loving home when I needed, and the support to leave it and seek my fortunes in the wide world.

Thanks to my dad, Thomas McKigney, for his love, which was always appreciated.

For their warmth and caring, thanks to my aunt Janice Sibley, and cousins Tasha Sibley, Shalimar Sibley, and Bob Bartlow.

Especially important to me has been the love of my wife, Elizabeth Eastwood. She has put up with the late nights, the early mornings, and phone calls at all hours. When there seemed to be nothing but problems, she reminded me that I enjoy my work. I couldn't have done it without you, and I love you dearly.

Elizabeth's family, Peter, Janice, Helen and Joe have been generous with their hospitality and made me feel welcome to both their home and their family.

My advisor, David Miller, has been thoroughly supportive, and provided insight and guidance without which this thesis certainly would not exist.

While studying physics, I have had the opportunity to meet some remarkable people who have taken the time to share their skills. From my undergraduate days, I would like to thank Jim Branson, Hans Kobrak, Wayne Vernon, and Bob Swanson. As a graduate student, I would like to thank the members of the UCL/Brunel OPAL HEP group; Peter Sherwood, Jan Lauber, Peter Clarke, David Miller, Brian Anderson, Derek Attree, Dominic Hayes, Jason Ward, Steve Betts, Max Sang, Bruce Kennedy, and Tony Rooke. In OPAL, I have learned a great deal from Austin Ball, Penny Estabrooks, Dick Kellogg, and Richard Nisius. Bernd Surrow has done a wonderful job absorbing all the details of the FFMs in a short time, and been extremely flexible about my time constraints. David Chrisman and Luis Del Pozo were both great

to work with in my guise as a system manager. I would also like to thank the other members of the OPAL collaboration, too numerous to name, who made my time at CERN both stimulating and enjoyable.

Mette Stuwe has been an incredible help with living in France, and has certainly gone beyond the call of duty in keeping me out of trouble.

Aaron Dominguez, Ian Fisk, and Chris Tully have been steadfast friends, and have improved both my physics and my life.

Julie Abo has provided excellent perspective for us all, and always been a joy to talk to. David and Shannon McNally have provided many enjoyable evenings, not the least of which was my last living in France.

Finally, I would like to thank all my friends who have kept in touch in spite of vast distances and time differences; Joe Ahadian, Matt Harrington, Jason Jones, Julie Wolfe, Nick Doran, and Roy Hobbes.

CONTENTS

1. *Introduction* 11

2. *Theory* 14
   - 2.1 Kinematics of $e^+e^- \rightarrow e^+e^-X$ and the Equivalent Photon Approximation 14
   - 2.2 The Structure Function Formalism 20
   - 2.3 Theoretical Predictions for the Structure Functions 21
     - 2.3.1 Photon Structure Functions at Low Q^2 22
     - 2.3.2 Evolution of the Structure Functions with Q^2 24
     - 2.3.3 Specific Photon Structure Function Models 25
     - 2.3.4 Evolution of the Structure Functions with P^2 27

3. *The LEP Collider and The OPAL Detector* 34
   - 3.1 The LEP Collider 34
   - 3.2 The OPAL Coordinate System 37
   - 3.3 The OPAL Detector 39
     - 3.3.1 The Central Tracking System 41
     - 3.3.2 Time Of Flight System and Tile Endcap System 43
     - 3.3.3 Electromagnetic Presampler and Calorimeter 44
     - 3.3.4 The Hadronic Calorimeter 46
     - 3.3.5 Muon Chambers 46
     - 3.3.6 The Forward Tagging Detectors 46
     - 3.3.7 Run Control and Data Acquisition System 50
     - 3.3.8 Trigger 52
     - 3.3.9 Online Computing 53

4. *Calibration of the Far Forward Monitors* 55
   - 4.1 Description of the Far Forward Monitors 55
   - 4.2 Online Luminosity Measurement 63
   - 4.3 Luminosity and Calibration Triggers 64

4.4 PMT Gain Balancing Procedure 68
4.5 Detector Simulation 71
4.6 Energy Calibration Procedure 79
4.7 Reconstruction of the Momentum of the Initial Electron 86
4.8 Machine Background 90
4.9 Calibration Using Data 99
  4.9.1 Stability of the Acceptance 104
  4.9.2 Detector Position Estimation 104

5. Target Virtuality Effects in $\gamma\gamma^*$ Scattering 126
5.1 Outline of the Measurement 126
5.2 Doubly Tagged Event Selection 127
5.3 Background Estimate 128
5.4 Acceptance Correction 130
5.5 Result 134

6. Conclusions 139

A. Paper presented at CHEP '97 143

Appendix 143

LIST OF FIGURES

1.1 Photon Interactions in Classical EM and QED 12
1.2 Particle Production by $\gamma\gamma$ Interactions in QED 12

2.1 The Kinematics of $\gamma\gamma$ Scattering at an e^+e^- Collider 17
2.2 The Real Photon Structure Function 26
2.3 The Virtual Photon Structure Function 31
2.4 u Quark Distribution For Several Models 32
2.5 The Virtual Photon Structure Function from the Quark-Parton Model 33

3.1 The CERN Accelerator Complex 35
3.2 Cutaway View of the OPAL Detector at LEP 38
3.3 Cross Section View of the OPAL Detector 40
3.4 The Forward Region in OPAL 48
3.5 OPAL DAQ 51

4.1 FFM Schematic 57
4.2 FFM Photograph 1 59
4.3 FFM Photograph 2 60
4.4 BHLUMI Bhabha Distributions 66
4.5 FFM Region 74
4.6 FFM in Geant 78
4.7 Pedestal Subtracted ADC Count Distribution 82
4.8 Pedestal Subtracted ADC Count Sums 83
4.9 Reconstructed Energy Distributions 84
4.10 Reconstructed Energy and Background 85
4.11 Asymmetry and Position Correlations 88
4.12 Off-momentum Energy Distributions from TURTLE 93
4.13 x and y Distributions of Off-momentum Particles from TURTLE 94
4.14 FFM Energy Distributions for Random Triggers, Period 85 . . 95
4.15 FFM Energy Distributions for Random Triggers, Period 86a . 96

4.16 FFM Energy Distributions for Random Triggers, Period 86b . 97
4.17 FFM Energy Distributions for Random Triggers, Period 88 . . 98
4.18 Calibrated Energy Distributions for Period 85 100
4.19 Calibrated Energy Distributions for Period 86a 101
4.20 Calibrated Energy Distributions for Period 86b 102
4.21 Calibrated Energy Distributions for Period 88 103
4.22 σ'_{FFM} vs OPAL Run Number 105
4.23 Distribution of σ'_{FFM} 106
4.24 $\mathrm{X}_{\mathrm{asym}}$ Distributions 113
4.25 $\mathrm{Y}_{\mathrm{asym}}$ Distributions 114
4.26 $\mathrm{Z}_{\mathrm{asym}}$ Distributions 115
4.27 Asymmetry Correlations for MC and Data 116
4.28 Correlation Between $\mathrm{X}_{\mathrm{asym}}$ and $\mathrm{Y}_{\mathrm{asym}}$ 117
4.29 Correlation Between $\mathrm{X}_{\mathrm{asym}}$ and $\mathrm{Z}_{\mathrm{asym}}$ 118
4.30 Result of Variation of x Position 120
4.31 Result of Variation of y Position 121
4.32 Schematic of Module Misalignment 123
4.33 Beam Pipe Position Variation 124

5.1 Module Acceptance, without and with $\mathrm{Y}_{\mathrm{asym}}$ cut 135
5.2 Module Acceptance, Systematic Variations 136

LIST OF TABLES

4.1 HV Gain Data 70
4.2 Gain Balancing Result 70
4.3 Energy to ADC Count Conversion Constants 77
4.4 Tuned PMT Gain Constants 79
4.5 Results of Position Variation in Monte Carlo 111
4.6 Positions of the FFM Modules 123
4.7 Values of the Cross Talk Parameters 125
4.8 Figure of Merit for Parameter Variations 125

5.1 Event Selection Cuts 128
5.2 Luminosity 129
5.3 Definition of Systematic Error Variations 137
5.4 Result of Systematic Error Variations 137
5.5 Comparison of Data and Monte Carlo 138

1. INTRODUCTION

In Classical Electrodynamics, electromagnetic waves obey Maxwell's equations given in 1.1, where E is the electric field and B is the magnetic field. Maxwell's Equations are linear partial differential equations. Solutions of equations of this type obey the superposition principle; the sums of solutions are also solutions. Since light is a manifestation of electromagnetic radiation, this implies that light does not interact with light. The variable ρ is the electric charge density and j is the electric current density. It follows that electromagnetic fields arise in the presence of electric charge.

$$\begin{aligned}
\nabla \cdot E &= \rho \qquad (1.1)\\
\nabla \times E + \frac{\partial B}{\partial t} &= 0\\
\nabla \cdot B &= 0\\
\nabla \times B - \frac{\partial E}{\partial t} &= j
\end{aligned}$$

The quantization of Maxwell's equations leads to Quantum Electrodynamics(QED). In this case, the electromagnetic field is quantized, and light is considered as an ensemble of particles, called photons. Using Feynman diagrams, the situations in Classical Electrodynamics and Quantum Electrodynamics (QED) can be illustrated. The first diagram in Figure 1.1 is

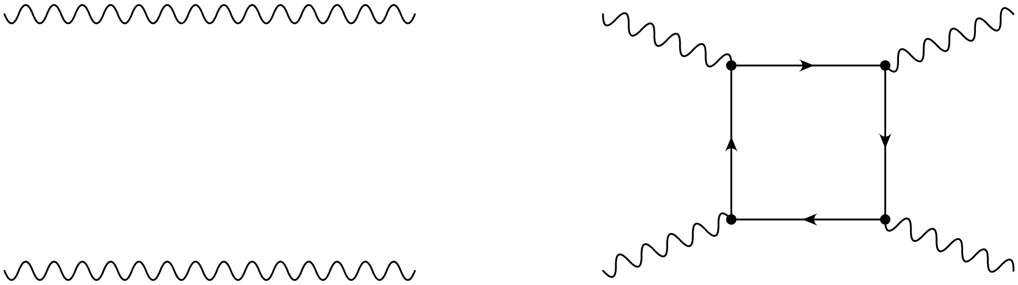

Fig. 1.1: Interactions of Photons in Classical Electrodynamics and Quantum Electrodynamics

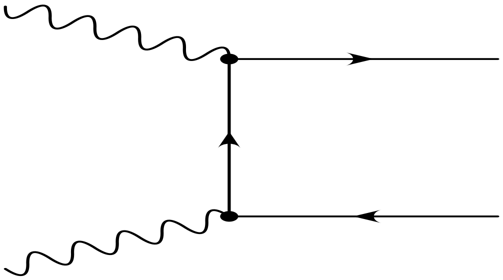

Fig. 1.2: Particle Production by $\gamma\gamma$ interactions in QED

allowed in both Classical Electrodynamics and QED. In this case, two photons propagate in space and time without interacting. The second diagram arises only in QED and is a correction to the first diagram. In this case, the photons couple to the charge of some intermediate particle, and scatter. QED thus allows light by light scattering. The scattering of light by light is related to the production particles in photon-photon interactions by the optical theorem. This type of particle production is shown in Figure 1.2. The case where the intermediate particle is an electron or positron was calculated by Breit and Wheeler in 1934 [1]. The production of e^+e^- pairs through the interaction of real photons was recently observed by E144 [2] at SLAC.

The diagram of Figure 1.2 can be thought of in a different way. One photon fluctuates into a virtual particle-antiparticle pair, and the other photon interacts with that particle-antiparticle system. Since the photon couples to any particle with an electric charge, the particle-antiparticle system can be composed of charged leptons or quarks. In this picture, a photon develops substructure through fluctuations into virtual particle-antiparticle pairs.

The study of the leptonic substructure of the photon provides a verification of the ideas of QED. The study of the hadronic substructure provides a testing ground for theories of the strong interaction, such as Quantum Chromodynamics (QCD). Deep Inelastic Scattering (DIS) is the scattering of a probe from a target which results in the breakup of the target, providing information about the structure of the target. DIS has proven an important tool in the study of the structure of hadrons. In this thesis, DIS will be used to probe the hadronic structure of the virtual photon. This has been done previously by Pluto [3, 4] and TPC/2γ [5].

The thesis is organized as follows; Chapter 2 introduces the theoretical background for the study. Chapter 3 discusses the experimental apparatus. The Far Forward Monitor (FFM) system, which was used to tag electrons and positrons at very small angles, is described in Chapter 4. Chapter 5 describes the measurement of $e^+e^- \rightarrow e^+e^- +$ Hadrons using the FFM system. Conclusions are given in Chapter 6.

2. THEORY

2.1 Kinematics of $e^+e^- \to e^+e^-X$ and the Equivalent Photon Approximation

The process shown in Figure 2.1 allows the study of photon-photon interactions at an $\mathrm{e}^+\mathrm{e}^-$ collider. The particles entering the diagram from the left are the beam particles; the incoming momenta are p_1 and p_2. In order to simplify the exposition, the term electron will generically refer to either electrons or positrons, except when the distinction is important, and such cases will be explicitly identified. The scattering angles of the outgoing electrons are θ_1 and θ_2, and the outgoing four-momenta are p_1' and p_2'. In order to simplify the following expressions, the coordinate system is chosen so that p_1' lies in the xz plane. The variable Φ is the angle between the scattering planes of the electrons. The photons radiated from the scattered electrons have momenta q_1 and q_2. The invariant mass of the final state of the $\gamma\gamma$ interaction is W. From knowledge of the beam energy and the assumption that the beams collide head-on, combined with energy and momentum conservation, several important expressions relating to the kinematics of this reaction can be derived. Equations 2.1 through 2.4 decompose the four-momenta using Cartesian coordinates in the laboratory reference frame and including the energy as the last component of the vector while disregarding the electron mass.

$$
\begin{aligned}
p_1 &= E^{\text{Beam}}(0, 0, -1, 1) && (2.1)\\
p_2 &= E^{\text{Beam}}(0, 0, 1, 1) && (2.2)\\
p_1' &= E_1'(\sin\theta_1, 0, -\cos\theta_1, 1) && (2.3)\\
p_2' &= E_2'(\sin\theta_2\cos\Phi, \sin\theta_2\sin\Phi, \cos\theta_2, 1) && (2.4)
\end{aligned}
$$

Using momentum conservation, the four-momenta of the radiated photons are

$$
\begin{aligned}
q_1 &= (-E_1'\sin\theta_1, 0, -E^{\text{Beam}} + E_1'\cos\theta_1, E^{\text{Beam}} - E_1') && (2.5)\\
q_2 &= (-E_2'\sin\theta_2\cos\Phi, -E_2'\sin\theta_2\sin\Phi, E^{\text{Beam}} - E_2'\cos\theta_2, E^{\text{Beam}} - E_2')
\end{aligned}
$$

where Φ is the angle between the electron scattering planes. The invariant masses of the radiated photons are, using $q^2 = E^2 - \vec{q}^2$ where $\vec{q}$ is the particle three-momentum,

$$
\begin{aligned}
q_1^2 &= -2E^{\text{Beam}}E_1'(1-\cos\theta_1) && (2.6)\\
q_2^2 &= -2E^{\text{Beam}}E_2'(1-\cos\theta_2) && (2.7)
\end{aligned}
$$

The invariant mass squared of the final state of the $\gamma\gamma$ scattering is, using energy and momentum conservation,

$$\begin{aligned} W^2 &= (q_1 + q_2)^2 \\ &= 2q_1 \cdot q_2 + q_1^2 + q_2^2 \\ &= 4(E^{\text{Beam}} - E_1')(E^{\text{Beam}} - E_2') - \\ &\quad 2E_1'E_2'(1 - \cos\theta_1 \cos\theta_2 + \sin\theta_1 \sin\theta_2 \cos\Phi) \end{aligned} \tag{2.8}$$

Note that the kinematics of this reaction are overconstrained, so that one of p_1', p_2' and W does not need to be measured, provided that the others are well measured. From an experimental point of view, it is useful to find an expression for the cross section of the process shown in Figure 2.1 that separates the physics of the electron-photon vertices, which can be calculated in QED, from the physics of the two-photon interaction. This has been done by a number of authors, and a good review can be found in Budnev et al. [6]. The result is

$$\begin{aligned} \mathrm{d}^6\sigma &= \frac{\alpha^2}{16\pi^4 q_1^2 q_2^2} \left[\frac{(q_1q_2)^2 - q_1^2q_2^2}{(p_1p_2)^2 - m_e^4}\right]^{1/2} \Big[4\rho_1^{++}\rho_2^{++}\sigma_{TT} \\ &\quad +2|\rho_1^{+-}\rho_2^{+-}|\tau_{TT}\cos 2\tilde{\phi} + 2\rho_1^{++}\rho_2^{00}\sigma_{TS} + 2\rho_1^{00}\rho_2^{++}\sigma_{ST} \\ &\quad +\rho_1^{00}\rho_2^{00}\sigma_{SS} - 8|\rho_1^{+0}\rho_2^{+0}|\tau_{TS}\cos\tilde{\phi} + A\tau_{TT}^a + B\tau_{TS}^a\Big] \frac{\mathrm{d}^3p_1'\mathrm{d}^3p_2'}{E_1'E_2'} \end{aligned} \tag{2.9}$$

The variable $\tilde{\phi}$ is the angle between the electron scattering planes in the $\gamma\gamma$ center of mass frame. Equation 2.9 was obtained after integrating over the phase space of the outgoing particles in the $\gamma\gamma$ final state, which implies that information on the structure of the final state is not included in this

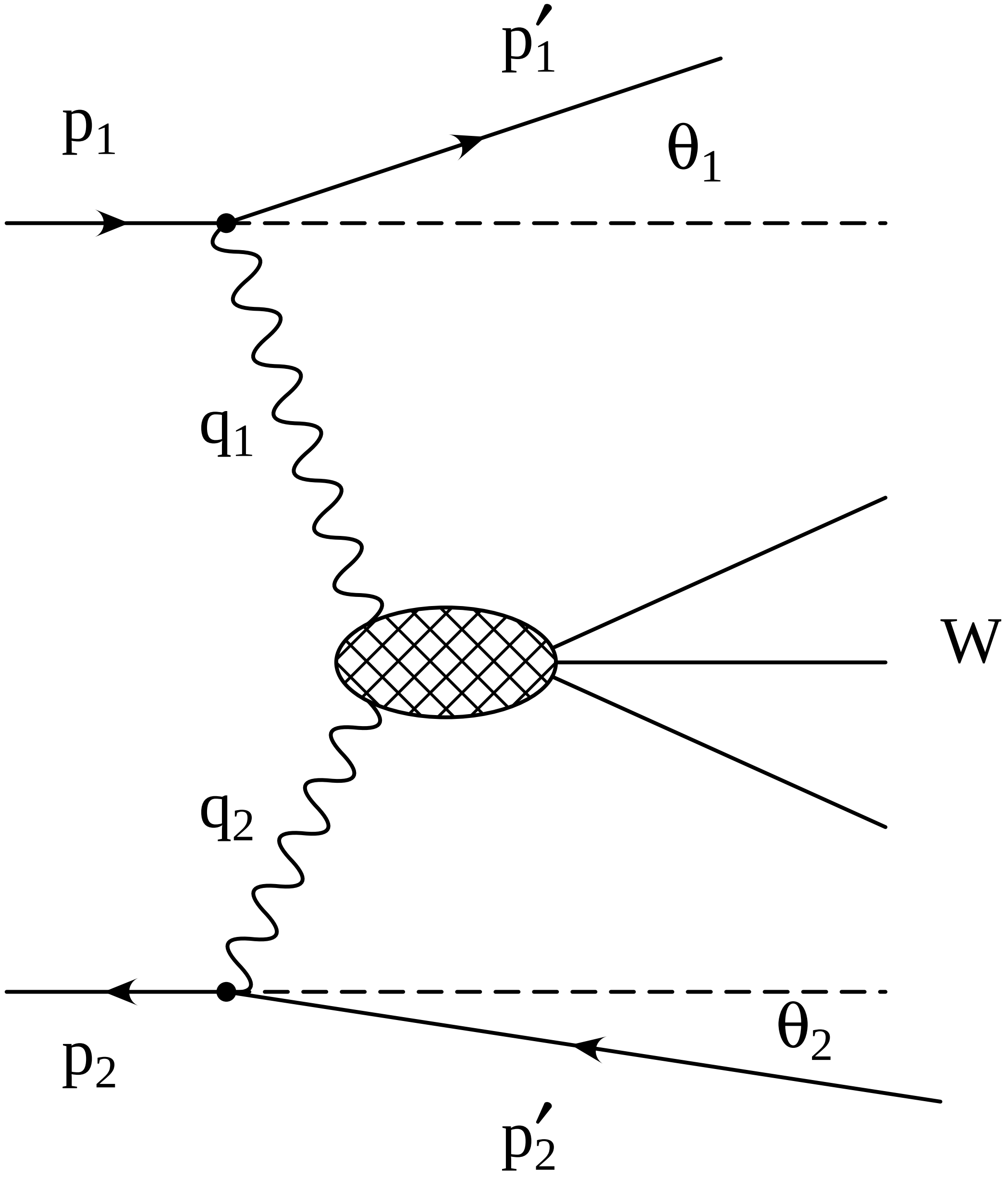

Fig. 2.1: The kinematics of $\gamma\gamma$ scattering at an e^+e^- collider.

expression. The overall differential cross section is decomposed into the cross sections, $\sigma_{ab}(a,b=S,T)$ and $\tau_{ab}(a,b=S,T)$ for the scattering of photons with various helicities, and factors, ρ_i^{ab}, related to the density of the various photon helicity states generated by the electron beams. The subscripts S (Scalar) and T (Transverse) denote photons with helicity zero and helicity +/-1, respectively. The density matrices can be written in terms of the kinematic variables, as in Equations 2.10 through 2.18.

$$
\begin{aligned}
2\rho_1^{++} = 2\rho_1^{--} &= X^{-1}(2p_1q_2 - q_1q_2)^2 + 1 + 4m_e^2/q_1^2 && (2.10)\\
\rho_1^{00} &= X^{-1}(2p_1q_2 - q_1q_2)^2 - 1 && (2.11)\\
8|\rho_1^{+0}\rho_2^{+0}|\cos\tilde{\phi} &= 4X^{-1}(2p_1q_2 - q_1q_2)(2p_2q_1 - q_1q_2)C\left[q_1^2q_2^2\right]^{-\frac{1}{2}} && (2.12)\\
C &= -(2p_1 - q_1)(2p_2 - q_2) + && (2.13)\\
&\quad X^{-1}(q_1q_2)(2p_1q_2 - q_1q_2)(2p_2q_1 - q_1q_2) &&\\
2|\rho_1^{+-}\rho_2^{+-}|\cos 2\tilde{\phi} &= C^2/(q_1^2q_2^2) - 2(\rho_1^{++} - 1)(\rho_2^{++} - 1) && (2.14)\\
|\rho_2^{ab}| &= |\rho_1^{ab}(1 \leftrightarrow 2)| && (2.15)\\
|\rho_i^{+-}| &= \rho_i^{++} - 1 && (2.16)\\
|\rho_i^{+0}| &= \sqrt{(\rho_i^{00} + 1)|\rho_i^{+-}|} && (2.17)\\
X &= \frac{1}{4}\left[W^4 - 2W^2(q_1^2 + q_2^2) + (q_1^2 - q_2^2)^2\right] && (2.18)
\end{aligned}
$$

For the case of unpolarized beams, the factors A and B are both zero.

In order to emphasize the similarity between the process shown in Figure 2.1 and deep-inelastic scattering of an electron beam from a hadron beam, the Equivalent Photon Approximation (EPA) can be used [6]. The basic idea of the EPA is to consider the electromagnetic field of a charged particle as an aggregate of photons with some energy spectrum. These equivalent photons then participate directly in the scattering process. In the case discussed here, each electron beam acts as a source of photons. Equation 2.9 is rewritten as Equation 2.19, introducing the transverse-transverse photon luminosity function, $\mathrm{L}_{\gamma\gamma}^{\mathrm{TT}}$.

$$\begin{aligned}\frac{\mathrm{d}^5\sigma}{\mathrm{d}\omega_1\ \mathrm{d}\omega_2\ \mathrm{d}\cos\theta_1\ \mathrm{d}\cos\theta_2\ \mathrm{d}\Phi} &= \frac{\mathrm{d}^5\mathrm{L}_{\gamma\gamma}^{\mathrm{TT}}}{\mathrm{d}\omega_1\ \mathrm{d}\omega_2\ \mathrm{d}\cos\theta_1\ \mathrm{d}\cos\theta_2\ \mathrm{d}\Phi} \\ \times \Big[\sigma_{TT}(q_1^2, q_2^2, W) + \epsilon\sigma_{ST}(q_1^2, q_2^2, W)&\frac{1}{2}\epsilon_1\epsilon_2\tau_{TT}(q_1^2, q_2^2, W)\cos\widetilde{2\phi}\Big]\end{aligned} \tag{2.19}$$

$$\frac{\mathrm{d}^5\mathrm{L}_{\gamma\gamma}^{\mathrm{TT}}}{\mathrm{d}\omega_1\ \mathrm{d}\omega_2\ \mathrm{d}\cos\theta_1\ \mathrm{d}\cos\theta_2\ \mathrm{d}\Phi} = \frac{\alpha^2}{16\pi^3}\frac{E_1'E_2'}{q_1^2q_2^2}\sqrt{X}4\rho_1^{++}\rho_2^{++} \tag{2.20}$$

$$\begin{aligned}\epsilon &= \rho_1^{00}/(2\rho_1^{++}) \qquad (2.21)\\ \epsilon_1 &= |\rho_1^{+-}|/\rho_1^{++}\\ \epsilon_2 &= |\rho_2^{+-}|/\rho_2^{++}\end{aligned}$$

Equation 2.19 neglects the terms containing cross sections for scalar target photons. This approximation is expected to be good for the low target virtualities studied in this thesis [6].

Using the EPA, the angular and energy distribution of equivalent photons from an electron beam can be written as [7]

$$\mathrm{d}n = \frac{\alpha}{\pi}\left[1 - \frac{\omega}{E_{\mathrm{Beam}}} + \frac{\omega^2}{2E_{\mathrm{Beam}}^2} - \frac{m_e^2\omega^2}{Q^2E_{\mathrm{Beam}}^2}\right]\frac{\mathrm{d}\omega}{\omega}\frac{\mathrm{d}Q^2}{Q^2} \tag{2.22}$$

where ω is the energy of the emitted photon. Rewriting in terms of the electron scattering angle and neglecting the electron mass, Equation 2.22 becomes

$$\mathrm{d}n = \frac{\alpha}{\pi}\left[1 - \frac{\omega}{E_{\mathrm{Beam}}} + \frac{\omega^2}{2E^2_{\mathrm{Beam}}}\right]\frac{\mathrm{d}\omega}{\omega}\frac{\sin\theta}{1-\cos\theta}\mathrm{d}\theta \tag{2.23}$$

and assuming θ is small,

$$\mathrm{d}n = 2\frac{\alpha}{\pi}\left[1 - \frac{\omega}{E_{\mathrm{Beam}}} + \frac{\omega^2}{2E^2_{\mathrm{Beam}}}\right]\frac{\mathrm{d}\omega}{\omega}\frac{\mathrm{d}\theta}{\theta}. \tag{2.24}$$

2.2 The Structure Function Formalism

The following kinematic variables

$$Q^2 = -q_1^2 \tag{2.25}$$

$$P^2 = -q_2^2 \tag{2.26}$$

$$x = \frac{Q^2}{Q^2+P^2+W^2} \tag{2.27}$$

$$y = 1 - \left(\frac{E_1'}{E^{\mathrm{Beam}}}\right)\cos^2(\theta_1/2) \tag{2.28}$$

and the structure functions

$$\begin{aligned} F_T(x,Q^2,P^2) &= \sigma_{TT}\frac{Q^2}{8\pi^2\alpha x} \\ F_L(x,Q^2,P^2) &= \sigma_{LT}\frac{Q^2}{4\pi^2\alpha} \\ F_X(x,Q^2,P^2) &= (\sigma_{\|}-\sigma_{\perp})\frac{Q^2}{4\pi^2\alpha} \\ \sigma_{\|} &= \sigma_{\mathrm{TT}} + \frac{\tau_{\mathrm{TT}}}{2} \\ \sigma_{\perp} &= \sigma_{\mathrm{TT}} - \frac{\tau_{\mathrm{TT}}}{2} \end{aligned} \tag{2.29}$$

and the more common set

$$\begin{aligned} F_1(x,Q^2,P^2) &= F_T(x,Q^2,P^2) \\ F_2(x,Q^2,P^2) &= 2xF_T(x,Q^2,P^2)+F_L(x,Q^2,P^2) \\ F_3(x,Q^2,P^2) &= F_X(x,Q^2,P^2) \end{aligned} \tag{2.30}$$

are used to rewrite Equation 2.19 as the cross section for deep inelastic electron-photon scattering. This can be done in cases where the equivalent photon approximation is valid, since the EPA decouples the radiation of the target photon from the hard scattering of the target and probe. Removing the EPA factor from Equation 2.19, and substituting the previously defined variables, results in

$$\begin{aligned} \frac{\mathrm{d}\sigma(e\gamma\rightarrow eX)}{\mathrm{d}x\mathrm{d}y\mathrm{d}Q^2\mathrm{d}P^2} &= \frac{8\pi\alpha^2EE_\gamma}{Q^4}\times[(1-y)F_2(x,Q^2,P^2) \\ &\quad +xy^2F_1(x,Q^2,P^2)+(1-y)\epsilon_2F_3(x,Q^2,P^2)\cos2\phi]. \end{aligned} \tag{2.31}$$

2.3 Theoretical Predictions for the Structure Functions

In the Quark-Parton Model (QPM) and Quantum Chromodynamics(QCD), hadrons are assumed to be made up of pointlike constituents called quarks, which photons scatter from incoherently. In these models, the previously defined structure function F_2 can be written as

$$F_2(x)=\sum_i e_i^2xq_i(x) \tag{2.32}$$

in the limit $Q^2\rightarrow\infty$, x fixed. The index i runs over all quarks and antiquarks. The function $q(x)$ is a quark distribution function parametrizing the probability of finding a quark of flavor i carrying a momentum fraction x of the momentum of the hadron.

2.3.1 Photon Structure Functions at Low Q^2

The calculation of hadronic structure functions from first principles is beyond current theoretical understanding, because of the non-perturbative nature of the problem. Perturbative QCD does allow the calculation of the evolution of hadronic structure functions as the scale of the probe Q^2 increases. The approach taken to determining photon structure functions has been to take an input distribution at some scale Q_0^2 and evolve this distribution to higher scales.

Two distinct approaches have been taken with the photon structure function. One approach is to use the Vector Meson Dominance(VMD) model to obtain an input F_2 and then apply the evolution equation. The description of the VMD model given here follows the one given in [8]. The VMD model is based on the observation that the interaction of photons with hadrons is similar to the interaction of hadrons with hadrons. The photon is assumed to fluctuate into a vector meson, which then interacts hadronically. In the VMD model, the cross section for electron-photon scattering can be written as

$$\sigma(e\gamma \to X) = \sum_V \left(\frac{\alpha\pi}{\gamma_V^2}\right) \sigma(eV \to X). \tag{2.33}$$

The coupling factor $\frac{\alpha\pi}{\gamma_V^2}$ is $(2.85 \pm 0.3) \times 10^{-3}$, $(0.4 \pm 0.04) \times 10^{-3}$ and $(0.6 \pm$

0.05) × 10^{-3} for the ρ, ω and ϕ, respectively. Because the ρ coupling is significantly larger than the other two, the approximation is often made that only the ρ contributes. This allows the identification of the photon structure function with the ρ meson structure function;

$$F_2(x,Q^2) = \left(\frac{\alpha\pi}{\gamma^2_{\rho^0}}\right) F_2^{\rho^0}(x,Q^2). \tag{2.34}$$

It is assumed that the ρ structure function is related to the π structure functions by rotational and isospin invariance as

$$F_2^{\rho^0}(x,Q^2) = F^{\pi^0}(x,Q^2) = F^{\pi^-}(x,Q^2) \tag{2.35}$$

The quark composition of the π is

$$F^{\pi^-}(x,Q^2) = x\left(\frac{4}{9}q_{\overline{u}/\pi^-} + \frac{1}{9}q_{d/\pi^-}\right) = \frac{5}{9}xq_{\overline{u}/\pi^-} \tag{2.36}$$

Using the reaction $\pi^- p \to \mu^+\mu^- + X$, $q_{\overline{u}}$ of the pion has been measured to be

$$xq_{\overline{u}/\pi^-}(x) = 0.57x^{0.41}(1-x)^{0.95}. \tag{2.37}$$

It is this quark distribution which is used as input for the GRV [9] photon structure function calculation.

Another approach is to fit an F_2 to low Q^2 measurements of the photon structure function and then evolve to higher Q^2. This approach has been taken in the SaS [10] calculation.

2.3.2 Evolution of the Structure Functions with Q^2

Given the quark distribution functions q_i and gluon distribution g at some scale Q_0^2, the evolution of the distribution functions with Q^2 is governed by the Dokshitzer-Gribov-Lipatov-Altarelli-Parisi (DGLAP) evolution equations;

$$\begin{aligned}\frac{\mathrm{d}q_i^\gamma(x,Q^2)}{\mathrm{d}\log Q^2} &= \frac{\alpha}{2\pi}P_{\gamma q}(\frac{x}{x'}) + \\ &\frac{\alpha_s}{2\pi}\int_x^1 \frac{\mathrm{d}x'}{x'}\left(q_i(x',Q^2)P_{qq}\left(\frac{x}{x'}\right) + g(x',Q^2)P_{qg}\left(\frac{x}{x'}\right)\right) \qquad (2.38)\\ \frac{\mathrm{d}g_i^\gamma(x,Q^2)}{\mathrm{d}\log Q^2} &= \qquad (2.39)\\ &\frac{\alpha_s}{2\pi}\int_x^1 \frac{\mathrm{d}x'}{x'}\left(\sum_i q_i(x',Q^2)P_{gq}\left(\frac{x}{x'}\right) + g(x',Q^2)P_{gg}\left(\frac{x}{x'}\right)\right).\end{aligned}$$

Derivations of the DGLAP equations can be found in a number of books [11, 12]. The functions

$$P_{qq}(z) = \frac{4}{3}\left(\frac{1+z^2}{(1-z)_+}\right) + 2\delta(1-z) \qquad (2.40)$$

$$P_{qg}(z) = \frac{1}{2}(z^2 + (1-z)^2) \qquad (2.41)$$

$$P_{gq}(z) = \frac{4}{3}\frac{1+(1-z)^2}{z} \qquad (2.42)$$

$$\begin{aligned}P_{gg}(z) &= \qquad (2.43)\\ &6\left(\frac{1-z}{z} + \frac{z}{(1-z)_+} + z(1-z)\right) + (\frac{11}{2} - \frac{n_f}{3})\delta(1-z)\end{aligned}$$

$$P_{\gamma q}(z) = 6\left[z^2 + (1-z)^2\right] \qquad (2.44)$$

are called splitting functions. The splitting functions are the probability of finding a parton inside another parton carrying a fraction z of the parent parton's momentum. The expression $(1-z)_+$ is defined such that

$$\int_0^1 \mathrm{d}z \frac{f(z)}{(1-z)_+} = \int_0^1 \mathrm{d}z \frac{f(z)-f(1)}{1-z} \tag{2.45}$$

and $(1-z)_+ = (1-z)$ for $z < 1$, and n_f is the number of quark flavors.

2.3.3 Specific Photon Structure Function Models

A number of parametrizations of the photon structure function $F_2(x, Q^2)$ have been made by combining a model for the low Q^2 structure of the photon with the DGLAP evolution equations. The structure functions for two different parametrizations are shown in Figure 2.2.

GRV

The GRV calculation [9] of the quark distribution functions used Equation 2.37 to model the quark content of a ρ meson. The calculation was performed both in Leading Order (LO) and in Next to Leading Order (NLO), with the NLO calculation performed in the DIS_γ factorization scheme. The input for the DGLAP evolution equations was taken to be

$$q_i^\gamma(x, Q_0^2) = \kappa \frac{\pi\alpha}{\gamma_{\rho^0}^2} q_{i/\pi}(x, Q_0^2) \tag{2.46}$$

and the constant κ was fit to measured photon structure functions. The values for κ were 2 for LO and 1.6 for NLO. The evolution was started at $Q_0^2 = 0.25$ GeV^2 for the LO calculation and $Q_0^2 = 0.3$ GeV^2 for NLO.

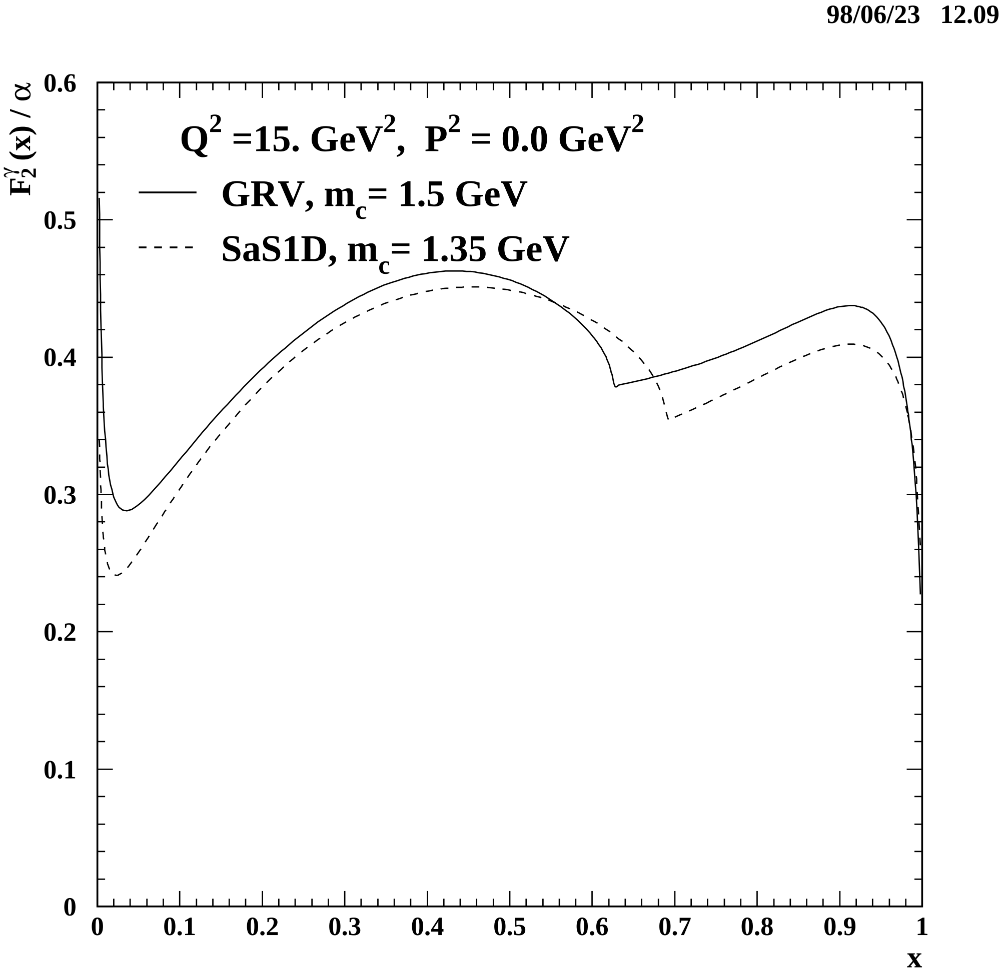

Fig. 2.2: The real photon structure function as a function of x_{Bjorken}.

SaS

The SaS calculation [10] used fits to photon structure function measurements to determine the input quark distributions at Q_0^2. Results in both the $\overline{MS}$ and the DIS_γ factorization schemes were provided. The Q^2 evolution was also started at two different scales, $Q_0 = 0.6$ GeV and $Q_0 = 2.0$ GeV. This yielded a total of four structure function parametrizations, known as SaS 1D, 2D, 1M and 2M. The number refers to the starting evolution scale, with 1 the smaller and 2 the larger. The letter refers to the factorization scheme, M being $\overline{MS}$ and D being DIS_γ.

2.3.4 Evolution of the Structure Functions with P^2

The virtual structure function of the photon $F_2(x, Q^2, P^2)$ is expected to be suppressed with respect to that of the real photon structure function $F_2(x, Q^2)$. This can be seen from a simple argument based on the uncertainty principle. The virtuality P^2 of the photon is the photon's mass squared, so in natural units

$$\begin{aligned} \Delta p \Delta x &= 1 \\ \Delta x &= \frac{1}{P}. \end{aligned} \tag{2.47}$$

For a real photon, Δx is infinite, and the photon is not confined to a particular region of space. The complete substructure implied by QCD can develop. For a photon of virtuality $P = 1$ GeV, $\Delta x = 0.2$ fm, which is smaller than the typical size of a hadron. The full bound state structure thus cannot develop.

This simple argument gives a feeling for why virtual photon structure should be suppressed compared to real photon structure, and several treatments of the virtuality suppression of the photon structure functions exist. The models discussed below all rely on modifying the quark distribution functions of the real photon ($q_i(x, Q^2)$) for the case when the photon is virtual ($q_i(x, Q^2, P^2)$).

Hill Ross

Hill and Ross (HR) have calculated the photon structure function for light quarks in the Quark Parton Model (QPM) [13]. The mean value of Q^2 for a given range of kinematic variables will be denoted by $\overline{Q^2}$ and likewise for P^2. The prediction of HR is shown in Figure 2.5 for the $\overline{Q}^2$ and $\overline{P}^2$ values corresponding to the doubly tagged data presented in this thesis, along with the $\overline{P}^2 = 0$ prediction. For this calulation, the virtual photon structure function is suppressed by approximately 20% compared to the real one.

Gluck Reya Strachmann

Gluck, Reya and Strachmann (GRS) have extended the GRV analysis to include target virtuality effects [14]. They modify the input quark distribution functions $q_i(x, Q_0^2)$ to be

$$\begin{aligned} q_i(x, \tilde{P}^2) &= \eta(P^2) q_i^{\text{NonPert}}(x, \tilde{P}^2) + [1 - \eta(P^2)] q_i^{\text{Pert}}(x, \tilde{P}^2) && (2.48) \\ \tilde{P}^2 &= \max(P^2, Q_0^2) && (2.49) \\ \eta(P^2) &= (1 + P^2/m_\rho^2)^{-2} && (2.50) \end{aligned}$$

where $q_i^{\mathrm{NonPert}}(x, \tilde{P}^2)$ is taken from the π structure function, as in the GRV analysis, and evolved to the scale $\tilde{P}^2$. The distribution function $q_i^{\mathrm{Pert}}(x, \tilde{P}^2)$ is an additional perturbative contribution, which is zero in leading order. The GRV analysis is then applied to these new distribution functions.

Schuler Sjöstrand

The treatment of the P^2 dependence of Schuler and Sjöstrand in [10] (ScSj) is similar to the GRS treatment, where the total quark distribution function is separated into a perturbative and a non-perturbative part. The non-perturbative part is multiplied by the same pre-factor $\eta(P^2)$ and evolved to $\tilde{P}^2$. It is obtained from the fits to photon structure function measurements used in the SaS structure function analysis. The treatment of the perturbative part is somewhat different. A comparison of GRS and SaS for several photon virtualities is shown in Figure 2.3.

Schuler and Sjöstrand have extended the treatment in [10] to include several more models for P^2 suppression [15]. The resulting u quark distribution functions are shown in Figure 2.4. These models show variations of 15% to 30% from the unsuppressed case, and 20% between the two most extreme models.

Drees Godbole

The model proposed by Drees and Godbole [16] (DrGo) allows the modification of existing quark distribution functions for $P^2 \neq 0$. They argue that for

P^2 less than some scale P_0^2 the real photon quark distributions are the correct description, and that as $P^2 \to Q^2$ the QPM result is the correct description. These two results are matched at $P^2 = P_0^2$, yielding

$$q_i(x, Q^2, P^2) = \frac{\ln(Q^2/(P^2 + P_0^2))}{\ln(Q^2/P_0^2)} q_i(x, Q^2) \tag{2.51}$$

$$g(x, Q^2, P^2) = \frac{\ln^2(Q^2/(P^2 + P_0^2))}{\ln^2(Q^2/P_0^2)} g(x, Q^2) \tag{2.52}$$

where P_0^2 is taken to be a typical hadronic scale (m_ρ^2 is used in this thesis). This result is not expected to produce exactly the correct x behavior of the quark distribution functions, but it is argued that it should be a good approximation for calculating cross sections. This model predicts a suppression of approximately 10% for the average values of the kinematic variables studied in thesis.

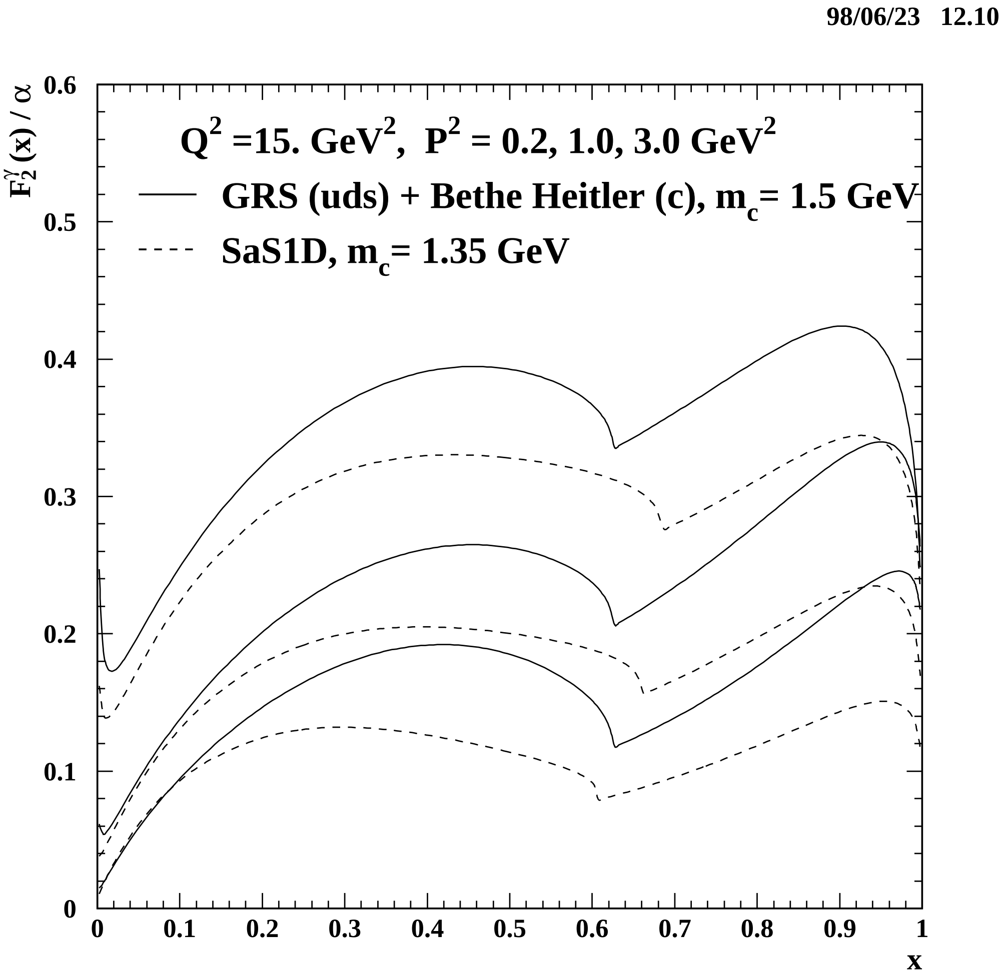

Fig. 2.3: The virtual photon structure function as a function of x_{Bjorken} and P^2.

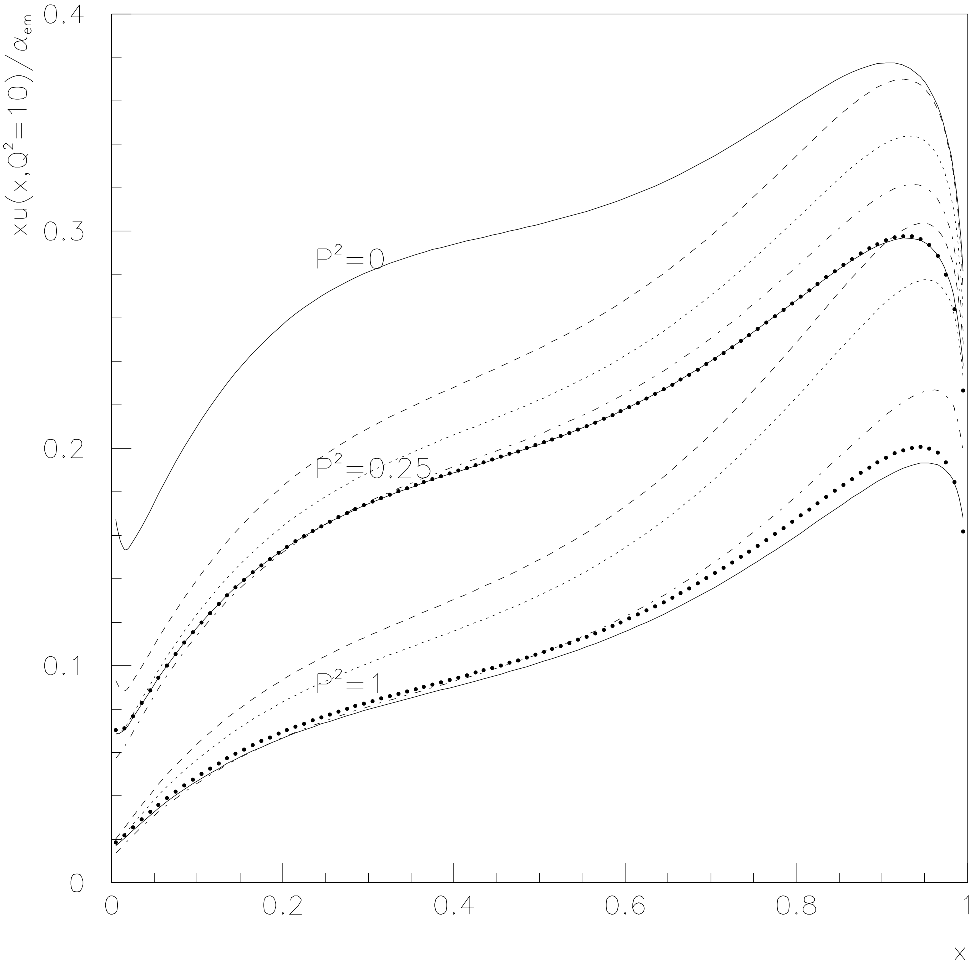

Fig. 2.4: The distribution of u quarks in the photon for the models described in [15], from which this plot was taken.

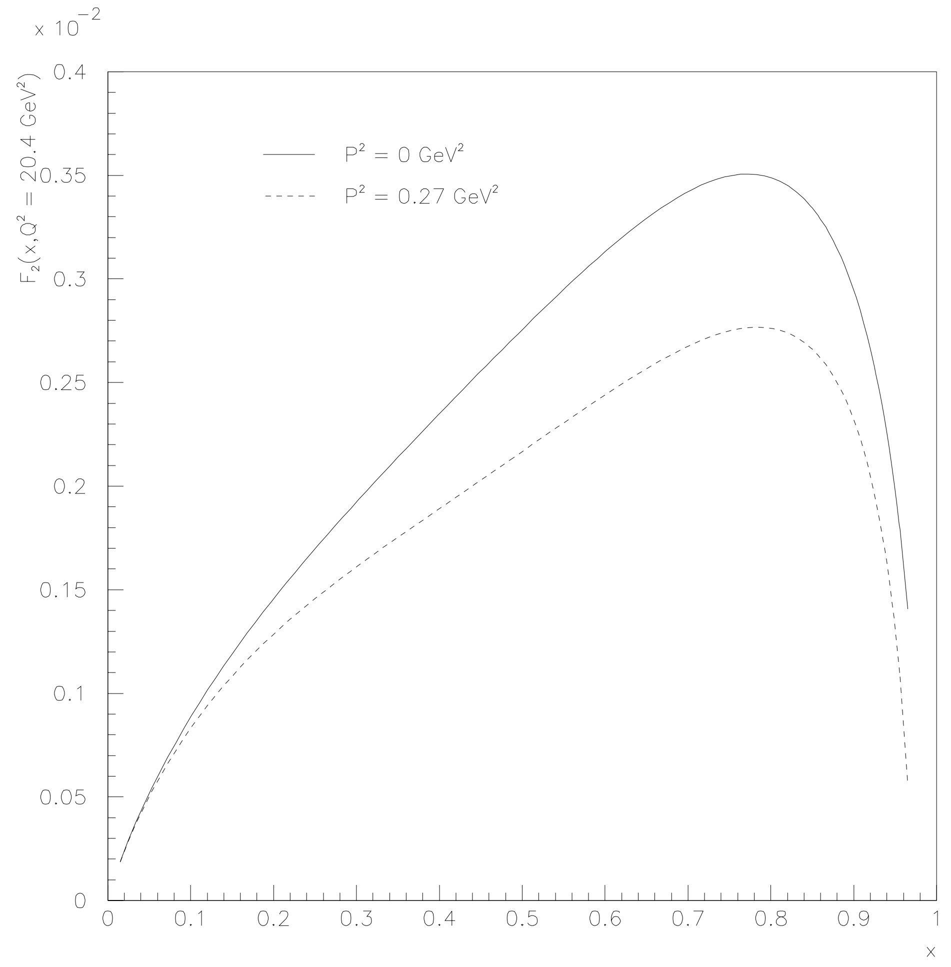

Fig. 2.5: The virtual photon structure function as a function of x_{Bjorken} and P^2, from the QPM calculation of Hill and Ross.

3. THE LEP COLLIDER AND THE OPAL DETECTOR

3.1 The LEP Collider

The Large Electron Positron (LEP) collider at CERN is a storage ring designed to produce Z^0 and $W^{\pm}$ particles via the annihilation of electrons and positrons. During the first phase of LEP (LEP1), Z^0s were produced using beams with center of mass energies $\sqrt{s}$ ranging from 87 GeV to 95 GeV. During the second phase of LEP (LEP2), the $\sqrt{s}$ was raised to 161 GeV, 172 GeV and then to 183 GeV, in order to produce W^+W^- pairs.

In order to save cost and utilize existing laboratory infrastructure, LEP uses the chain of accelerators that already existed at CERN as an injector, which provides 22 GeV electrons and positrons. The CERN accelerator complex is shown in Figure 3.1. It should be noted that the Proton Synchrotron (PS) and Super Proton Synchrotron (SPS) are capable of running in a complex cycle with succesive acceleration of electrons, positrons and protons, so that fixed target experiments using proton beams can operate at the same time as LEP.

LEP has the following elements in each standard cell of the lattice: a defocusing quadrupole, a vertical orbit corrector, a group of six bending dipoles, a sextupole, a focusing quadrupole, a horizontal orbit corrector, a second group

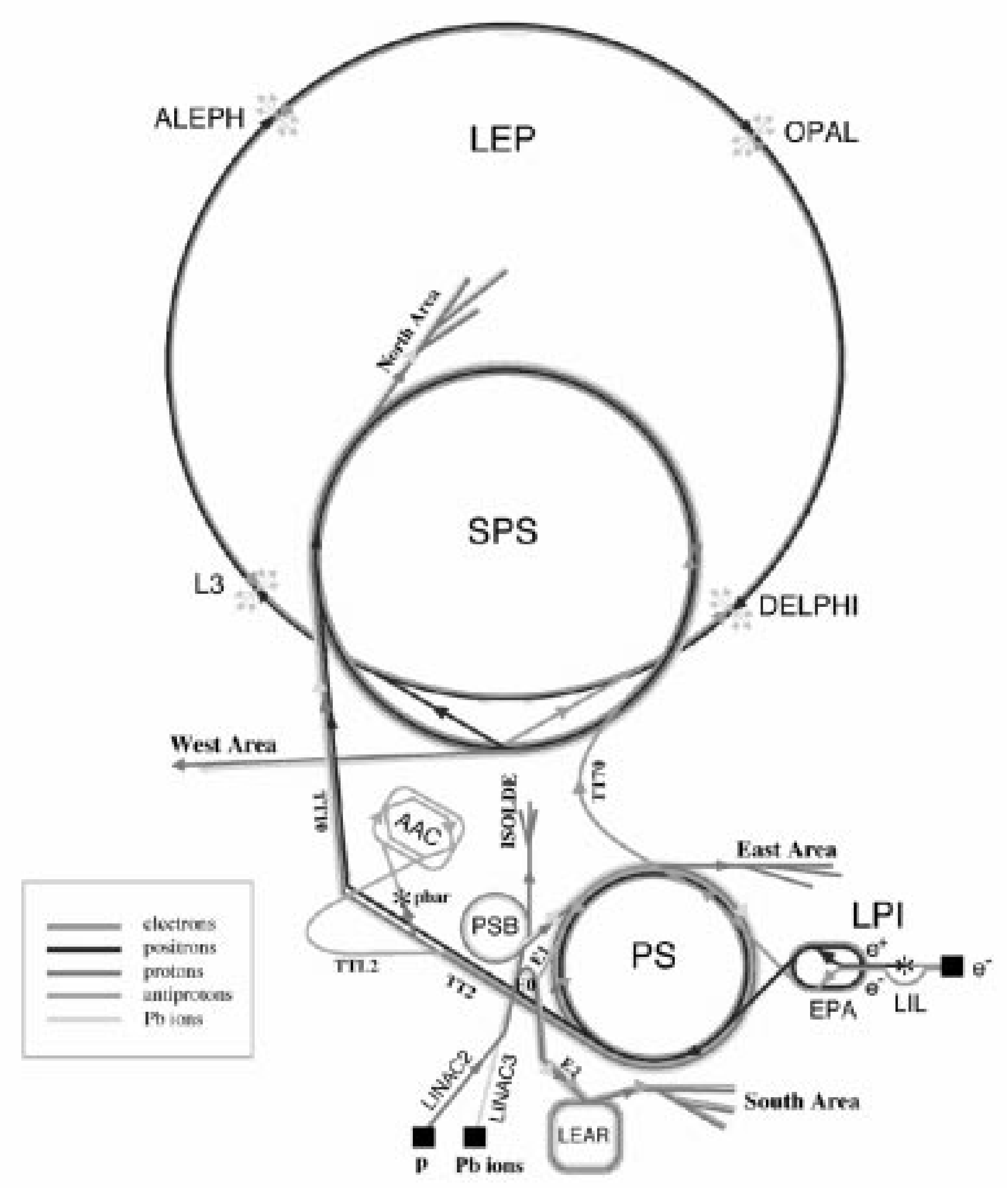

Fig. 3.1: The CERN accelerator complex. (Figure Courtesy of Rudolph Ley, CERN PS Division)

of six bending dipoles and another sextupole. The standard cell is 79.11 m long, and there are 31 standard cells in each of the 8 arcs [17]. In addition to these standard cells which steer the beams around LEP, there are straight sections containing the accelerating cavities and the experiments. The original accelerating cavities were room temperature copper cavities, and superconducting cavities were added for the energy upgrade to LEP2. The existence of the long straight sections turns out to have important consequences for this thesis, as detailed in Section 4.8.

In order to store beams for extended periods of time, it is necessary for them to travel in an extremely high vacuum. This is accomplished at LEP using a 26.67 km long vacuum chamber and two pumping technologies. The vacuum in LEP has been measured to be 10^{-12} Torr when no beams are in the machine, and typically declines to 10^{-9} Torr when beams are present, because synchrotron radiation causes outgassing in the vacuum chamber. This outgassing is more pronounced in the arcs, where the synchrotron photons impact the walls of the vacuum chamber. Pumping is provided in two stages; a 'rough' pumping system achieves vacuums of 10^{-4} Torr, and a non-evaporable getter strip provides the ultra-high vacuum. This strip is composed of several compounds which react with the active gases to form stable compounds. The residual gas in the vacuum chamber thus 'sticks' to the getter strip.

3.2 The OPAL Coordinate System

In order to discuss the OPAL experiment, it is helpful to define the OPAL coordinate system, as well as some terms used to denote positions in OPAL. A cutaway view of OPAL is shown in Figure 3.2, and the OPAL coordinate system is illustrated there. The LEP vacuum chamber passes through the center of OPAL, and defines the z-axis. The plane defined by the LEP ring is at an angle of 13.9 mrad with respect to the horizontal plane. The OPAL x-axis is in the plane of the ring and points towards the center of LEP, the positive z-axis is in the e^- beam direction, and the y-axis therefore points up, perpendicular to the LEP ring plane, to form a right handed coordinate system. Spherical polar coordinates will often be used, and these have their normal definition relative to the OPAL coordinate system.

Several terms will be used to indicate the position of various detector components in OPAL. The terms Left and Right are defined as those directions when standing next to the LEP access point 6 PZ access shaft (which is on the outside of the LEP ring) and facing the detector. From the same location, Near denotes the side of the detector closest to the observer, and Far the side of the detector away from the observer. Thus, Right Far refers to an object in the positive x, positive z quadrant of the xz plane.

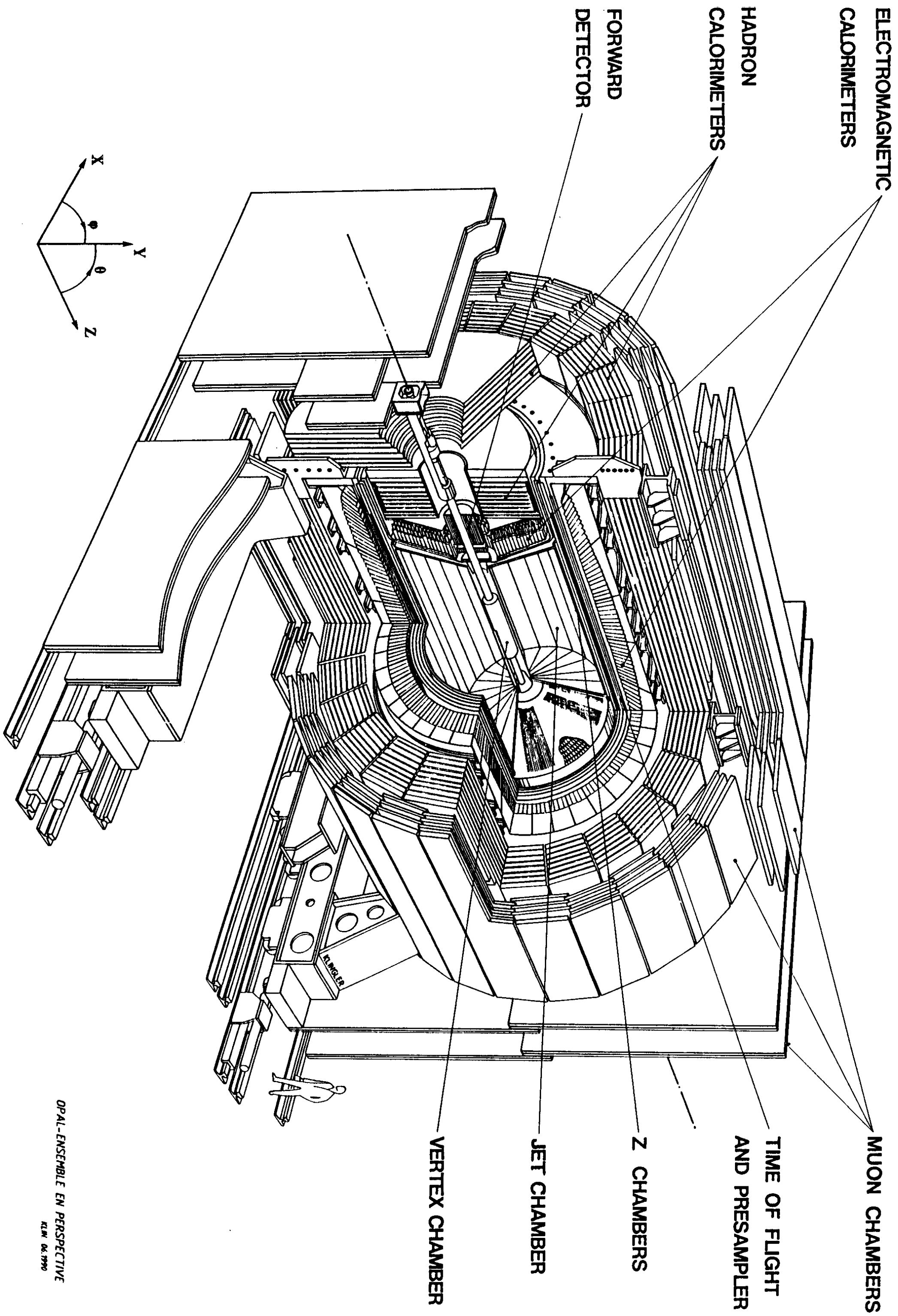

Fig. 3.2: Cutaway view of the OPAL detector at LEP.

3.3 The OPAL Detector

The acronym OPAL is formed from the phrase Omni-Purpose Apparatus for LEP. The OPAL detector is designed to provide good measurement of particle momenta, particle energy and in some cases particle species. This is accomplished using many subdetector systems and combining the information from them.

A cross-section of OPAL is shown in Figure 3.3. OPAL is constructed as a long cylinder. The central part of the cylinder is called the barrel. The solid angle covered by the detector is extended by two endcaps, at either end of the barrel. The barrel region contains tracking systems for charged particles, a time of flight counter system, an electromagnetic calorimeter, a hadron calorimeter and a further set of tracking chambers to detect muons which exit the detector. The endcaps do not contain a separate tracking system, but otherwise have a similar set of subdetectors. A set of small subdetectors directly around the beam pipe are used to measure luminosity, using Bhabha scattering events. Each of the OPAL subdetector systems is described below, with more emphasis placed on those which are used in the analysis presented in this thesis. A complete description of OPAL can be found in Nuclear Instruments and Methods [18].

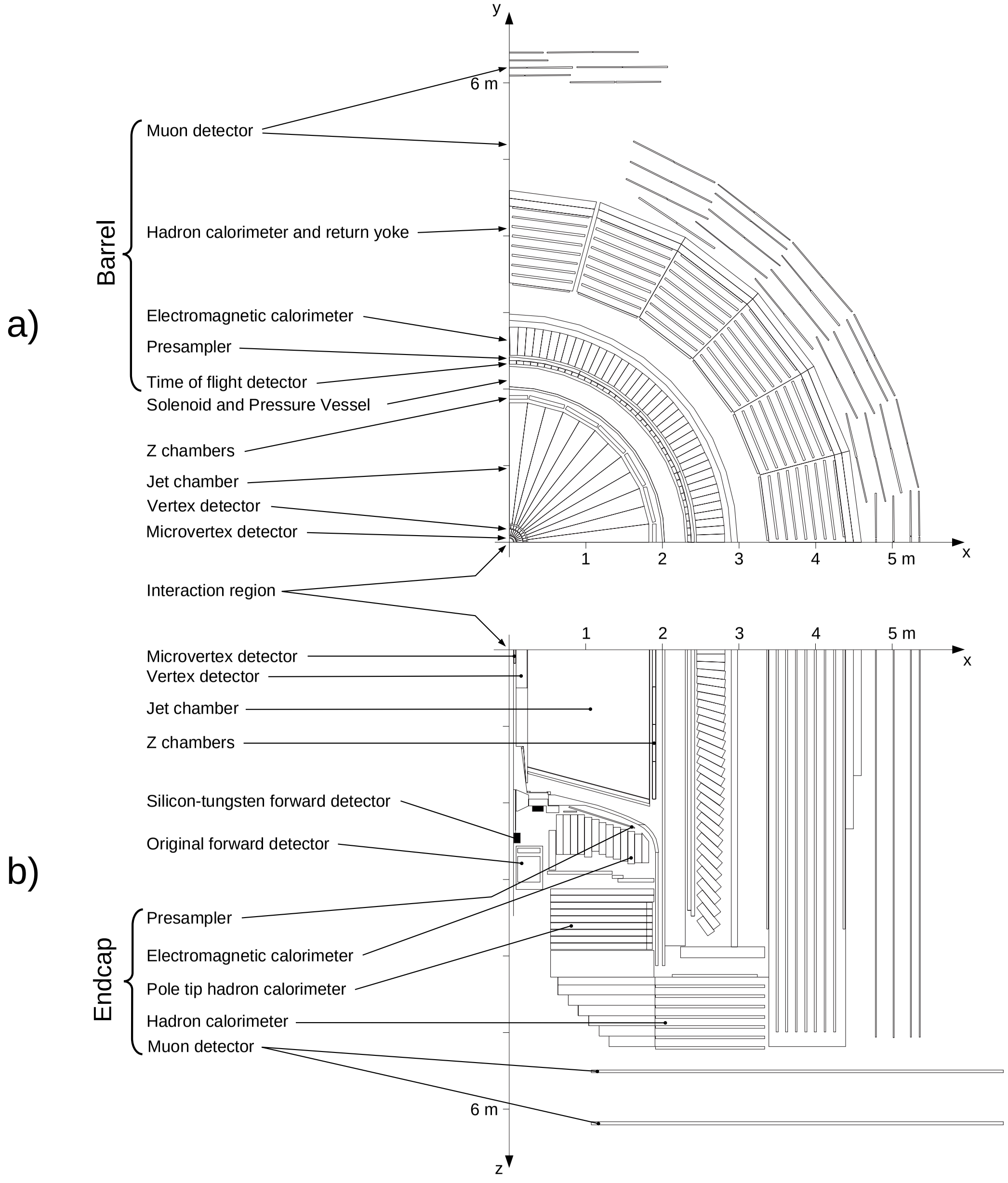

Fig. 3.3: Cross section view of the OPAL detector.

3.3.1 The Central Tracking System

Four subdetectors form the central tracking system. These are the Silicon Microvertex Detector (SI), the Central Vertex chambers (CV), the Central Jet chamber (CJ) and Central Z chambers (CZ). All four detectors provide measurements of points along the path of a charged particle traversing the OPAL barrel, and each is optimized to give information about a particular part of the path, so that the central tracking system provides a good measurement of charged particle momentum, position of origin and particle species. The individual subdetectors and their specific contributions to tracking are described below.

Closest to the interaction point (IP) is the Silicon Microvertex detector. The first version was installed in 1991. This subdetector is made of two layers of semi-conducting silicon wafers which are divided into strips. Each layer has two back-to-back single sided detectors, one giving coordinates in the r-ϕ plane and the other along the z axis. The strips have a voltage bias across them, and when a charged particle passes through them, charge from ionization in the silicon is collected on the readout strips. Using the charge on each strip, and combining information from the layers, the path of a charged particle through the silicon can be reconstructed. The inner layer is at a radius of approximately 61 mm and the outer layer is at a radius of approximately 75 mm. The microvertex detector is especially important for reconstructing tracks from particles decaying away from the primary interaction point. The silicon operates at ambient atmospheric pressure, in the gap between the beam pipe and the inner wall of the OPAL pressure vessel.

The Central Vertex chambers surround the microvertex detector and are inside the OPAL pressure vessel, which provides a common 4 bar gas pressure used by the CV, CJ and CZ central tracking detectors. This gas is a mixture of 88.2% argon, 9.8% methane and 2.0% isobutane. The CV detector was an original component of OPAL, and serves a purpose similar to that of the Silicon Microvertex detector, by providing precisely measured points on the particle path near the interaction point. These points allow the determination of the origin of the path and improve the overall momentum resolution of the central tracking system. CV is 1 m long and 470 mm in diameter. It is a cylindrical drift chamber with two layers of 36 cells each. The readout wires in the inner layer are axial, and those in the outer layer are stereo with a 4 degree tilt. The inner cells provide a measurement of points in the r-ϕ plane with a resolution of 50 μm. The combination of the axial and stereo wires provides a z position measurement. The design of CV is based on that of the Central Jet chamber.

The Central Jet chamber is a large volume gaseous detector. It surrounds the CV starting at a radius of 0.5 m and extending to a radius of 3.7 m, and is approximately 4 m long. The chamber has 24 sectors, each of which contains a plane of 159 anode sense wires parallel to the z axis. Cathode wire planes separate adjacent sectors. Particle paths with polar angles from 43 degrees to 137 degrees pass all 159 wires in a plane before exiting the CJ, while particle paths with lower or higher polar angles exit the ends of the jet chamber and pass fewer sense wires. The CJ allows the measurement of charged particle momenta by recording the bending of particle paths caused by the 0.435 Tesla solenoidal magnetic field in the central part of OPAL. In addition, particle species identification is provided by measuring the rate of energy loss of particles traversing the chamber.

The Central Z chambers surround the CJ. These chambers cover the polar angle range from 44 degrees to 136 degrees. They make a precise measurement of the z coordinate of particle paths exiting the CJ and thus improve the polar angle measurement. CV is made up of 24 chambers. Each chamber is 4 m long, 500 mm wide and 59 mm thick. The chambers are divided into 8 cells in z, each 500 mm long, and each cell contains six readout wires.

The impact parameter resolution of the combined CV, CJ and CZ system was measured in 1989 using $e^+e^- \rightarrow \mu^+\mu^-$ events. The resolution was 75 μm in the r-ϕ plane. In the r-z plane, the resolution was 2 mm, using the CV stereo wires, and 2.7 cm without them.

For this analysis, the Central Tracking System is important for triggering on and reconstructing the hadronic final state.

3.3.2 Time Of Flight System and Tile Endcap System

The time of flight system is behind the pressure vessel and solenoid, and measures the transit time of particles from the interaction point. The subdetector is made up of 160 scintillation counters, which are trapezoidal in shape, with a length of 6.84 m, a depth of 45 mm and a width ranging from 89 to 91 mm. They form a layer around the outside of the solenoid and pressure vessel at 2.36 m radius. The system covers the solid angle range $|\cos\theta| < 0.82$. Each counter is read out at both ends, and a z position measurement of particles traversing the counters is made using the difference in arrival times for signals at each end of the counter.

The TOF system (TB) provides trigger signals and a particle identification system for charged particles in the energy range 0.6 to 2.5 GeV. The time resolution has been measured using $e^+e^- \to \mu^+\mu^-$ events, and was 460 ps, without the use of external z position information. The TOF trigger information is important for the physics studied in this thesis.

In addition to the TOF system, which covers the barrel region, a scintillating tile system was installed in the OPAL endcap region in 1996. This system provides timing information and the capability to detect minimum ionizing particles in the endcap region. It is based on scintillating tiles with wavelength shifting fiber technology, and is called the Tile Endcap system (TE).

3.3.3 Electromagnetic Presampler and Calorimeter

Behind the TB/TE system is the Electromagnetic Presampler system. In the barrel, this system is a set of gaseous limited streamer mode chambers which samples the energy of particles that have showered in the material between the interaction point and the Electromagnetic Calorimeter, especially in the magnetic coil. In the endcap region, the Electromagnetic Presampler is a ring of thin gaseous multiwire chambers which are operated in high gain mode. Combining the presampler information with the Electromagnetic Calorimeter information provides an improved energy resolution for electromagnetic showers, because the number of charged particles passing through the presampler is approximately proportional to the energy deposited in the material traversed before the presampler.

The Electromagnetic Calorimeter is made of an array of lead-glass blocks. In the barrel region, these blocks have a pointing geometry and point close to the nominal interaction point. In the endcap region the long axes of the blocks are parallel to the z axis. The Barrel Electromagnetic calorimeter starts at a radius of 2.455 m and contains 9,440 lead glass blocks. Each block is 37 cm (24.6 radiation lengths) deep and approximately 10 × 10 cm^2. The Endcap Electromagnetic calorimeters are composed of 2,264 lead-glass blocks of varying lengths; 380, 420, and 520 mm. The differing lengths of the blocks allow the endcap calorimeter follow the contour of the pressure bell of the central tracking system. They present a minimum of 20.5 radiation lengths to particles traversing them. The Barrel Electromagnetic calorimeter covers $|\cos\theta| < 0.82$, while the Endcap Electromagnetic calorimeter covers $0.83 < |\cos\theta| < 0.95$. The total electromagnetic calorimetric coverage of OPAL is extended further by the forward detectors described below. The energy resolution of a prototype barrel section was measured, in a testbeam, to be $\sigma_E/E = 0.2\% + 6.3\%/\sqrt{E}$ with no material in front of the calorimeter.

3.3.4 The Hadronic Calorimeter

An iron magnetic flux return yolk is situated behind the Electromagnetic Calorimeter and provides the passive material for the Hadron Calorimeter. The Hadron Calorimeter is a sampling calorimeter made of alternating layers of limited streamer chambers and layers of iron. The iron layers are 100 mm thick and provide approximately four interaction lengths of material, in addition to the 2.2 interaction lengths in front of the Hadron Calorimeter. Hadronic energy measurements are made by combining information from the Electromagnetic Calorimeter and the Hadronic Calorimeter.

3.3.5 Muon Chambers

The outer layer of the barrel is made up of the muon chambers. The Barrel Muon chambers are large area drift chambers, and the Barrel Muon system has four layers of chambers. These chambers detect charged particles which have traversed the whole of the OPAL barrel. These particles are primarily muons, with a small contamination of hadrons. The outermost layer of the endcaps is the Endcap Muon system. This system is made of gaseous limited streamer tube chambers. The muon chambers are not used in this analysis.

3.3.6 The Forward Tagging Detectors

The electromagnetic calorimetry of OPAL is extended to very low angles relative to the beam direction by the forward tagging detectors. These detectors provide precision luminosity measurement using Bhabha scattering events. In order to minimize the error on the luminosity measurement, two conditions must be met. The detectors must be at low angles so that the rate of Bhabha events is high, in order to minimize the statistical error on the luminosity measurement. In addition, the acceptance of the detector must be well known, in order to minimize the systematic error in calculating the luminosity from the measured counting rate. All of the forward detectors are also used to tag electrons from $\gamma\gamma$ interactions.

The Forward Detectors (FD) are the original luminosity measurement detectors in OPAL. There are two Forward Detectors, one at each end of OPAL, which are symmetric about the interaction point. A Forward Detector is actually composed of a number of subsystems, which meet various performance requirements in the forward region. The Gamma Catcher is a lead scintillator ring 7 radiation lengths thick, which fills the gap in coverage from 200 to 154 mrad between the Electromagnetic Endcaps and the Forward Calorimeter. The Forward Calorimeter is the main part of the Forward Detector. It is a lead scintillator sampling calorimeter 24 radiation lengths deep. The first four radiation lengths are a presampler, and only read out on the outer edge. The back 20 radiation lengths are read out on both the inner and outer edges. The Tube Chambers are located between the presampler and the main part of the Forward Calorimeter (Figure 3.4 incorrectly shows them at the center of the FD). The Tube Chambers are three layers of proportional tubes, with two layers aligned at right angles, and the third layer at 45 degrees to the other two. The Tube Chambers allow a determination

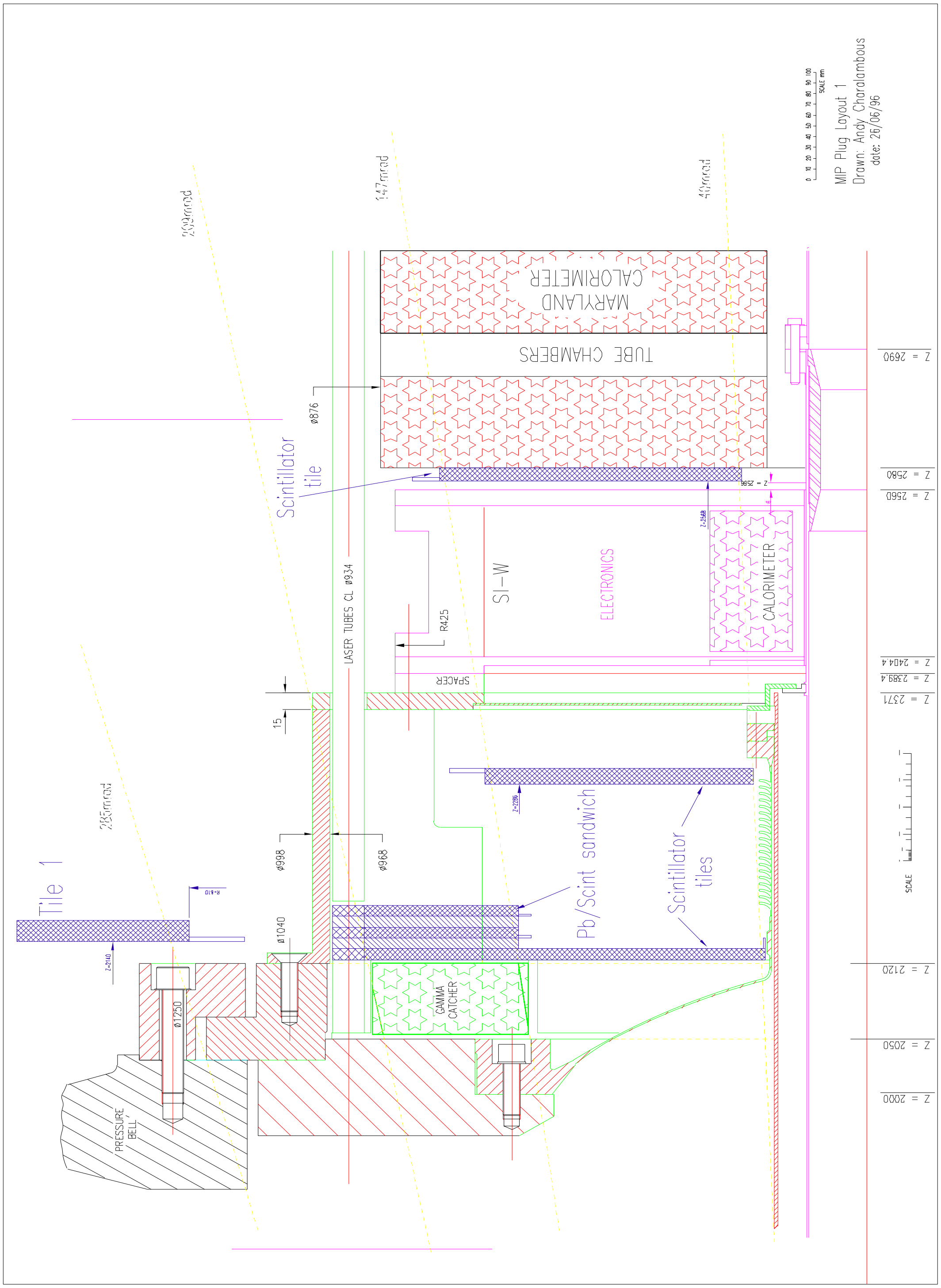

Fig. 3.4: The Forward Region in OPAL.

of shower positions within the Forward Calorimeter with an accuracy of ±3 mm.

Before 1993, the Forward Detectors also had two other subsystems for determining luminosity. These were the Drift Chambers and the Fine Luminosity Monitors. There were 4 pairs of Drift Chambers at each end of OPAL, mounted on the front of the Forward Calorimeter. These drift chambers provided more precise determination of incident particle angles and were also used to precisely survey the positions of the Tube Chambers. The Fine Luminosity monitors were four pairs of scintillation counters, precisely positioned, which defined a well known acceptance for the Forward Calorimeter. The cross section for Bhabha events into the Fine Luminosity monitors was $\approx$ 7 nb at the Z^0 resonance.

Because of the need for a higher statistics luminosity measurement, the Forward Detectors were supplemented in 1993 by the Silicon Tungsten Luminometers. In order to make space in the forward region, the Fine Luminosity monitors were removed. The Silicon Tungsten Luminometers overlap the Forward Detectors, and extend electromagnetic calorimetric coverage to 27 mrad. They are sampling calorimeters with passive layers of tungsten, and active layers of silicon segmented into pads that are read out individually.

The Far Forward Monitors are a subsystem of the Forward Detectors. They were originally intended to provide a fast luminosity measurement. These detectors are one of the main tools used in this thesis, and are described in great detail in Chapter 4.

3.3.7 Run Control and Data Acquisition System

The data acquisition system in OPAL is based on distributed processing by each subdetector, under central control. The individual subdetector systems are based on NIM, CAMAC and VME modules which drive the front-end electronics mounted on the detector. A bunch crossing signal is provided to all the subdetectors for synchronization. Immediately after each bunch crossing, those subdetectors whose data is used to make a trigger decision send information to the central trigger unit. This information could be, for example, a logic signal indicating that the sum of energy in a region of the detector is above some threshold. If a positive trigger decision is not forthcoming, each subdetector resets and acquires data again on the next bunch crossing. A schematic of the OPAL DAQ is shown in Figure 3.5.

If a positive trigger decision is forthcoming, data is digitized and stored in a data object suitable for transfer to the Event Builder, which assembles the data from different subdetectors for the same bunch crossing into an event, which is the logical unit processed by the OPAL reconstruction software.

Global control of the individual subdetectors is provided by a system known as Run Control. Run Control is based on a state machine concept, in which each part of the data acquisition system is in a well defined state. A set of rules then governs transitions from one state to another. These transitions are initiated either automatically or by human intervention.

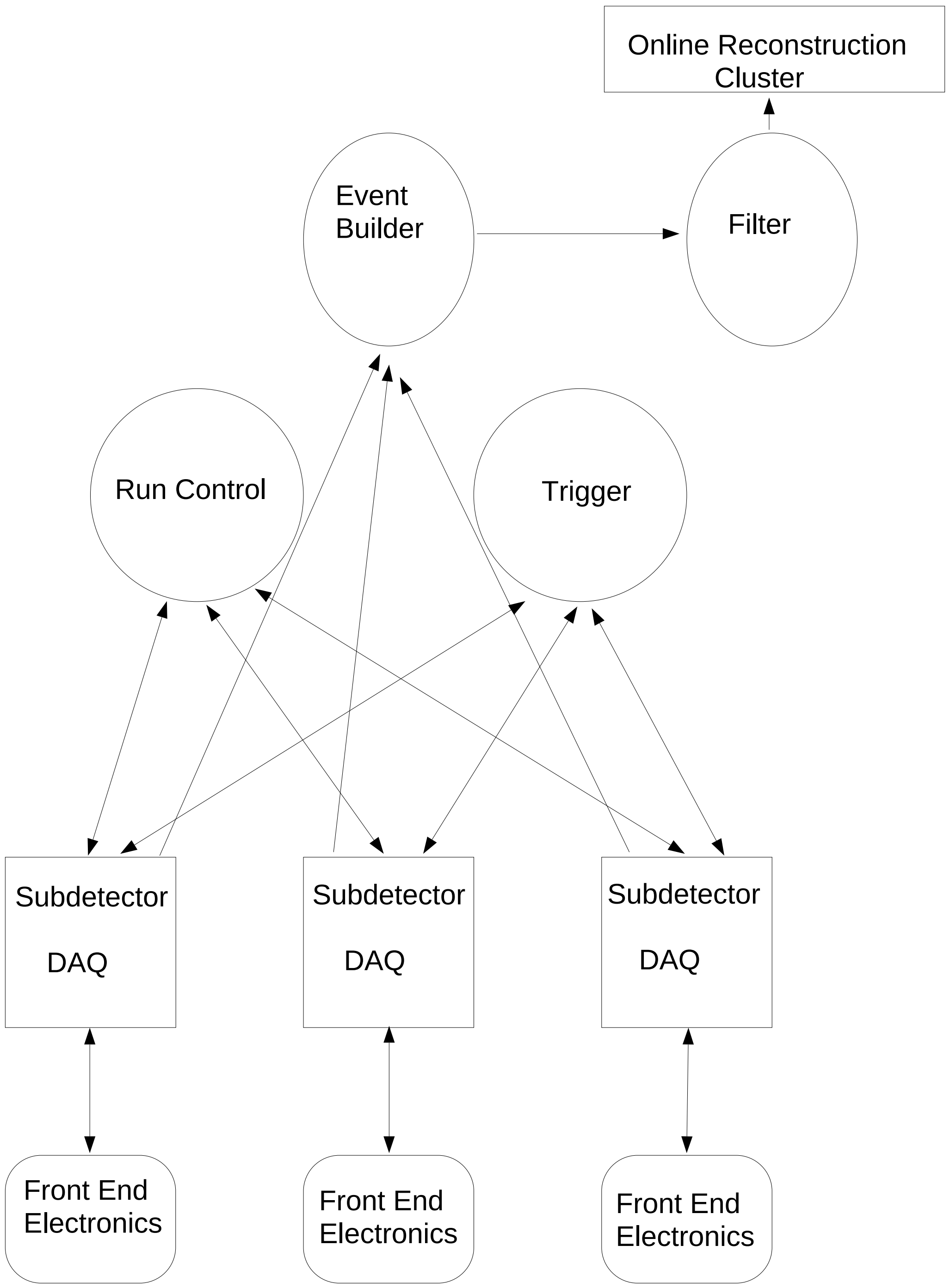

Fig. 3.5: A schematic of the OPAL DAQ system. Information flows along the lines in the direction of the arrows.

3.3.8 Trigger

The OPAL trigger system is designed to reduce the 45 kHz LEP bunch crossing frequency to an event rate of less than 10 to 15 Hz, by making fast decisions about whether a bunch crossing contains an interesting physics event. This is achieved by combining information provided by the various subdetectors and selecting events based on a set of criteria programmed into the system. The trigger signals from the various subdetectors are used in two ways, either as standalone logic signals, or as input to a system which provides logic signals based on correlations between different subdetectors in the same theta and phi region ($\theta - \phi$ matrix).

The standalone trigger signals are generally based on an energy sum above some threshold in the calorimeters or the track multiplicity in the central tracking system. Track multiplicity is determined by the track trigger, which is capable of finding tracks with momenta above about 250 MeV/c. The track trigger finds tracks separately in different regions of theta and phi, so that the total number of tracks can be used for stand-alone triggers, while the individual $\theta - \phi$ bins can be used as input to the $\theta - \phi$ matrix. The inputs to the $\theta - \phi$ matrix are logic signals indicating that a particular subdetector had activity in a certain region of theta and phi. A $\theta - \phi$ coincidence is generated when mutliple subdetectors have activity in the same $\theta - \phi$ bin, and this coincidence is passed to the central trigger logic.

The standalone trigger signals and the $\theta - \phi$ coincidence signals are combined in a flexible way in the central trigger logic, which is based on programmable logic. If a positive trigger decision is made, a trigger interupt is sent to the subdetectors via a custom trigger bus, and they are read out by the DAQ. If a negative trigger decision is made, a reset is sent on the bus, and the subdetectors acquire data again on the next bunch crossing. The reset or trigger interupt signal is sent approximately 15 μs after the bunch crossing, allowing 7 μs for subdetectors to reset [19].

A second level of data rejection is provided by the filter, which partially reconstructs triggered events, and places more complex requirements on them. The filter is implemented using a cluster of HP 742 and 747 machines which reside in VME crates. Events which pass the filter selection are transfered to the online computing cluster for complete reconstruction, and also written to tape.

3.3.9 Online Computing

In addition to the online computing performed by the subdetectors, the trigger, the event builder and the filter, there is a farm of HP workstations which processes events passing the filter selection. The farm performs three tasks. One is to completely process each event, using the full OPAL reconstruction software. Another is to archive data for future use. The primary archive medium is writeable optical disk, which is attached directly to the farm, while the secondary medium is tape located at the main CERN site. The final task is to use the processed events to provide information used to monitor and calibrate the detector. Because the reconstruction processing occurs nearly in real time, this monitoring information can prove useful for quickly locating faults. Once these task have been performed, the data is transfered to one of the offline computing facilities for analysis. Information about the number of events recorded and total data volume for each year of data taking can be found in Appendix A.

4. CALIBRATION OF THE FAR FORWARD MONITORS

The Far Forward Monitors (FFMs) provide OPAL with the capability of observing electrons which have been scattered through very small angles. The FFMs were installed for the entirety of OPAL data taking, but have not previously been used in a physics analysis. In the course of studying data from the FFMs a number of problems were observed and corrected, as described in Section 4.1. In addition, the capabilities of the detectors have been understood and an upgrade has been performed to increase the FFMs' performance.

4.1 Description of the Far Forward Monitors

The OPAL Far Forward Monitors are four small lead plastic-scintillator sampling calorimeters. The FFM modules are mounted 7.7 m from the interaction point, on both sides of the beam pipe at both ends of OPAL, behind the LEP mini-β quadrupoles which are defocusing in the horizontal plane. Defocusing by the quadrupole lowers the scattering angle for which particles are accepted and also introduces an energy dependence in the angular acceptance.

The dimensions of the sensitive part of the modules are 50 mm along the x axis, 140 mm along the y axis and 203 mm along the z axis. Each module is divided into six compartments, so that the position of a shower within the module can be measured using energy sharing. The scintillator slabs in each compartment are read out as a group by a wavelength shifting bar. The positions of the compartments are shown in Figure 4.1. For the exposition that follows, each compartment is labeled by it's position; the first part of the compartment label denotes either the upper or lower part of the detector, and the second denotes either the outer, inner, or front part of the detector. Each of the four modules will be referred to by its location as described previously in Section 3.2; Right Far (RF), Right Near (RN), Left Far (LF), or Left Near (LN). For example, the upper front compartment of the Left Far module is refered to as LF uf. The front compartments have four layers of scintillator, while the back compartments have ten layers of scintillator. The 5 mm thick scintillator slabs alternate with 6.2 mm (1.1 X_0) layers of lead. There are 12.6 mm of lead in front of the first layer of scintillator and 25.3 mm of lead after the last layer of scintillator. The 4.4 X_0 of lead at the back of the detector provides protection from synchrotron radiation entering the detector from behind. The lead layers are bolted to an aluminum plate on the edge away from the beam pipe, which provides support for the entire detector module. The inner edge of the detector is covered by a 1.4 mm thick lead sheet, which provides shielding against low energy synchrotron radiation.

The scintillator slabs in each compartment are read out by a Y7 wave-

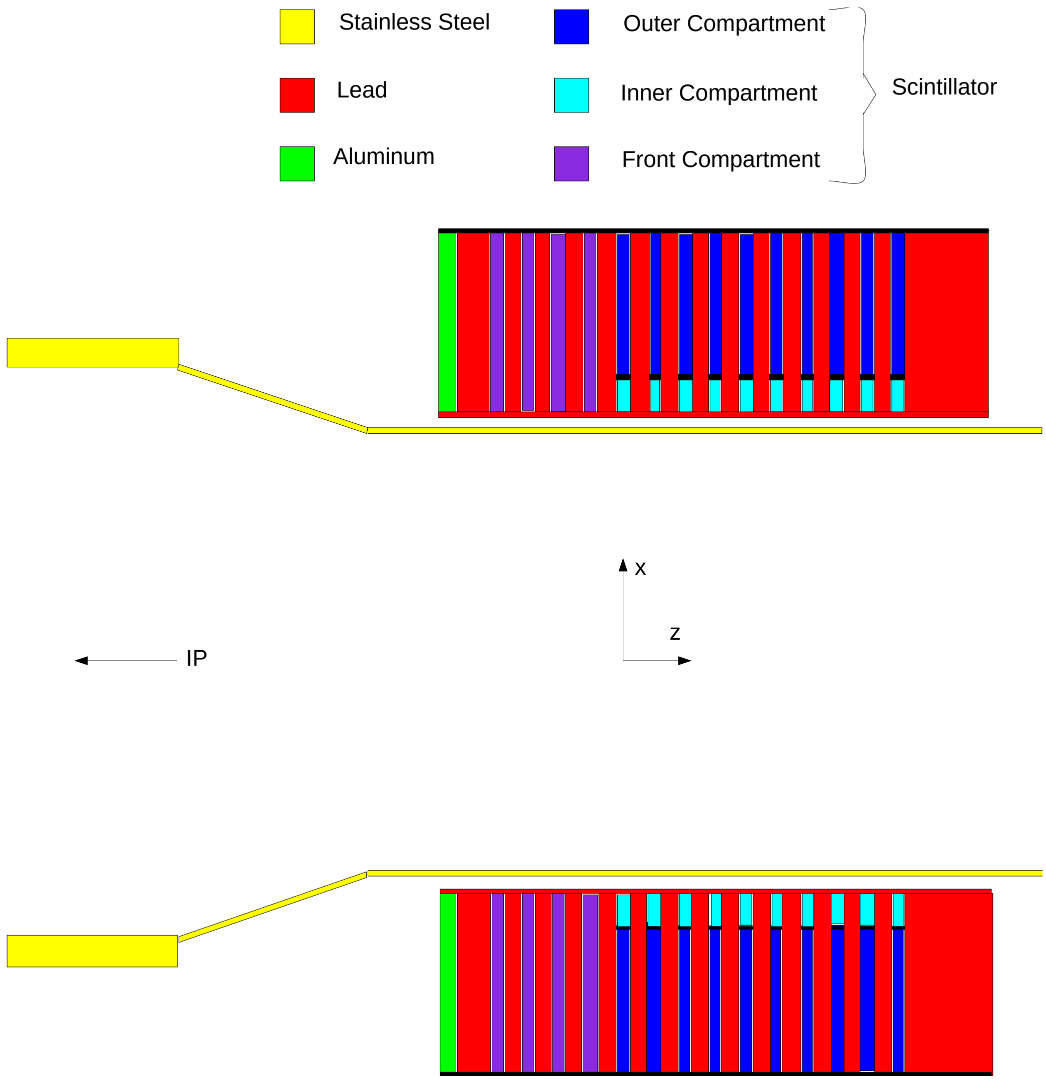

Fig. 4.1: Schematic top view of the beam pipe and one pair of FFM's. Three separate sets of scintillator slabs are shown in the schematic, each with its own color. These sets comprise the Outer, Inner and Front compartments of each FFM.

length shifting bar, which is attached to a perspex light guide, directing the light on to a Hammamatsu R1213 phototube. A partially disassembled FFM is shown in the photographs in Figure 4.2 and Figure 4.3. The bases of the phototubes are custom built and reside on circuit boards near the PMTs. The bases drive coaxial cables which run for approximately 50 m to trigger and readout electronics. The trigger is described below and the readout consists of 24 channels of Lecroy 2249A ADC's [20].

During the initial analysis of FFM data from LEP 1, it was discovered that the light yield from the compartments, especially the inner ones, had been degrading with time. In addition, a large amount of crosstalk between the adjacent inner and outer compartments in each module was observed. Because of these problems, and in order to install an LED test system, the FFM's were dismantled and refurbished during the 1996-1997 shutdown.

After opening the modules, the cause of the degradation in light yield became clear. All of the wavelength shifting bars had crazed. For the front and outer compartments, the wavelength shifting bars had been flat slabs of Poly-Vinyl Toluene (PVT) doped with BBQ wavelength shifting dye and attached to Perspex light guides. For the inner compartments, the PVT had been bent, so that no separate light guide was needed. The bent part of the inner compartment PVT slabs were exceptionally crazed. For all compartments, the optical connection to the PMT had been made using a Perspex cylinder, to which the light guide had been glued, and which contacted the face of the PMT through a layer of optical grease. For some compartments,

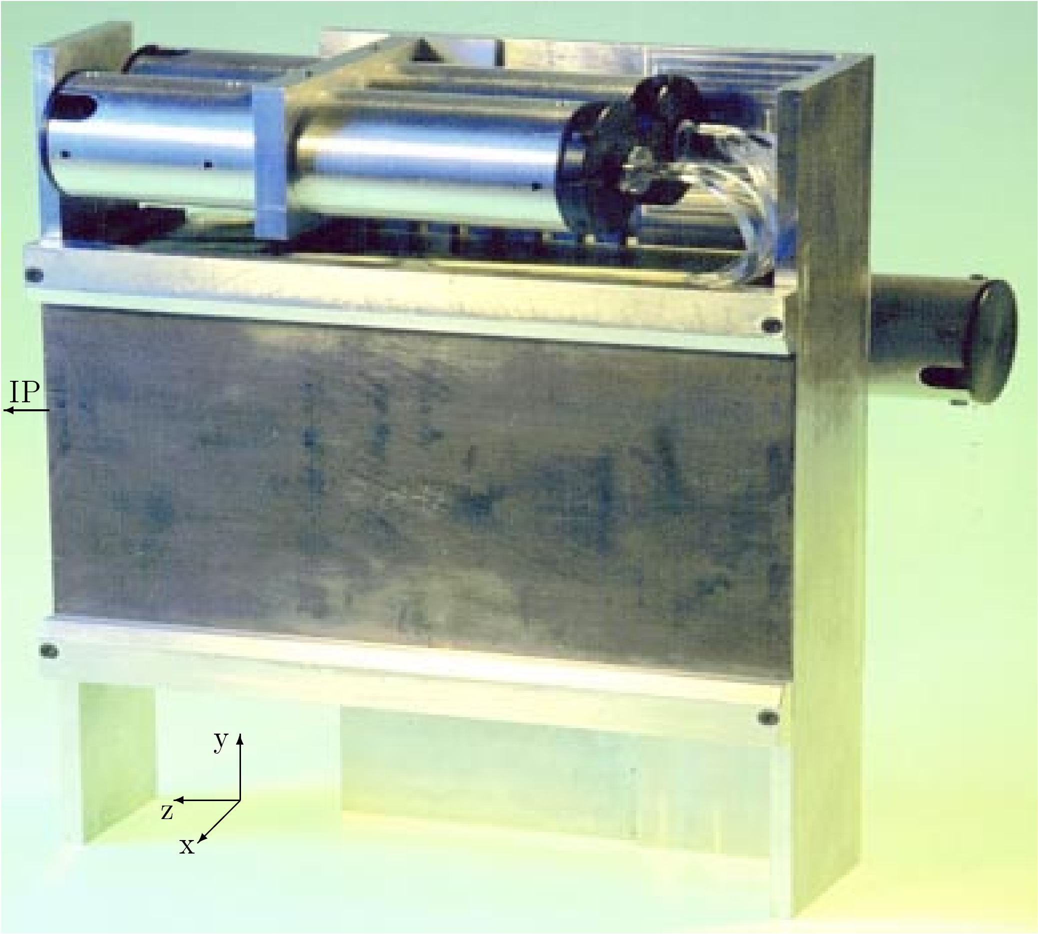

Fig. 4.2: A partially disassembled FFM module, looking at the side mounted next to the beam pipe. The thin lead plate which covers the active part of the detector is visible in the center of the photograph. The light guides for the upper inner and outer compartments are visible at the top of the photo, and the light guides for the lower compartments would be mounted in the same relative positions.

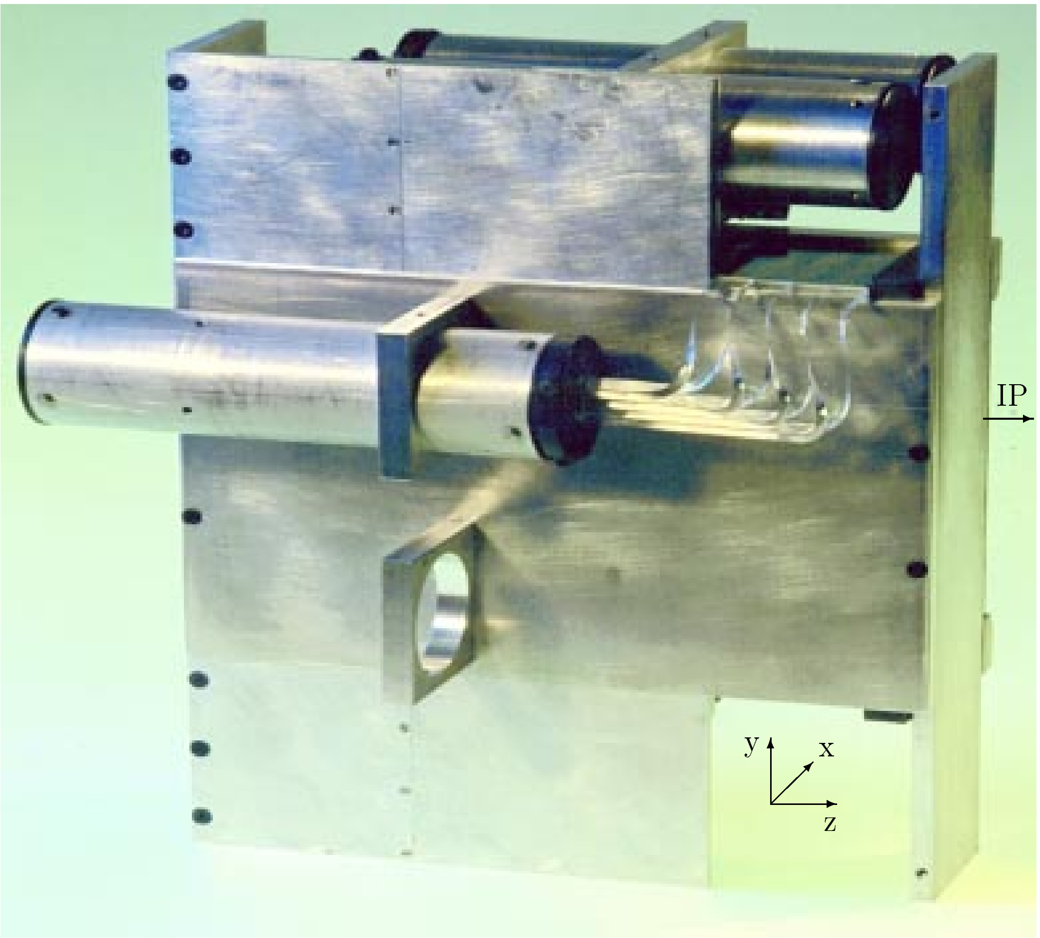

Fig. 4.3: The partially disassembled FFM module, looking towards the side which is mounted away from the beam pipe. The light guide for the upper front compartment is visible at the right of the photo, and the lower front PMT would be mounted in the same relative position. The PMT base printed circuit boards would be mounted on the aluminum plates above and below the front compartment phototubes.

the glue joint between the light guide and the Perspex cylinder had broken, resulting in further light loss.

In order to remedy the problems with the wavelength shifter bars and light guides, new wavelength shifter/light guide combinations were fabricated by the CERN scintillator workshop. Polystyrene doped with Y7 wavelength shifter leftover from the construction of the OPAL Forward Calorimeter was used. New Perspex light guides were made for all compartments, including the inner ones.

Two problems contributing to the crosstalk between inner and outer compartments were found. These were the way in which the resistor network providing high voltage to the PMT's had been designed, and a wiring error in the resistor network at the anode end.

In contravention of common practice, the resistor network for each PMT had not been constructed directly on the socket into which the pins of the PMT are inserted. Instead, the resistor networks for each set of Outer, Inner and Front compartment PMT's had been constructed together on a circuit board which was mounted in a separate part of the module, as described in the caption of Figure 4.3. The high voltage from the resistor network had been connected to the socket for each PMT via single strand insulated wires with a length of approximately 20 cm each. In routing the wires from the resistor networks to the sockets, two bundles of wires had been made. One bundle contained the wires for the front compartment PMT, while the other bundle contained the wires for both the Inner and Outer compartment

PMT's. A separate problem with the design of the resistor networks had been the use of a common ground for the resistor networks of the three PMT's housed on the same circuit board, which was also used as the ground for one side of the coaxial cable used to carry the output signal. Both of these design features contributed to cross talk between different compartments.

While a solution to the problems of the resistor network was being sought at UCL, an additional problem was discovered. A mistake had been made with the wiring of the anode end of the resistor network. In an attempt to fix the problems associated with the resistor network, the following changes were made by UCL technicians during the 1996-1997 FFM refurbishment:

- The single strand wires for each PMT were bundled separately and wrapped in a ground braid.
- Small value resistors were introduced into the last two dynode lines and the ground connector, close to the PMT socket.
- The coaxial signal output lines were isolated from each other and the high voltage.
- The resistors at the anode end of the resistor network were reorganized.

In addition to the changes made in order to fix observed problems, extra modifications were made to allow for better testing of the modules. An LED test system was installed, with a green LED glued to each of the wavelength shifting bars and attached to a plug mounted on the FFM case. These LEDs are driven remotely via a pulse generater, and allow for testing of the modules before and after installation.

4.2 Online Luminosity Measurement

The FFM calibration is based on Bhabha events, which are also used to provide the OPAL online luminosity measurement. In addition, the online luminosity measurement provides a good way of monitoring the FFM data quality. For these reasons, a general outline of the online luminosity measurement is a good starting point for understanding the FFM calibration.

The online luminosity is a near real time estimate of the luminosity being delivered to OPAL. This information, along with similar information provided by the other LEP experiments, is used to optimize the luminosity delivered to the LEP experiments.

The FFM luminosity,L_{FFM}, and Bhabha cross section, σ_{FFM}, are defined as

$$L_{\mathrm{FFM}} = \frac{(N_{\mathrm{FFM}}^{\mathrm{Bhabha}} - N_{\mathrm{FFM}}^{\mathrm{Accidental}})}{\sigma_{\mathrm{FFM}}} \tag{4.1}$$

$$\sigma_{\mathrm{FFM}} = f_{\mathrm{livetime}} \frac{(N_{FFM}^{\mathrm{Bhabha}} - N_{\mathrm{FFM}}^{\mathrm{Accidental}})}{L_{SW}}. \tag{4.2}$$

The OPAL online luminosity is measured by counting the number of Bhabha events which are detected by the FFMs, and then calculating the luminosity using Equation 4.1. The online criteria for a Bhabha event are very simple and are based on an energy sum trigger. If the sum of energy in each of a pair of diagonally opposite (conjugate) modules is above some threshold, the event is considered a Bhabha event. In order to estimate the number of FFM Bhabha triggers produced by uncorrelated coincidences of hits which fake the

Bhabha signature, an “accidental trigger” is also counted. This trigger works in the same way as the Bhabha trigger, except that the energy sums from the left end of OPAL are put into coincidence with the energy sums from the right end of OPAL for the previous bunch crossing. Both of these triggers are described in more detail in Section 4.3. The factor σ_{FFM} is determined using Equation 4.2 where L_{SW} is the integrated luminosity for a run, measured using the Silicon-Tungsten luminometer which was described in Section 3.3. The factor f_{livetime} is the fraction of time that OPAL was able to record an event during the data taking run. OPAL may be unable to record an event during a data taking run for several reasons. Two common causes are that the data acquistion system is reading out an event, or that data taking is paused in order to put a subdetector's data acquistion system under the control of the global data acquistion system. The live time correction is required because Bhabha events in the FFMs are counted while OPAL is unable to record an event, but Bhabha events in the Silicon-Tungsten Luminomiter are not.

4.3 Luminosity and Calibration Triggers

Because the FFM calibration sample is defined by the events selected by the FFM Bhabha and accidental triggers, a detailed explanation of these triggers is necessary. The FFM Bhabha trigger is called FDFAR, and the accidental trigger is called FDFARA.

$$\begin{aligned} FDFAR \;=\; & \\ & ((RF_{\mathrm{sum}} > T_0) \text{ AND } (LN_{\mathrm{sum}} > T_0)) \\ & \text{OR } ((RN_{\mathrm{sum}} > T_0) \text{ AND } (LF_{\mathrm{sum}} > T_0)) \end{aligned} \tag{4.3}$$

The FDFAR trigger signal is defined in Equation 4.3. RF_{sum}, LN_{sum}, RN_{sum} and LF_{sum} are, respectively, the sum of the pulse heights for the RF, LN, RN and LF calorimeter modules. The designation of the modules was explained in Section 4.1. T_0 is the threshold for the constant fraction discriminator which is used to derive a logic signal from the analog sum. It is important to note that an ideal trigger requires the phototube gains to be balanced so that for each compartment the factor which relates the signal from the PMT to the deposited energy is the same. The procedure for balancing the gains to achieve this is described in Section 4.4. The threshold of the discriminators, during the $\sqrt{s} = 183$ GeV data taking in 1997, was 200 mV, which yields an energy threshold of approximately 46 GeV. The energy threshold is obtained from looking at the low energy tail in Figure 4.10, and is not sharp because the PMT gains were not perfectly balanced, as discussed in Section 4.4. The FDFAR trigger is based on the assumption that the electron and positron which participate in a Bhabha scattering reaction are collinear and so should be observed in diagonally opposite modules. This is true for the vast majority of Bhabha events in which initial and final state radiation is small, as shown in Figure 4.4.

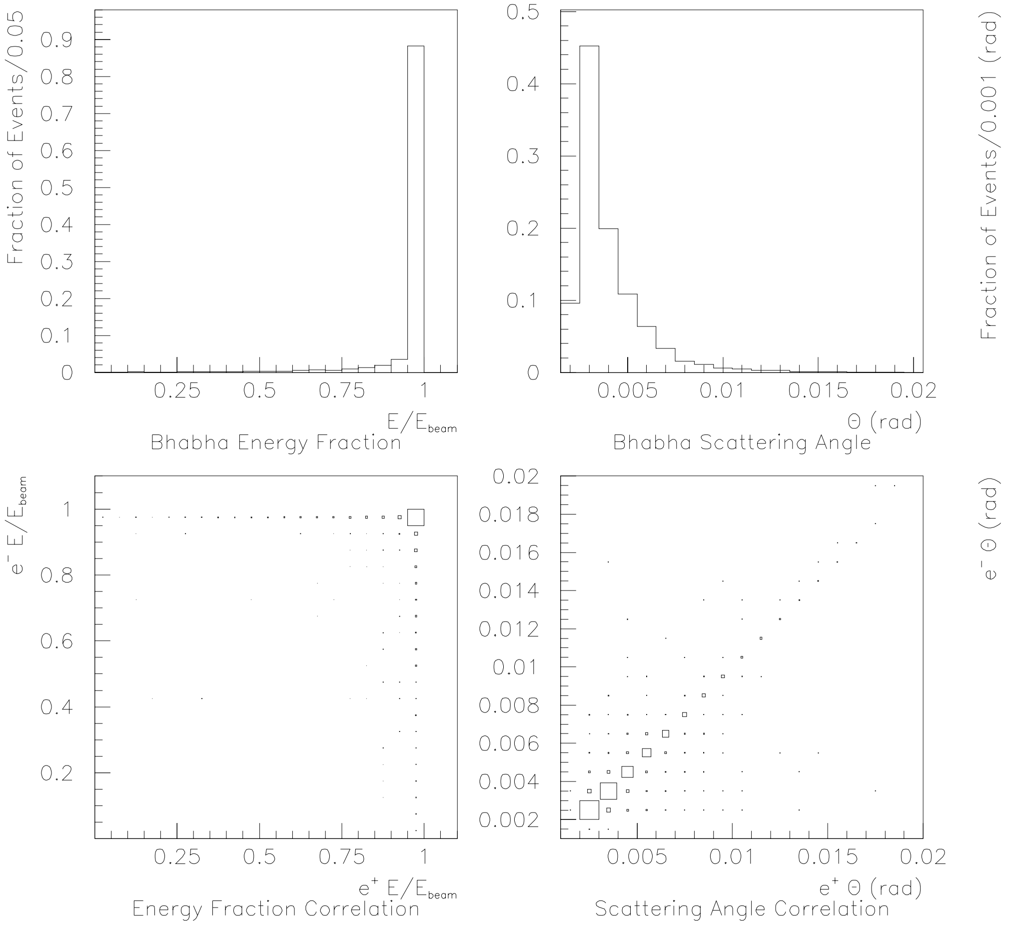

Fig. 4.4: The first two plots show the distributions of scattered particle energy fraction and scattering angle, as generated by BHLUMI. The area of the histograms has been normalized to one. The energy fraction distribution is peaked at the beam energy. The angular distrubtion is peaked at the lowest generated scattering angle, although this does not coincide exactly with the histogram binning. The second two plots show, respectively, the correlation between the energy fractions for scattered electrons and positrons, and the correlation between scattering angles for scattered electrons and positrons.

The main background for Bhabha events in the FFMs is an accidental coincidence in conjugate modules due to off momentum electrons coming from beam-gas interactions in the long straight sections and the beginnings of the arcs of LEP at either end of OPAL. The detailed discussion of this background is postponed until Section 4.8 because some technical points from the calibration procedure are important in understanding the observed background energy distributions. Because of this background, two of the four FFM modules could not be used at all for the physics analysis of the 1997 data which follows, and distributions will only be shown for the Right Near and Left Far modules, which have been used.

$$\begin{aligned} FDFARA \;=\; & \\ & ((RF_{\text{sum}}^{\text{delayed}} > T_0) \text{ AND } (LN_{\text{sum}} > T_0)) \\ & \text{OR } ((RN_{\text{sum}}^{\text{delayed}} > T_0) \text{ AND } (LF_{\text{sum}} > T_0)) \end{aligned} \tag{4.4}$$

The FDFARA trigger signal, defined in Equation 4.4, is used to estimate the rate of the accidental coincidence background. $RF_{\text{sum}}^{\text{delayed}}$ and $RN_{\text{sum}}^{\text{delayed}}$ in Equation 4.4 are the RF_{sum} and RN_{sum} logic signals which have been delayed by one bunch crossing. Since the particles causing the accidental coincidences are uncorrelated, the number of FDFARA triggers estimates the number of accidental coincidences which have contaminated the FDFAR Bhabha sample. This estimate may not be correct if the four bunches are significantly different. LEP is operated with approximately the same current in each bunch, which reduces the possibility of large differences in backgrounds from different bunches. The approximate equality of the currents was checked for representative runs throughout the year. Pulse height information is only available for the non-delayed modules in an FDFARA triggered event, because only the logic signals are delayed.

Because the rate of events satisfying the FDFAR and FDFARA trigger conditions is large, most of the FDFAR and FDFARA trigger signals are only counted by the trigger monitoring system and do not cause the OPAL data acquistion to record an event. These two signals are also, however, logically ORed together and rate limited. The rate limited trigger signal is called FDSPEC. Running at up to 0.1 Hz, this provides an unbiased sample of FDFAR and FDFARA events which are used to calibrate the FFMs. The number of FDFAR and FDFARA trigger signals counted during a period of time are the quantities $N_{FFM}^{\mathrm{Bhabha}}$ and $N_{\mathrm{FFM}}^{\mathrm{Accidental}}$ in Equation 4.1.

4.4 PMT Gain Balancing Procedure

The purpose of the gain balancing procedure is to adjust the gain of each PMT so that each compartment's output signal is related to the deposited energy by the same constant, which is called the calibration constant. This is motivated by the desire to make a simple analog sum of the signals from each compartment for use in the FFM trigger logic, as described in the previous section.

The gain balancing is done in several steps. The first step is to set the initial PMT voltages and make sure that the signals are within the range of the 10 bit ADCs. For 1997, the initial voltages were the same as those used in 1996. During data taking, the voltages were adjusted so that the maximum signals from Bhabha events did not go above the range of the readout ADCs. Once this was accomplished, the data could be used for gain balancing.

In the second step, the calibration constants are determined using the procedure described below in Section 4.6. The third step is to adjust the voltages so that all calibration constants are the same. The second and third steps are iterated until the constants are all approximately equal.

In order to adjust the voltages using the information from the calibration constants, a relation between the PMT gains and the PMT high voltages is needed. Using the LED test system, this relationship was roughly determined. Three PMTs were chosen at random, and the pulse height versus high voltage was measured, for a constant LED test pulse. The results of this test are given in Table 4.1. (As part of the 1997-1998 detector upgrade, the gain versus voltage curves have been measured for all PMTs used in the FFM system.)

The measured points in Table 4.1 have an approximately exponential relationship, as given in Equation 4.5, with $\alpha \approx 0.008$. This expression was used for the 1997 gain balancing. Over the range of values used it is not very different from the more physically motivated relation [21], based on the way in which a PMT works, given in Equation 4.6. The constant β is a function of the number of stages in the PMT and the variation in gain for each stage

PMT 1		PMT 2		PMT 3	
V (kV)	PH (mV)	V (kV)	PH (mV)	V (kV)	PH (mV)
1.10	200	1.16	188	1.20	252
1.15	268	1.21	252	1.25	328
1.20	336	1.26	336	1.30	408
1.25	404	1.31	416	1.35	496
1.30	460	1.36	512	1.40	572

Tab. 4.1: The applied high voltage and pulse height (PH) for a constant LED test pulse. The three tubes were chosen at random, and the mean applied high voltage is the operating voltage from 1996.

Compartment	Right Near Ratio	Left Far Ratio
Upper Outer	0.73	1.23
Upper Inner	1.00	0.78
Upper Front	1.26	1.06
Lower Outer	0.52	0.59
Lower Inner	0.89	1.05
Lower Front	1.59	1.29

Tab. 4.2: The ratios of the calibration constants for each compartment to the average calibration constant for the module, after the gain balancing procedure described in Section 4.6 was performed in 1997. In the ideal case, all of the calibration constants would be the same, and all of these ratios would be 1. The errors on the ratios are typically a few percent.

with applied voltage. For the measurements in Table 4.1, $\beta \approx 5.5$.

$$\frac{G}{G_0} \approx e^{\alpha(V-V_0)} \tag{4.5}$$

$$\frac{G}{G_0} \approx \left(\frac{V}{V_0}\right)^{\beta} \tag{4.6}$$

The results of the gain balancing procedure for 1997 are given in Table 4.2.

4.5 Detector Simulation

A simulation of the FFMs has been implemented using the GEANT [22] detector simulation package, including the effects of the quadrupoles and of the beam pipe geometry. The geometry and composition of the detectors are taken from the design specifications and measurements of the actual detectors. The positions of the detectors are given as parameters to the simulation, and the method used to estimate the actual detector positions is described in Section 4.9.

As particles go from the interaction point to the FFM modules, they pass through the LEP mini-β quadrupoles [23], which are the final focusing quadrupoles around OPAL. In the simulation, particle four-vectors are generated by a separate Monte Carlo generator, and the propagation from the interaction point through the quadrupoles is simulated according to a set of transformation matrices [24]. This is more efficient than simulating the quadrupoles in GEANT. The transformation consists of a field free drift to the quadrupole, the quadrupole matrix transformation, and a drift to the final z position. Denoting the particle momentum along the i^{th} axis as P_i, the treatment used here requires that $P_{\mathrm{z}} >> P_{\mathrm{x}}, P_{\mathrm{y}}$. A vector is defined

$$\vec{v} = \begin{pmatrix} x \\ x' \\ y \\ y' \end{pmatrix} \tag{4.7}$$

where x and y are the coordinates of the particle and

$$x' = P_{\mathrm{x}}/P_{\mathrm{z}} \tag{4.8}$$

$$y' = P_{\mathrm{y}}/P_{\mathrm{z}} \tag{4.9}$$

are the divergences, essentially the normalized transverse components of the momentum. A drift is then described by the matrix

$$\mathbf{M}^{\mathrm{drift}} = \begin{pmatrix} 1 & D & 0 & 0 \\ 0 & 1 & 0 & 0 \\ 0 & 0 & 1 & D \\ 0 & 0 & 0 & 1 \end{pmatrix} \tag{4.10}$$

where D is the length of the drift. A finite-length ideal quadrupole is described by the matrix

$$\mathbf{M}^{\mathrm{quad}} = \begin{pmatrix} \cosh\phi & \frac{1}{\sqrt{|k_0|}}\sinh\phi & 0 & 0 \\ \sqrt{|k_0|}\sinh\phi & \cosh\phi & 0 & 0 \\ 0 & 0 & \cos\phi & \frac{1}{\sqrt{|k_0|}}\sin\phi \\ 0 & 0 & -\sqrt{|k_0|}\sin\phi & \cos\phi \end{pmatrix} \tag{4.11}$$

where k_0 is the field gradient and $\phi = \sqrt{|k_0|}l$. The total quadrupole transformation is given by

$$\vec{x}_{\mathrm{ff}} = \mathbf{M}_2^{\mathrm{drift}}\mathbf{M}^{\mathrm{quad}}\mathbf{M}_1^{\mathrm{drift}}\vec{x}_{\mathrm{IP}} \tag{4.12}$$

For the FFM simulation, the first drift is 3.88 m, the quadrupole transformation matrix, provided by the LEP machine group, is

$$\mathbf{M}^{\mathrm{quad}} = \begin{pmatrix} 1.336383 & 2.219594 & 0 & 0 \\ 0.354082 & 1.336383 & 0 & 0 \\ 0 & 0 & 0.697557 & -0.2861987 \\ 0 & 0 & 1.793984 & 0.697557 \end{pmatrix} \tag{4.13}$$

and the second drift is 1.3475 m.

In order to simulate interactions with the beam pipe, the last drift stops approximately half a meter before the position of the FFM modules and the particles are propagated from there by GEANT. The section of the beam pipe which is simulated is shown in Figure 4.1 and consists of three parts; a 192.5 mm long round section with an inner radius of 78 mm, a 35 mm long conical section 1.5 mm thick, and a 125 mm long round section with inner radius 60 mm. In reality, the third section was oval, with a minor radius of 60 mm and a major radius of 78 mm. The cross section of the second piece made a smooth transistion from the cross section of the first piece to the cross section of the third piece. This particular geometry does not exist in GEANT, so the circular and conical geometries were used as an approximation.

The FFM modules are located on either side of the smaller straight section. Most particles which are measured with the FFM pass through the conical section of beam pipe, which provides a window from the machine vacuum to the detector. It is assumed that particles which leave the machine vacuum before reaching this vacuum window shower in the LEP structures around the beam pipe and are not observed. For this reason, particles whose position after the final drift is at a radius greater than the inner radius of the first section of beam pipe in the simulation are not allowed to propagate to the FFMs. Figure 4.5 is a detailed schematic of the area around the FFMs inside the cantilever which supports the LEP low-β quadrupole and shows a

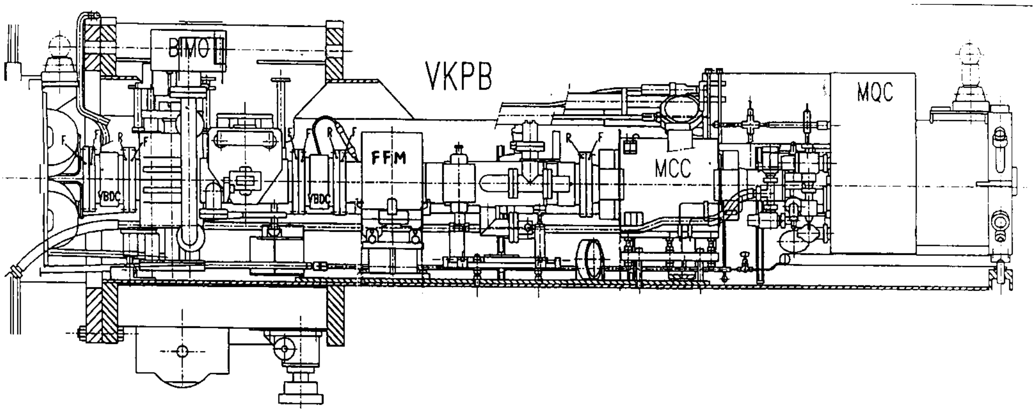

Fig. 4.5: Schematic of the region around the FFM's inside the cantilever supporting the mini-β quadrupole. The interaction point is to the right of the figure. The object labeled MQC is the rear of the low-β quadrupole. MCC labels a small corrector dipole magnet. The rectangular object slightly to the right of the FFM is an ion pump.

number of the LEP structures.

The GEANT simulation of the FFMs works in the following way. The geometry and composition of the FFMs are defined in a standard format implemented in several FORTRAN subroutines. Using this information, the general purpose routines in GEANT are able to track particles through the detectors and sample the interactions which take place, including the deposited energy. In order to allow flexible use of the simulation a number of parameters, such as the detector positions, are taken as input. For any desired values of the parameters a simulation run is performed in which simulated physics events are produced by a separate Monte Carlo generator. For each event, the particle vectors are passed to GEANT which tracks the particles through the detectors. The energy deposited in each scintillator layer is stored. At the end of simulation for an event the total deposited energy for each scintillator layer is available.

In the real detector, the deposited energy causes excitations of the scintillating material; when these excitations decay, light is emitted. This light is emitted isotropically and travels through the scintillator until it leaves one of the faces of the slab. One face of the scintillator slab is separated from a slab of wavelength shifting material by a small air gap. Once the scintillation light enters the wavelength shifting material, it is absorbed and re-emitted at a different wavelength. The wavelength shifted light is produced isotropically and propagates to the faces of the wavelength shifting slab. One of the faces of the wavelength shifting slab is attached to a light guide, which uses total internal reflection to direct the light onto the face of the PMT. In principle, a light guide could be attached directly to the scintillator, but the use of the wavelength shifter allows for a more compact design of the calorimeter.

The purpose of the PMT is to convert the photonic signal from the wavelength shifter to an electronic signal. This is accomplished using the photoelectric effect to produce electrons from the incident photons, and then using a series of dynodes, maintained at different voltages, to multiply the number of electrons. The multiplication takes place because the electrons are accelerated by the voltage difference between successive dynodes, and at each dynode one incident electron produces several secondary electrons, which are then accelerated to the next dynode. The electrons from the final dynode are collected on the anode, which produces the output signal.

The signal from the anode travels approximately 50 m on coaxial cable and is input for a charge integrating ADC, which digitizes the pulse and provides an integer value proportional to the integrated charge.

$$N_{\mathrm{ADC}} = \mathrm{INT}(E_{\mathrm{deposited}} f_1 f_2 f_3 f_4 f_5 f_6 f_7) \tag{4.14}$$

Rather than using Monte Carlo techniques to simulate the discrete processes involved in scintillation, light transport and PMT operation, an estimate of the number of ADC counts for the amount of deposited energy is made using Equation 4.14. The multiplicative constants in 4.14 are given in Table 4.3, along with an explanation of each constant. It is clear that a single constant could replace the seven constants in Equation 4.14, since the sixth constant is tuned to fit the data. This is not done, however, in order to simulate the statistical nature of the light collection process. A Poisson distribution whose mean is the deposited energy times the first constant is sampled, the result is multiplied by the second constant and a Binomial distribution with the new mean is sampled. This is repeated for each constant until f_6, using Binomial distributions. The last two constants do not contribute to statistical fluctuations, but do allow a direct analogy to be made between the steps in the physical detector and in the simulation. The constants given in Table 4.3 are reasonable estimates taken from, for example [25]. The tuned gain constants for each compartment used in the final analysis are given in Table 4.4.

f1	$10\ \frac{\text{photons}}{\text{keV}}$	Conversion from deposited energy to scintillation photons [7].
f2	0.125	Geometrical factor for light collection from one face of a scintillator slab
f3	0.40	Efficiency of the wavelength shifter
f4	0.125	Geometrical factor for light collection from one face of a wavelength shifting slab
f5	$0.33\ \frac{\text{photo-electrons}}{\text{photon}}$	Quantum efficiency for a PMT
f6	see Table 4.4	The unknown PMT gain (varies from channel to channel)
f7	$6.4 \times 10^{-7}\ \frac{\text{ADC counts}}{\text{electron}}$	conversion from integrated charge to ADC counts

Tab. 4.3: The values used as constants in Equation 4.14 for conversion from deposited energy to ADC counts in the FFM Monte Carlo simulation.

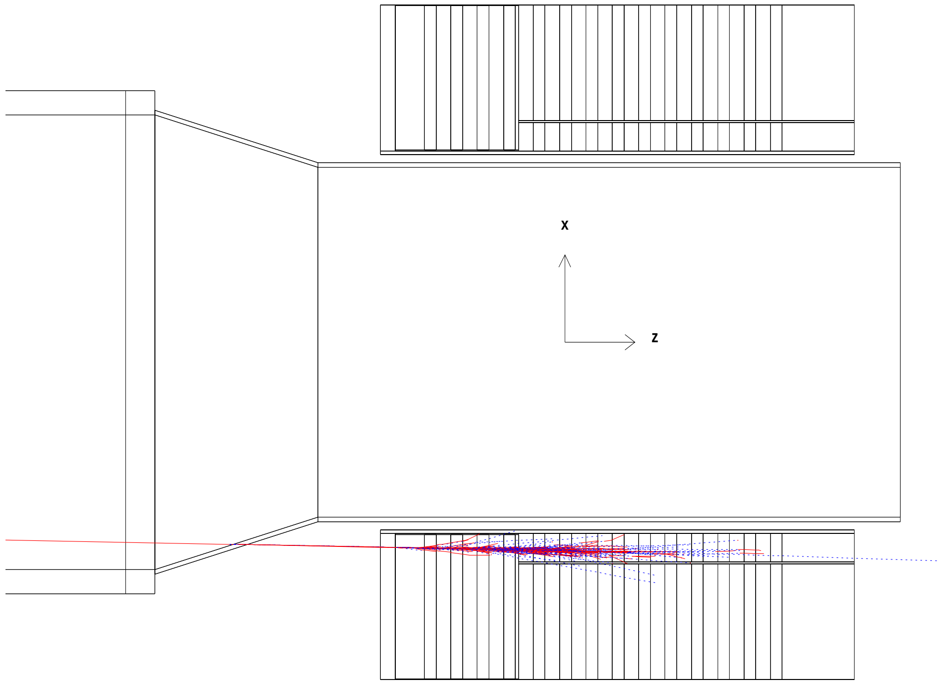

Fig. 4.6: Top view of an FFM module and shower, as simulated by GEANT. Dotted (red) lines are electrons or positrons and dashed (blue) lines are photons. All particles produced in the simulation with more than 100 MeV are shown.

Compartment	Gain
RN Upper Outer	4.00×10^4
RN Upper Inner	4.00×10^4
RN Upper Front	5.71×10^4
RN Lower Outer	4.00×10^4
RN Lower Inner	4.44×10^4
RN Lower Front	4.44×10^4
LF Upper Outer	1.33×10^4
LF Upper Inner	3.57×10^4
LF Upper Front	7.27×10^4
LF Lower Outer	4.44×10^4
LF Lower Inner	2.85×10^4
LF Lower Front	4.44×10^4

Tab. 4.4: The tuned PMT Gain constants for each compartment, used in the FFM Monte Carlo simulation.

4.6 Energy Calibration Procedure

In order to determine the energy and position of a shower in an FFM module, the following method is used. Each module is considered as a set of compartments, $\mathbf{M}$. The uncorrected energy in a module is

$$E^{\mathrm{unc}}(C_i) = \sum_{i \in \mathbf{M}} C_i (A_i - P_i) \tag{4.15}$$

where A_i is the number of ADC counts measured in the i^{th} compartment, P_i is the pedestal value for that compartment, and C_i is the calibration constant for that compartment.

The pedestal values for each compartment are determined from the data. During a data taking run, OPAL records a sample of events at random, which are not required to satisfy any physics selection criteria. The FFMs do not contain an energy deposit for the majority of these events. The pedestal for each FFM compartment is the mean of a gaussian fitted to the ADC count distribution for the randomly triggered events.

The calibration constants are determined by considering a set, **B**, of Bhabha events. For the Monte Carlo simulation, these Bhabha events are generated using the BHLUMI event generator [26]. Bhabha events are selected in the data as described in Section 4.3. To a good approximation, each Bhabha electron carries the beam energy, as shown in Figure 4.4. The calibration constants are fitted by minimizing the objective function

$$X = \sum_{j \in \mathbf{B}} (E_j^{\mathrm{unc}}(C_i) - E^{\mathrm{Beam}})^2 \tag{4.16}$$

which is proportional to the square of the reconstructed width of the energy distribution for Bhabha events. Figure 4.7 and Figure 4.8 are, respectively, the raw ADC distributions for individual compartments and the summed distributions for FFM modules. Although there is no clear peak in the individual compartment distributions, there is a clear peak in the summed distributions. The peaks for the summed data and Monte Carlo do not have the same mean, however. Given the good agreement between data and Monte Carlo for the individual module distributions, this discrepancy indicates that the correlation between energy deposits in different compartments is not properly modelled in the Monte Carlo. This discrepancy is removed by the calibration procedure, which minimizes the width of the summed peak in order to find the calibration constants. The calibrated energy distributions are shown in Figure 4.9. The width of the calibrated peaks for data and the estimated off-momentum background are shown in Figure 4.10.

It is important to note the underlying assumption of the calibration, which is the existence of a single peak, at the beam energy, in the summed energy distribution. This condition may not be met if, for example, there is contamination in the calibration sample of events from some other source. Such contamination does occur during some periods of data taking because of off-momentum electrons which are bent into the FFMs by the beam optics. Random coincidences of two such electrons in diagonally opposite modules result in contamination of the Bhabha sample. If such coincidences occur too often, the calibration fails.

Equation 4.16 is minimized using the MINUIT package [27]. The minimization is iterated, applying event selection cuts before each iteration. Events used in the first iteration must satisfy

$$\sum_{i \in \mathbf{M}} (A_i - P_i) > 250 \text{ counts} \tag{4.17}$$

while events used in the subsquent iterations must satisfy

$$E^{\text{unc}} > 0.5 E^{\text{Beam}} \text{ AND } E^{\text{unc}}_{\text{conj}} > 0.8 E^{\text{Beam}} \tag{4.18}$$

where $E^{\text{unc}}_{\text{conj}}$ is the energy in the conjugate module. The condition for the first iteration is used to separate events which have essentially no energy deposit in a given module from those which do have a deposit. This is necessary because Bhabha events deposit energy in two of the four modules and only

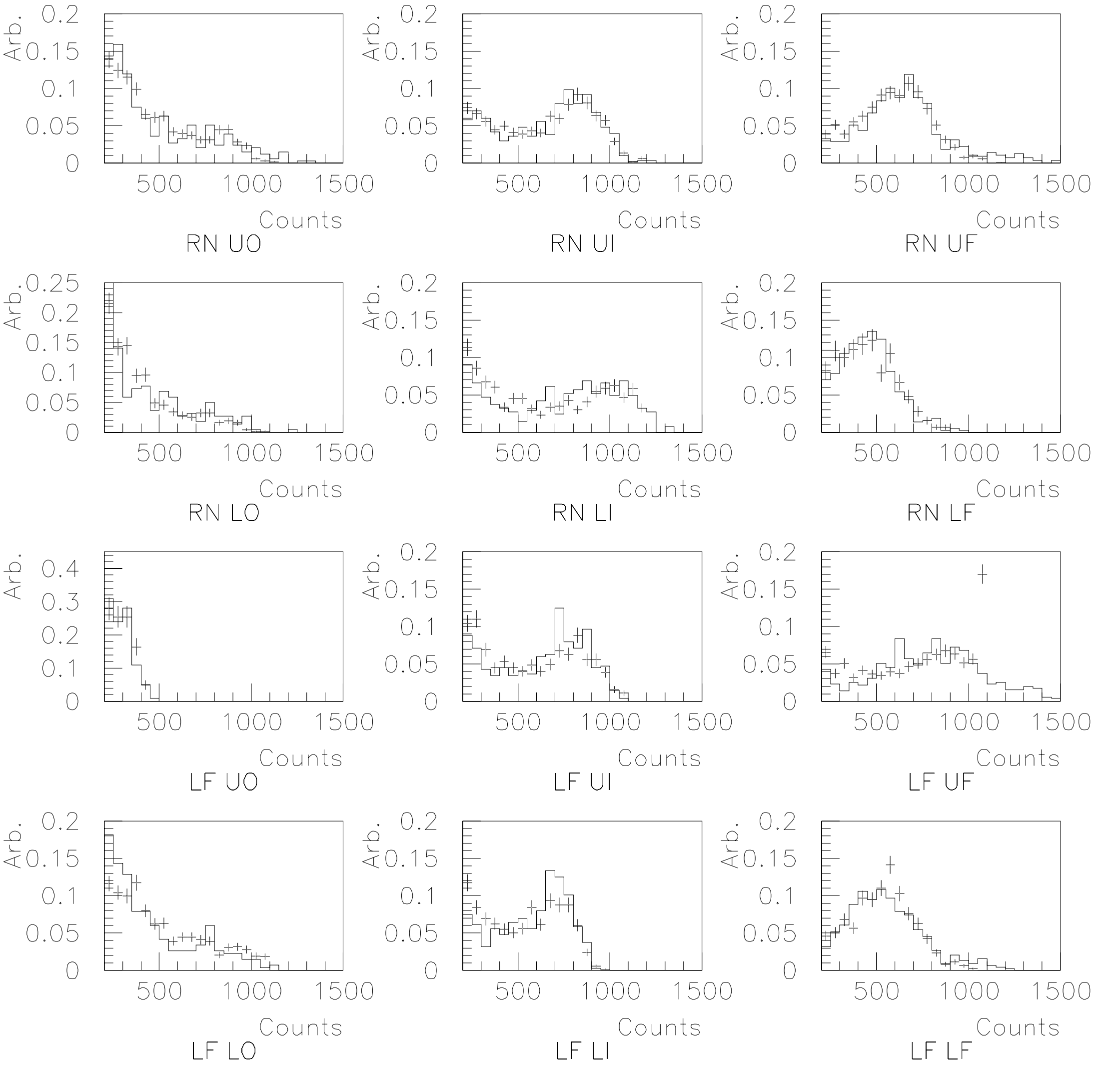

Fig. 4.7: Distributions of pedestal subtracted ADC counts in the individual compartments for the FFM modules used in the doubly tagged analysis. The points with error bars are data from a typical run, while the open histograms are from a Monte Carlo simulation of the FFMs at their nominal positions.

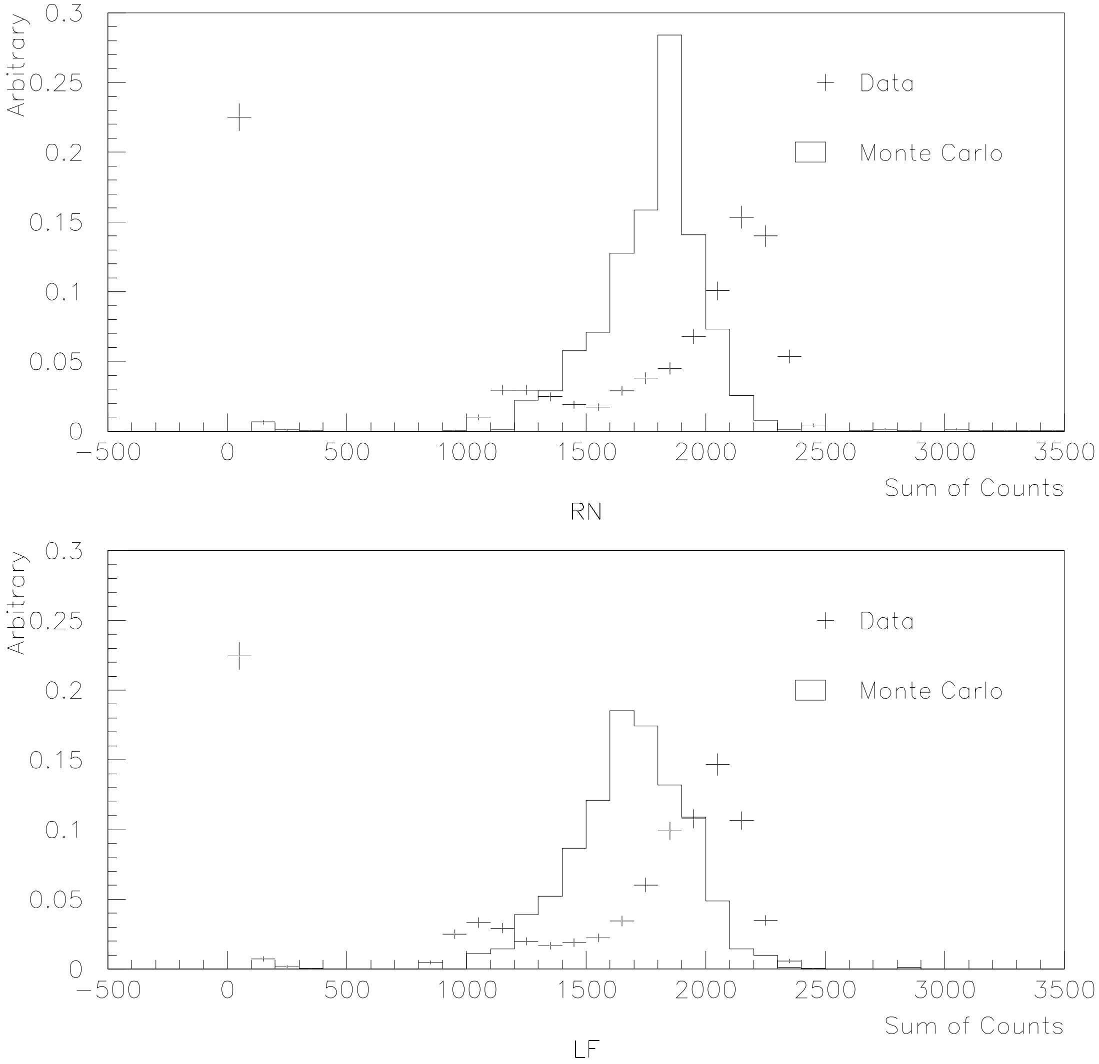

Fig. 4.8: Distributions of the sum of pedestal subtracted ADC counts for the FFM modules used in the doubly tagged analysis, before calibration. The points with error bars are data from a typical run, while the open histograms are from a Monte Carlo simulation of the FFMs at their nominal positions. The counts in the lowest bins come from events in which these modules were the "spectator" modules.

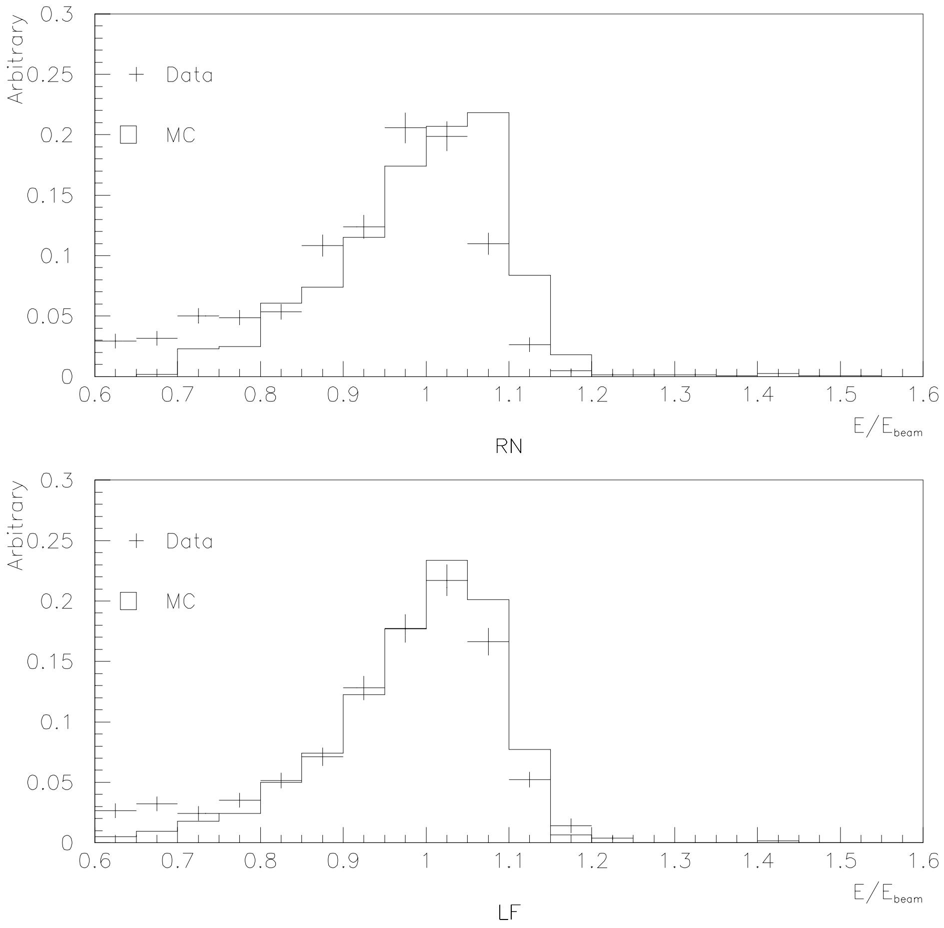

Fig. 4.9: Distribution of reconstructed energy for the RN and LF modules for data and Monte Carlo. The Monte Carlo distributions were made using the best estimate for the free parameters. Each distribution is normalized to have an area of 1, so that the shapes can be compared. Note that the offset seen between data and Monte Carlo for the raw sums in Figure 4.10 is no longer present.

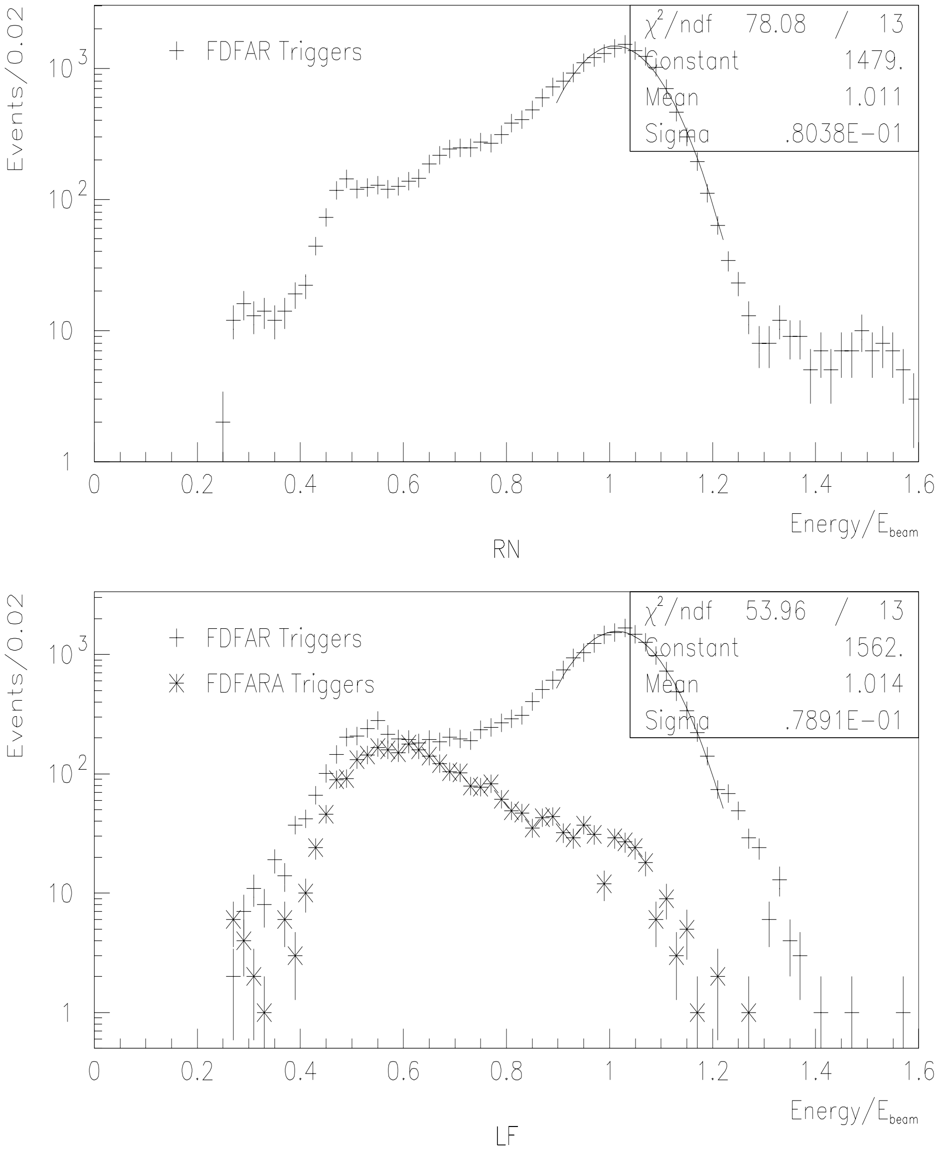

Fig. 4.10: Distributions of fractional energy for the Right Near and Left Far modules, after calibration. The crosses with error bars represent events satisfying the FDFAR trigger condition, while the asterisks with error bars represents events satisfying the FDFARA trigger condition. The asterisks with error bars are absent for the Right Near distribution because only the logic signal was delayed, and the ADC values for the previous bunch were not recorded.

the ADC pedestal is expected in the other two “spectator” modules for that event. The cut relies on an initial loose balancing of the PMT gains, so that a peak in the sum of ADC count distribution occurs for Bhabha events, and is well separated from the pedestal peak. The summed ADC count distributions for the RN and LF modules are shown in Figure 4.8, where a clear separation between the pedestal peak and the signal peak is evident.

4.7 Reconstruction of the Momentum of the Initial Electron

The Moliére radius for an electromagnetic shower in lead is 1.56 cm, so showers are expected to deposit some energy in all compartments, for the whole of the clear acceptance of the detector. Once the calibration constants have been fitted, an energy for each compartment can be obtained

$$E_i = C_i(A_i - P_i) \tag{4.19}$$

and the total energy in the module is $E_{\text{tot}} = \sum_i E_i$, where the variables are defined as before. The fractional energy deposition in different compartments depends on the shower position within the module, so that a position measurement can be made using energy asymmetries;

$$\begin{aligned} \mathrm{X}_{\text{asym}} &= \frac{(E_{uo} + E_{lo}) - (E_{ui} + E_{li})}{(E_{uo} + E_{lo}) + (E_{ui} + E_{li})} && (4.20) \\ \mathrm{Y}_{\text{asym}} &= \frac{(E_{uo} + E_{ui} + E_{uf}) - (E_{lo} + E_{li} + E_{lf})}{E_{\text{tot}}} && (4.21) \\ \mathrm{Z}_{\text{asym}} &= \frac{(E_{uf} + E_{lf}) - (E_{uo} + E_{ui} + E_{lo} + E_{li})}{E_{\text{tot}}}. && (4.22) \end{aligned}$$

The $\mathrm{X_{asym}}$ is related to the shower position in the horizontal plane, the $\mathrm{Y_{asym}}$ is related to the shower position in the vertical plane, and the $\mathrm{Z_{asym}}$ is related to profile of the shower with depth in the module.

The asymmetries from a shower contain all of the available information about its position within the FFM module. The next task is to relate the asymmetries to a set of external coordinates so that the momentum vector of the parent electron can be reconstructed. Because no testbeam data is available, the ideal relations between asymmetries and external coordinates are determined using the Monte Carlo simulation of the detector. Monte Carlo Bhabha events are passed through the detector simulation, and for these simulated events the asymmetry values and the position of the incident electron are known. Polynomial functions $x(\mathrm{X_{asym}})$ and $y(\mathrm{Y_{asym}})$ are fit to the correlation histograms shown in Figure 4.11, and these functions give the ideal position of an incident particle for a particular set of asymmetries.

The procedure for reconstructing the incident particle position assumes that the positions of the modules and the beam is well known, in the external coordinate system. In fact, there is uncertainty in the position of the beam and of the modules. These uncertainties are discussed in more detail in Section 4.9.2.

Once the position and energy of the shower have been determined at the FFM, it is necessary to reverse the quadrupole transformation. The transformation given in Equation 4.12 is used to accomplish this. The position of the incident electron at the FFM module is known, and the position of the

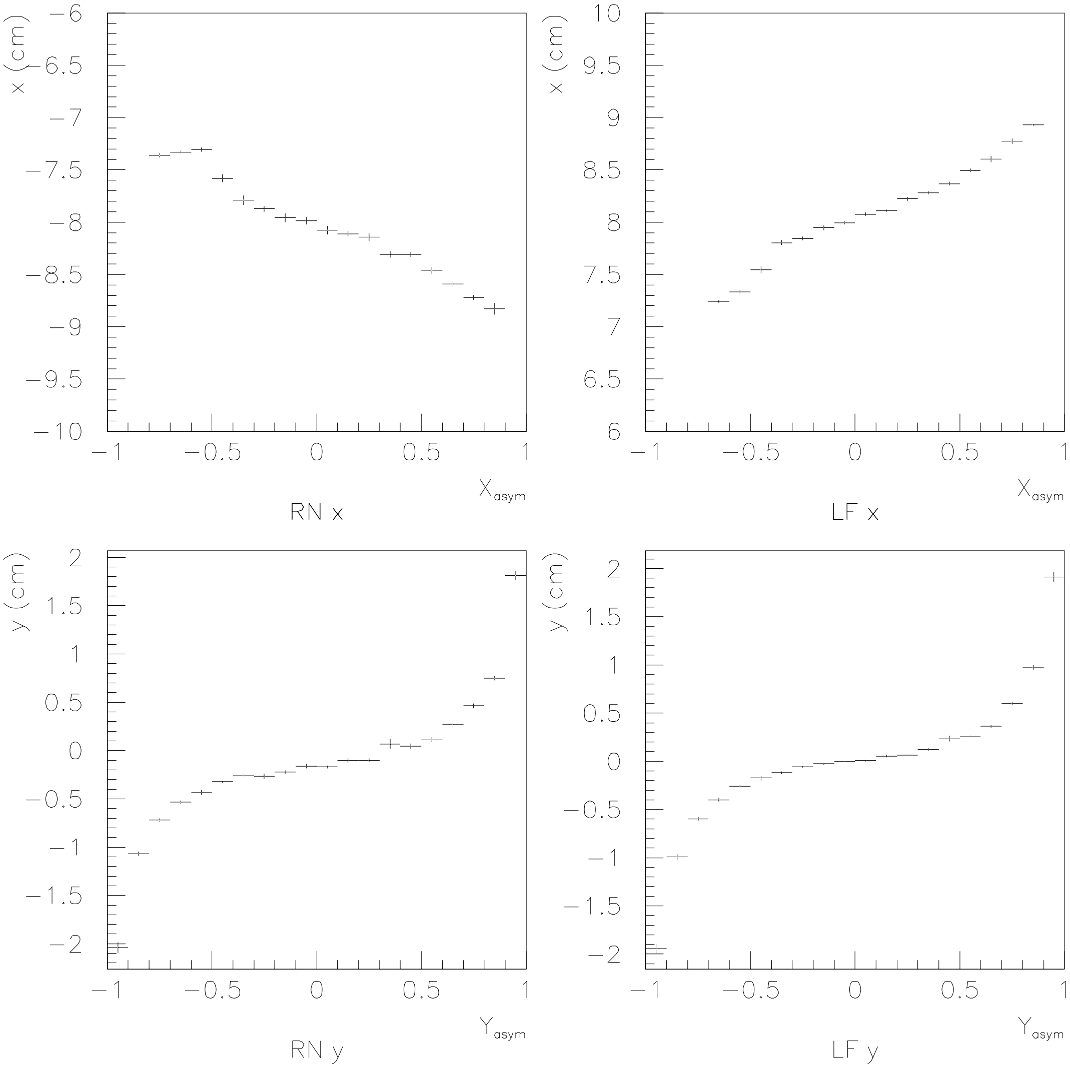

Fig. 4.11: Monte Carlo results show the correlation between the asymmetries and the associated shower coordinate.

interaction point is known, so that we have a system of four equations and four unknowns. The four unknowns are the horizontal and vertical divergences before and after the quadrupole transformation. Defining the vectors $\vec{x}_{\mathrm{ff}}$ and $\vec{x}_{\mathrm{IP}}$ as

$$\vec{x}_{\mathrm{ff}} = \begin{pmatrix} x_{\mathrm{ff}} \\ x'_{\mathrm{ff}} \\ y_{\mathrm{ff}} \\ y'_{\mathrm{ff}} \end{pmatrix} \tag{4.23}$$

$$\vec{x}_{\mathrm{IP}} = \begin{pmatrix} x_{\mathrm{IP}} \\ x'_{\mathrm{IP}} \\ y_{\mathrm{IP}} \\ y'_{\mathrm{IP}} \end{pmatrix} \tag{4.24}$$

the unknown divergences are solved for using Equation 4.12;

$$x'_{\mathrm{IP}} = \frac{x_{\mathrm{ff}} - x_{\mathrm{IP}}(\cosh\phi + D_2\cosh\phi)}{D_1\cosh\phi + \frac{1}{\sqrt{|k_0|}}\sinh\phi + D_1 D_2\sqrt{|k_0|}\sinh\phi + D_2\cosh\phi} \tag{4.25}$$

$$y'_{\mathrm{IP}} = \frac{y_{\mathrm{ff}} - y_{\mathrm{IP}}(\cos\phi + -\sqrt{|k_0|}\sin\phi D_2)}{D_1\cos\phi + \frac{1}{\sqrt{|k_0|}}\sin\phi + -\sqrt{|k_0|}\sin\phi D_1 D_2 + D_2\cos\phi} \tag{4.26}$$

$$x'_{\mathrm{ff}} = \sqrt{|k_0|}\sinh\phi(x_{\mathrm{IP}} + D_1 x'_{\mathrm{IP}}) + \cosh\phi x'_{\mathrm{IP}} \tag{4.27}$$

$$y'_{\mathrm{ff}} = -\sqrt{|k_0|}\sin\phi(y_{\mathrm{IP}} + D_1 y'_{\mathrm{IP}}) + \cos\phi y'_{\mathrm{IP}}. \tag{4.28}$$

Since $P_{\mathrm{z}} \approx E$, equations 4.8 and 4.9 give the momentum of the initial electron as

$$P_{\mathrm{x}} = x'_{\mathrm{IP}}E \tag{4.29}$$

$$P_{\mathrm{y}} = y'_{\mathrm{IP}}E \tag{4.30}$$

$$P_{\mathrm{z}} = E. \tag{4.31}$$

4.8 Machine Background

Background from the LEP beams is a crucial issue in this thesis, because this background contaminates both the calibration and signal data samples. For the calibration sample, a random coincidence of two high energy FFM clusters can fake the Bhabha signature. For the signal sample, a random coincidence of a single high energy FFM cluster and a genuine singly tagged event can fake the doubly tagged signature. For the 1997 data sample, background rates were sufficiently high that two of the four FFM modules could not be calibrated, and thus could not be used for the doubly tagged analysis. In addition, the machine background prevented one module from being used for part of the data sample, even though it could be calibrated. In total, only approximately 37.5% of the potential signal sample could be used. For this reason, it is important to understand the origin of the machine background.

The machine background comes from beam particles which have lost some energy. Energy loss occurs because of bremsstrahlung from the residual gas molecules in the LEP vacuum chamber. Once a beam particle has lost energy, the LEP collider acts as a very complicated spectrometer. If the position at which a particle loses energy and the amount of energy loss are known, the point at which the particle leaves the LEP vacuum chamber can be determined. Georg von Holtey of the CERN SL division has simulated the LEP off-momentum background using a modified version of the TURTLE [28] beam line simulation program.

The simulation is configured to include all of the optical elements for 600 m on one end of the experiment, which includes all of the straight section and approximately 6.5% of the arc. The residual gas is assumed to have a constant pressure over this entire section of the accelerator. Some information about the pressure profile is available, and there are known to be variations of pressure in the straight section. The pressure in the arcs is expected to be higher than the pressure in the straight section, because synchrotron radiation from the beams, as they are bent in the arc, causes outgassing from the vacuum chamber. The results of the simulation thus only give a qualitative description of the background.

A number of distributions from the simulation provide insight into the source of off-momentum background. The first two plots in Figure 4.12 show the distributions of the relative energy of the off-momentum particles striking the detector, for the Near and Far module, respectively. Two peaks are present in each distribution, but a clear asymmetry is present; the peak above 70% of the beam energy is much larger for the Near module than for the Far module. The peak below 70% of the beam energy is approximately the same for both modules. The second pair of plots in Figure 4.12 show the distributions of relative energy versus the z position at which the bremsstrahlung occured, for the Near and Far module respectively. From these plots, the origin of the two peaks becomes clear. The lower energy peaks come from bremsstrahlung in the straight section, with lower energy particles coming from nearer the detector. The higher energy peaks come from bremsstrahlung at the beginning of the arc. The vacuum pressure is expected to be higher there than in the straight section, so the higher energy peaks might be expected to be relatively larger than the low energy peaks in the data. Local pressure variations in the straight section may also causes certain parts of the low energy peak to be enhanced, but this will not affect the asymmetry between the Far and Near higher energy peaks.

Because the detectors are asymmetric in phi, the distribution of off-momentum particles in the xy plane is also important. The x distribution, y distribution, and the correlation of x and y are shown in Figure 4.13, for off-momentum particles with more than 70% of the beam energy. The asymmetry between near and far is clearly evident. The off-momentum particles lie mainly along the x axis, so that the vast majority fall within the detector acceptance. Figures 4.14 through 4.17 show the energy distribution in each of the FFM modules, for randomly triggered events. The right end of OPAL has more off-momentum activity than the left end, implying a worse vacuum on the left side of OPAL, which is in agreement with observations of the machine group. There is also a distinct asymmetry between Near and Far modules, in agreement with the TURTLE simulation. A sharp increase in background is observed between periods 85 and 86, when a LEP component was replaced. This background declines during the rest of the year. The qualitative features of the data agree with those of the TURTLE simulation.

The effect of the off-momentum background on calibration is shown in

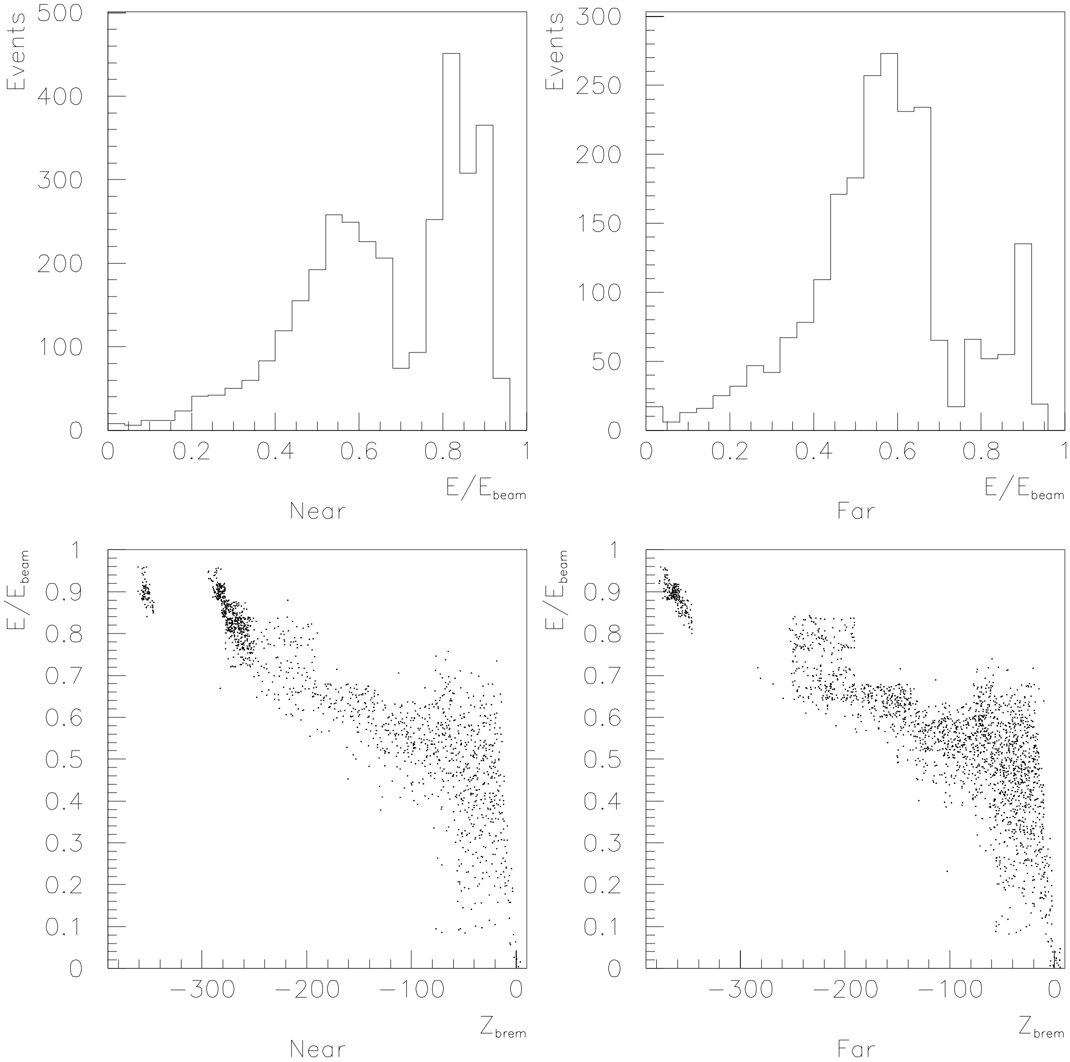

Fig. 4.12: Off-momentum Energy Distributions from the TURTLE simulation for electrons striking the FFMs. The First pair of plots shows the energy distribution for the Near and Far modules. The second pair of plots shows the correlation of the off-momentum particle energy with the z position, in meters, of the bremsstrahlung which caused the energy loss.

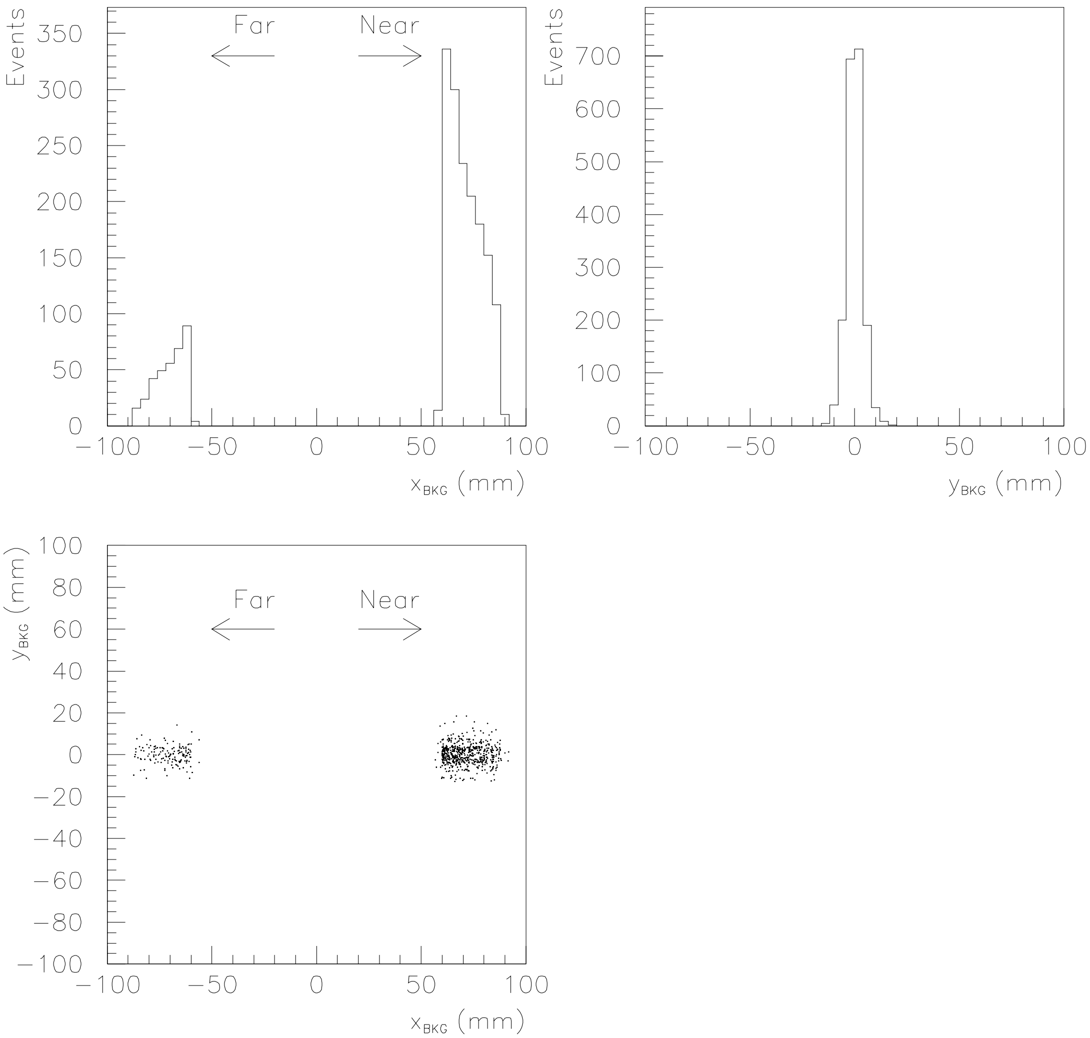

Fig. 4.13: TURTLE simulation of off-momentum backgrounds. For all of the distributions shown, only events with more than 70% of the beam energy were selected. The first plot shows the distribution of high energy off-momentum particles in x, while the second shows the distribution in y. The third plot shows the correlation in x and y. The background almost entirely falls within the acceptance of the Far Forward Monitors.

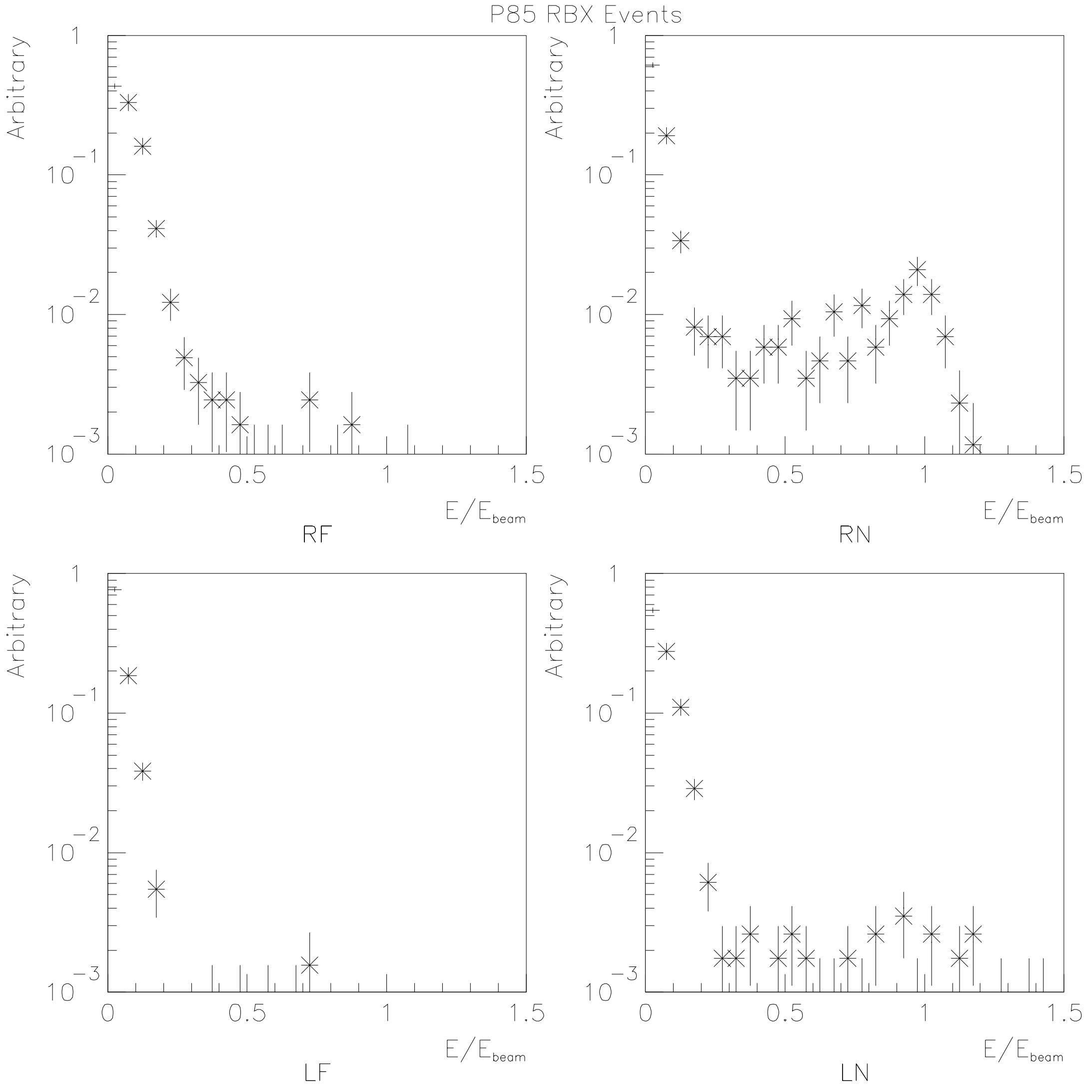

Fig. 4.14: The FFM energy distributions for random triggers for OPAL Period 85 show qualitative features predicted by the TURTLE Monte Carlo simulation, namely the two Near modules record background close to the beam energy while the Far modules do not.

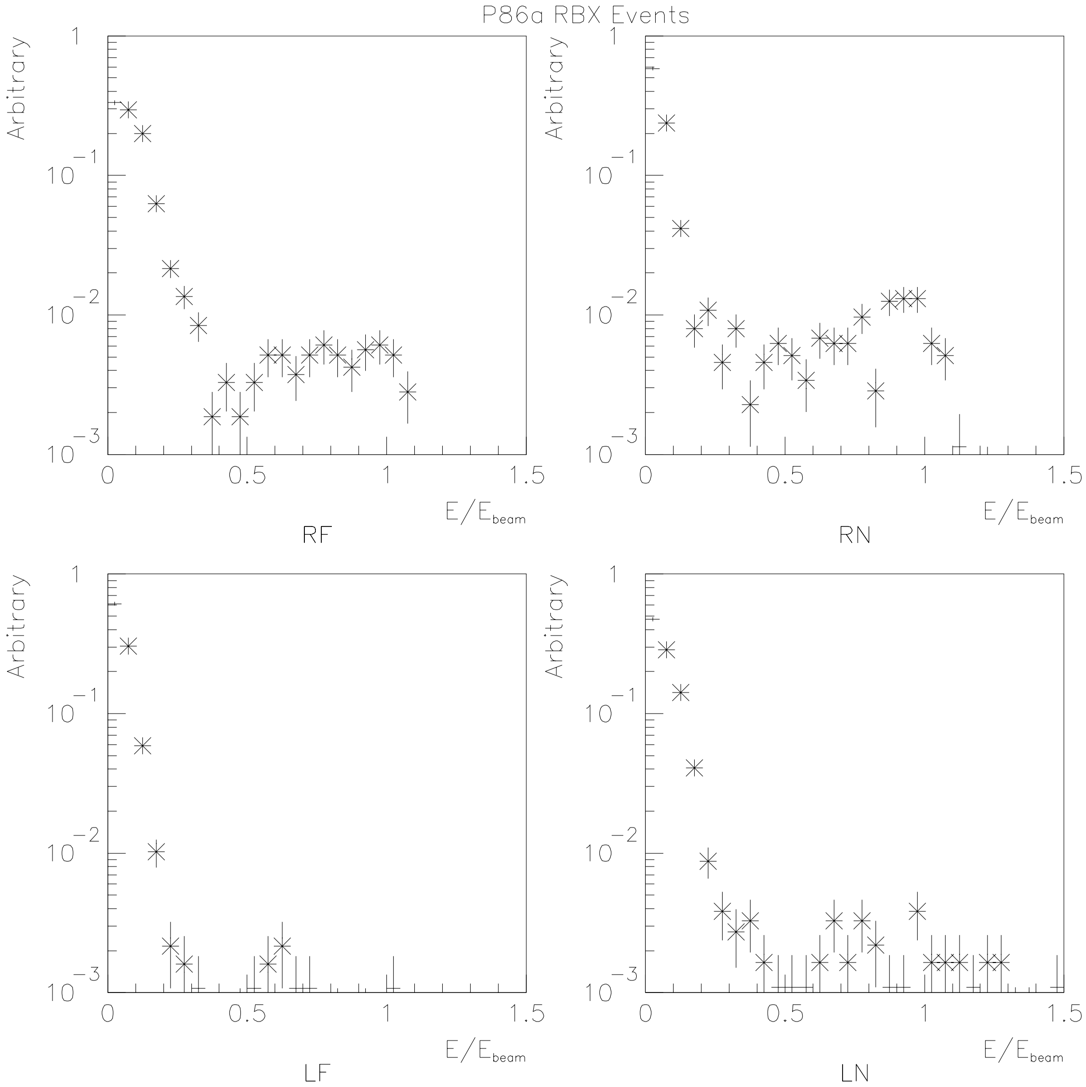

Fig. 4.15: The FFM energy distributions for random triggers during OPAL Period 86a show a different background distribution than seen in Period 85. This is because the vacuum on the Left end of OPAL became worse when a LEP component was replaced. The background in the Right Far module did not extend to the beam energy, as seems to be indicated by the plot. Because the background dominated the Bhabha calibration sample, the background peak was moved to the beam energy. This is seen in Figure 4.19.

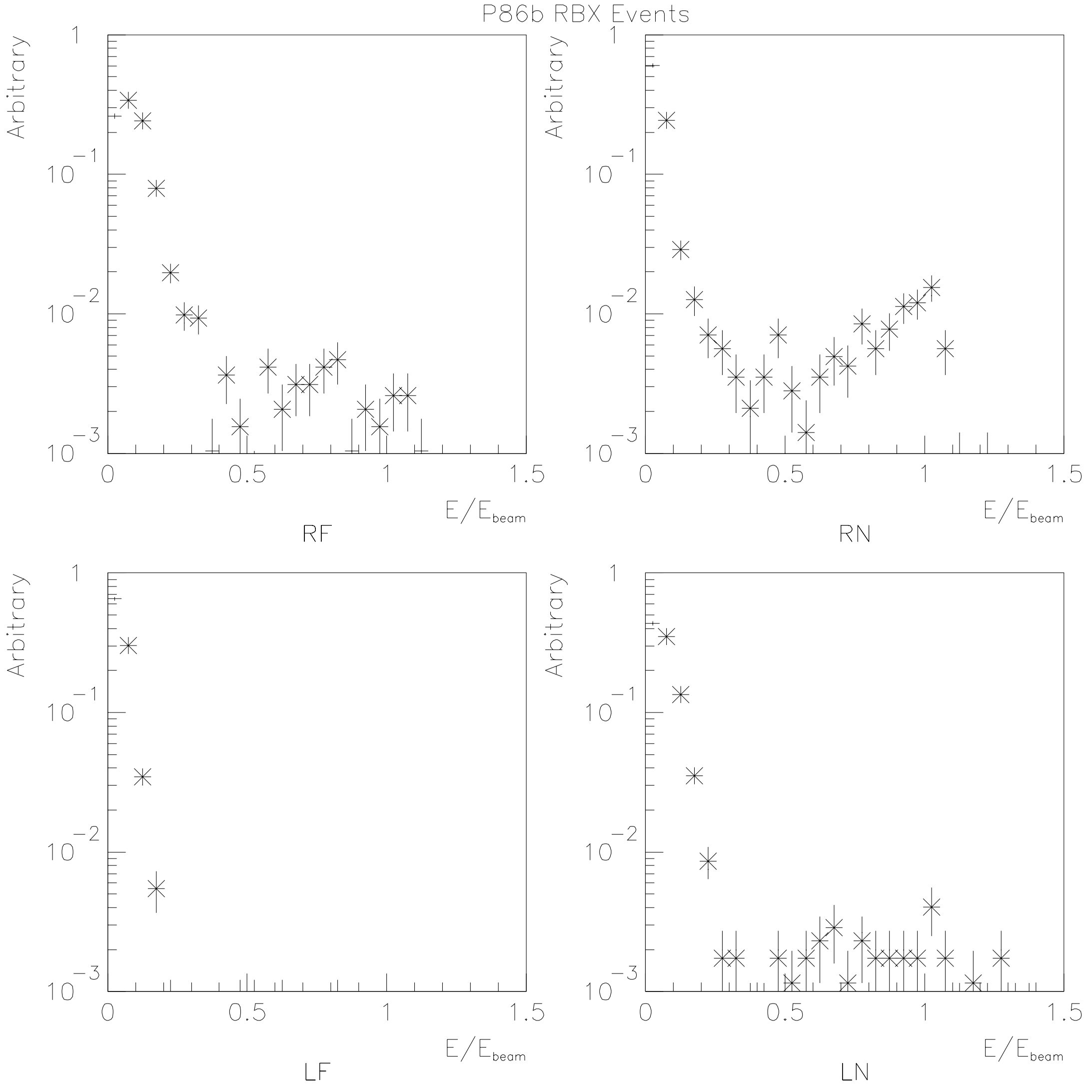

Fig. 4.16: The FFM energy distributions for random triggers during OPAL Period 86b show a decrease in the lower energy background for the Right FFM modules, which is consistent with an improving vacuum on the Left side of OPAL.

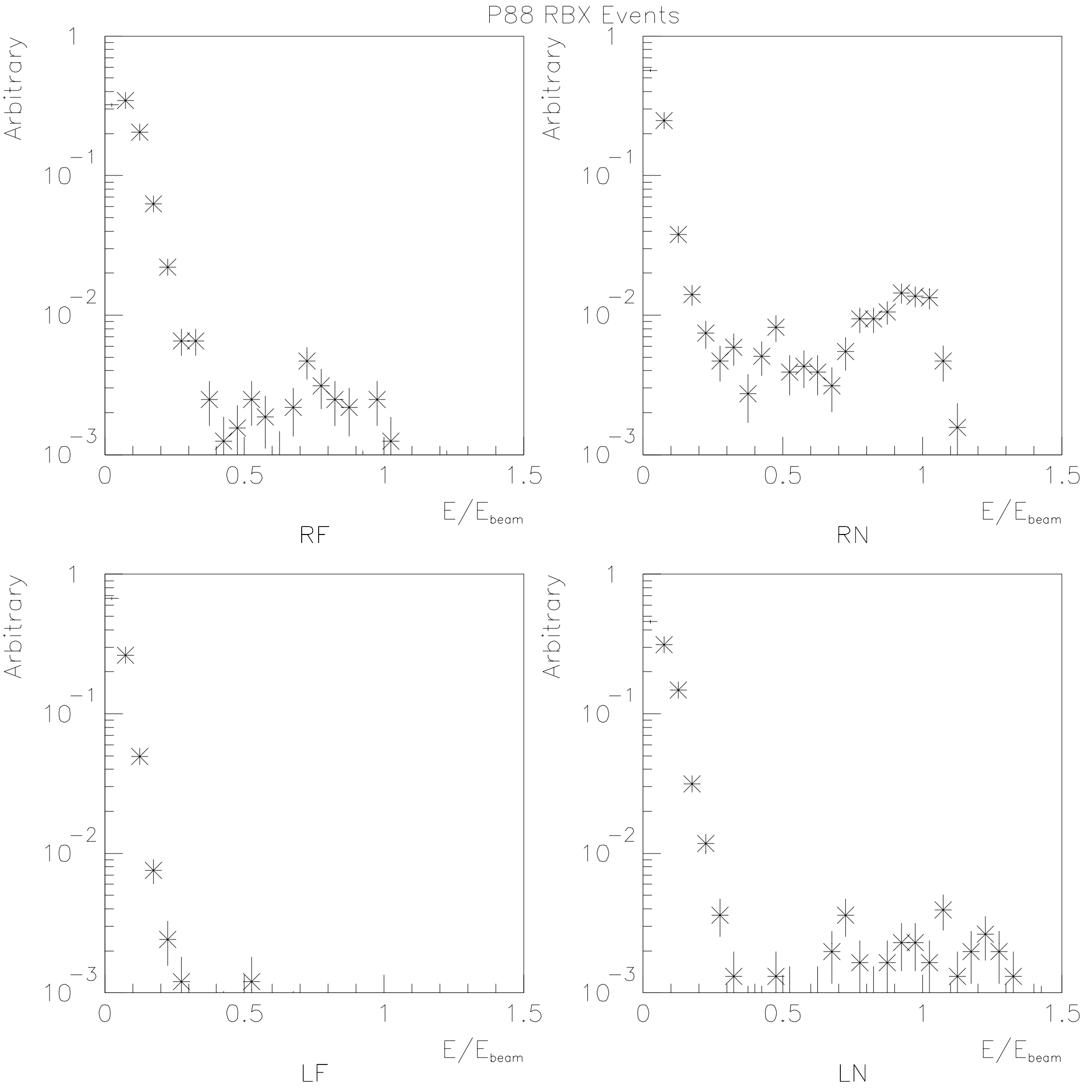

Fig. 4.17: The energy distribution for random triggers in Period 88 does not look strikingly different from that in Period 86b.

Figures 4.18 through 4.21. The reconstructed Bhabha energy distributions for each Period are shown, along with the Accidental energy spectrum for the modules where it is available. During all periods, the RN-LF calibration is successful. For Period 85, the Right Far energy calibration succeeds, but the Left Near fails. The contamination of the Bhabha sample for LN is about 20%. For Periods 86 through 88, the calibration for both Right Far and Left Near fails, and the estimated background for those modules is larger than the Bhabha signal.

The observations in this section indicate that a good knowledge of the LEP vacuum is important for detailed modelling of the off-momentum background. A higher vacuum in the arcs would reduce the machine background in the Far Forward Monitors. It remains to be seen if any improvement on this front can be made.

Another result of the background simulation, which will just be quoted here, is that there are collimators which may help to control the high energy peak from off-momentum background, but that the maximum reduction they allow is only about 50%.

4.9 Calibration Using Data

In order to calibrate the FFMs using data, the calibration constants as described in Section 4.6 are determined, then the positions of the detectors are estimated, using the measured cross section for Bhabha scattering into the detectors.

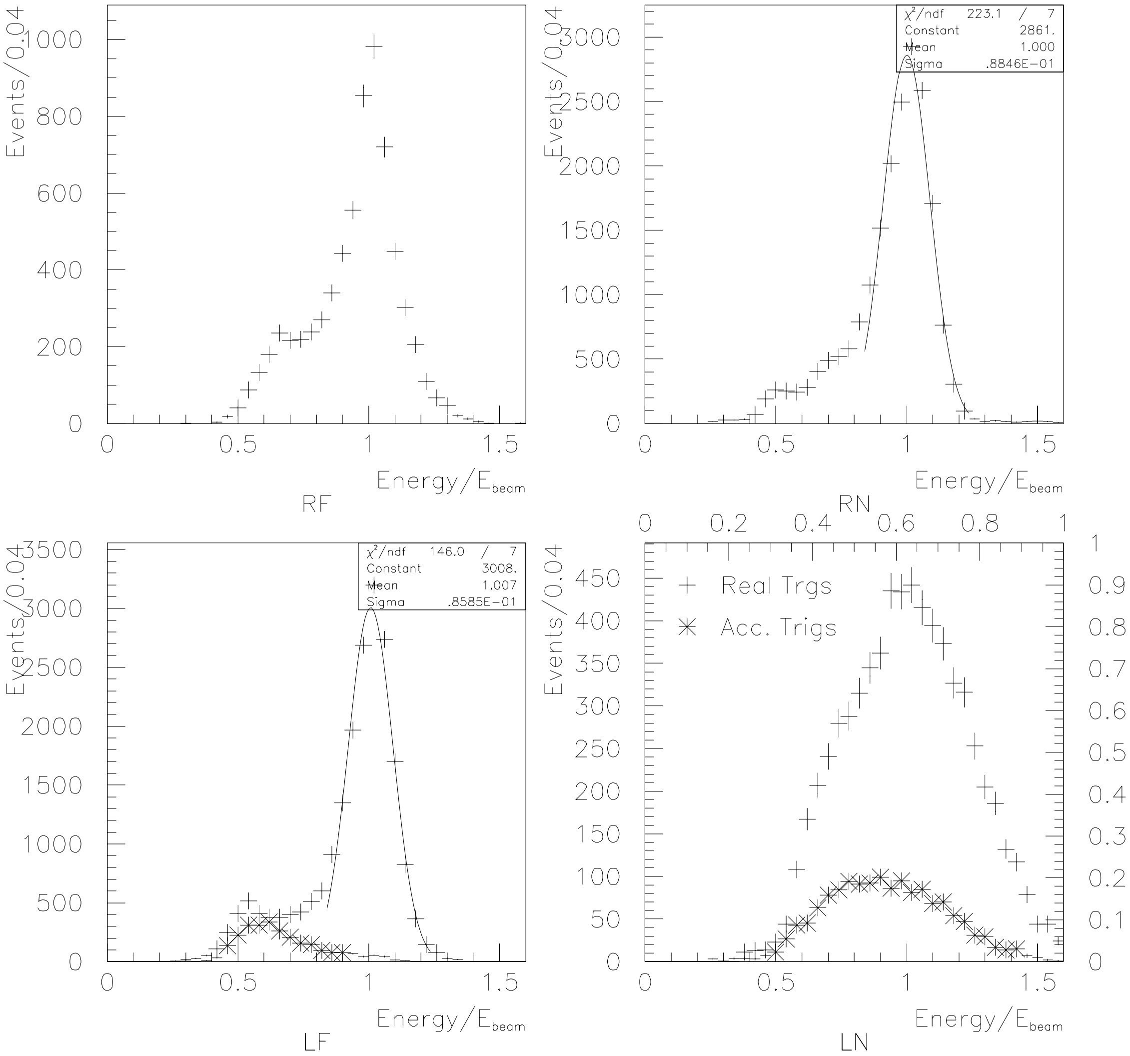

Fig. 4.18: Calibrated energy distributions for each module during Period 85. The crosses with error bars are for events triggered by the FDFAR trigger signal, while the asterisks with error bars are for events triggered by FDFARA. The Right Near and Left Far modules have well behaved calibrated peaks, and the FDFARA events account for the low energy tail. The Right Far module shows a peak at the beam energy similar to the RN and LF modules, but with a larger low energy tail. The calibration has failed for the Left Near module. As mentioned in Section 4.3 above, the pulse heights for the accidental triggers are only available for the Left Modules.

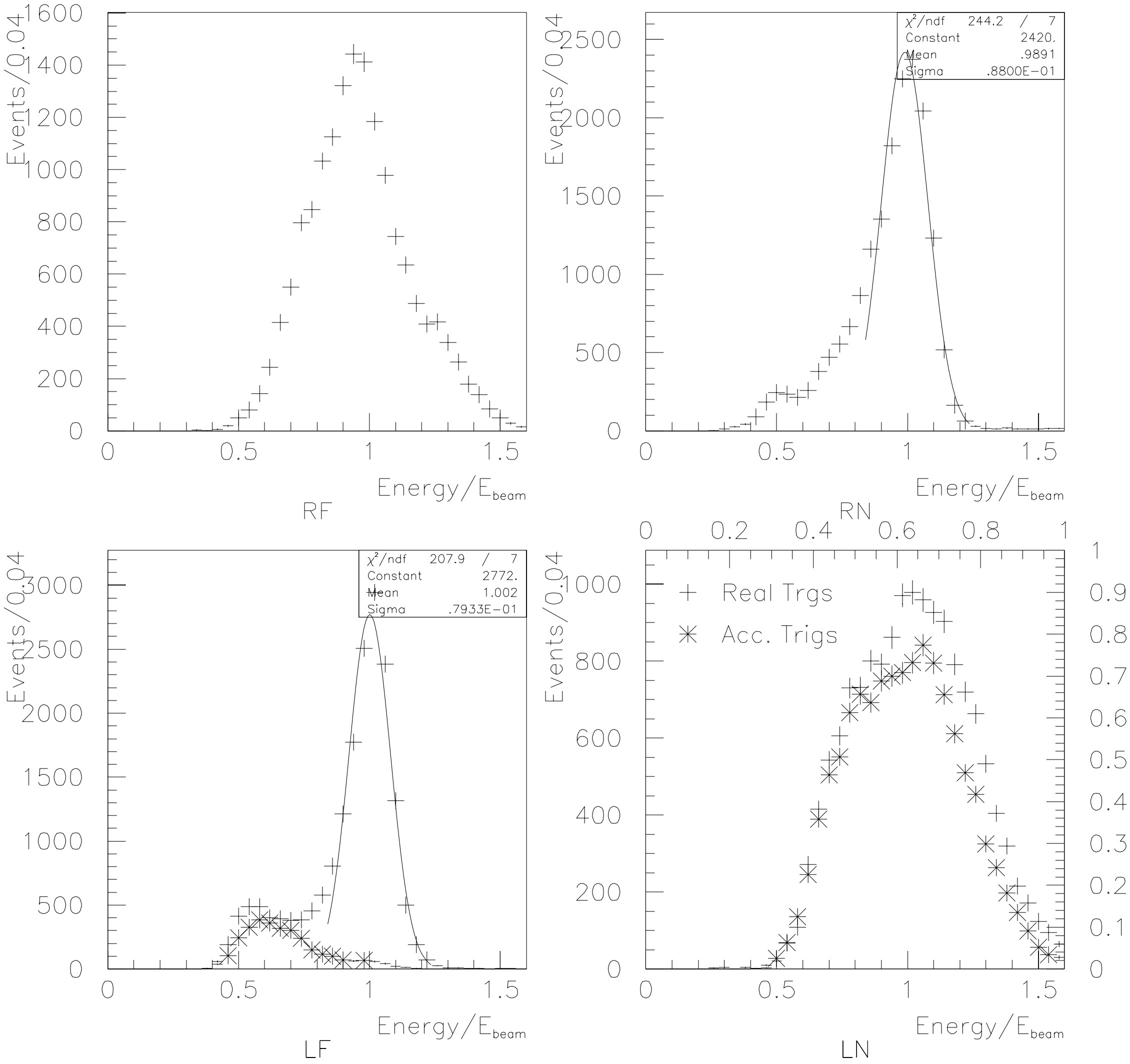

Fig. 4.19: Calibrated energy distributions for each module during Period 86a in the same format as in Figure 4.18. The calibrated energy peaks for the Right Near and Left Far modules are very similar to those in Period 85. The calibration has failed for both the Right Far and Left Near modules. The FDFARA background estimate for the Left Near module indicates that background dominates the calibration sample.

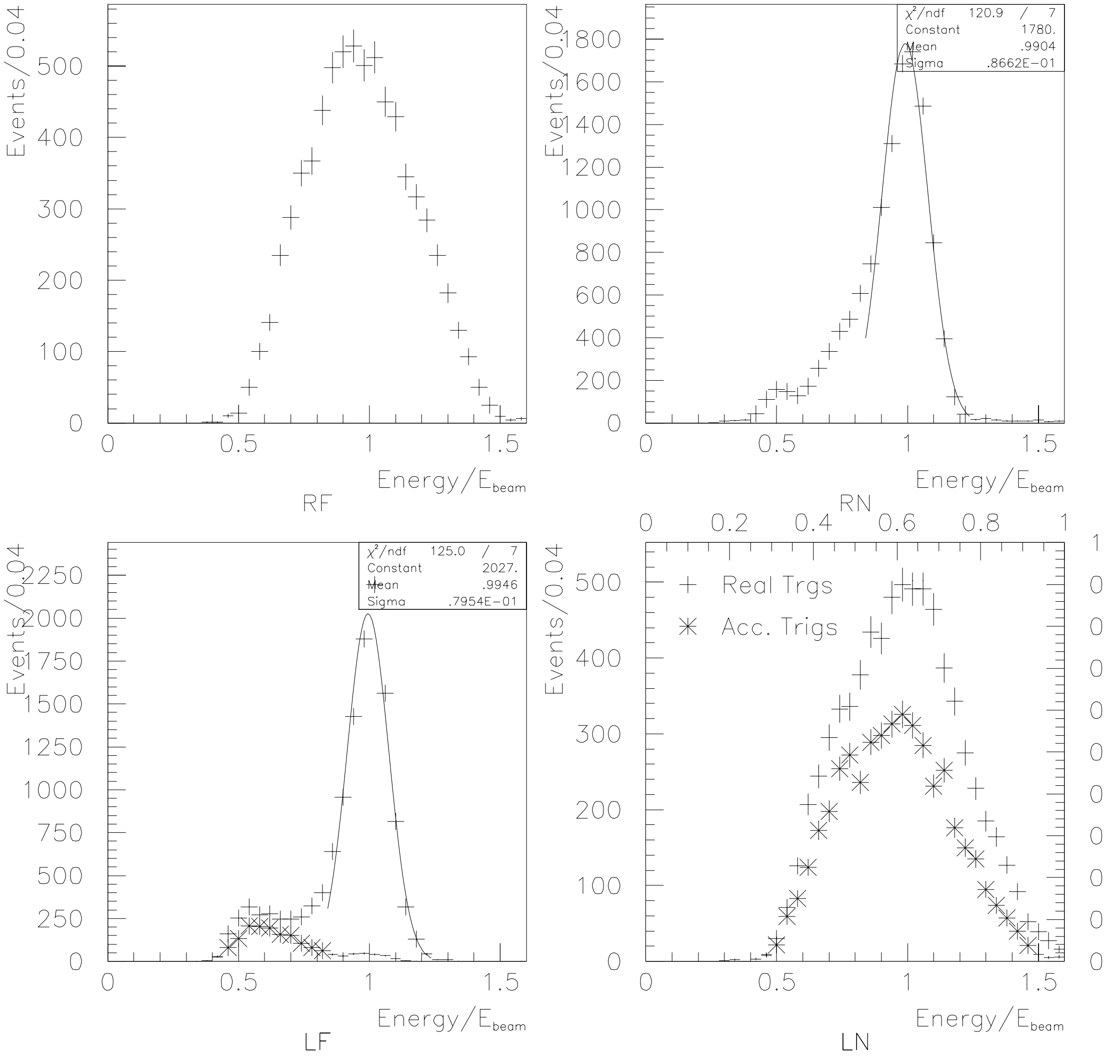

Fig. 4.20: Calibrated energy distributions for each module during Period 86b. The Right Near and Left Far modules are again well calibrated, while the calibration fails for the Right Far and Left Near modules. Note that the fraction of background in the RF-LN combination estimated by FDFARA is decreasing, although still dominant.

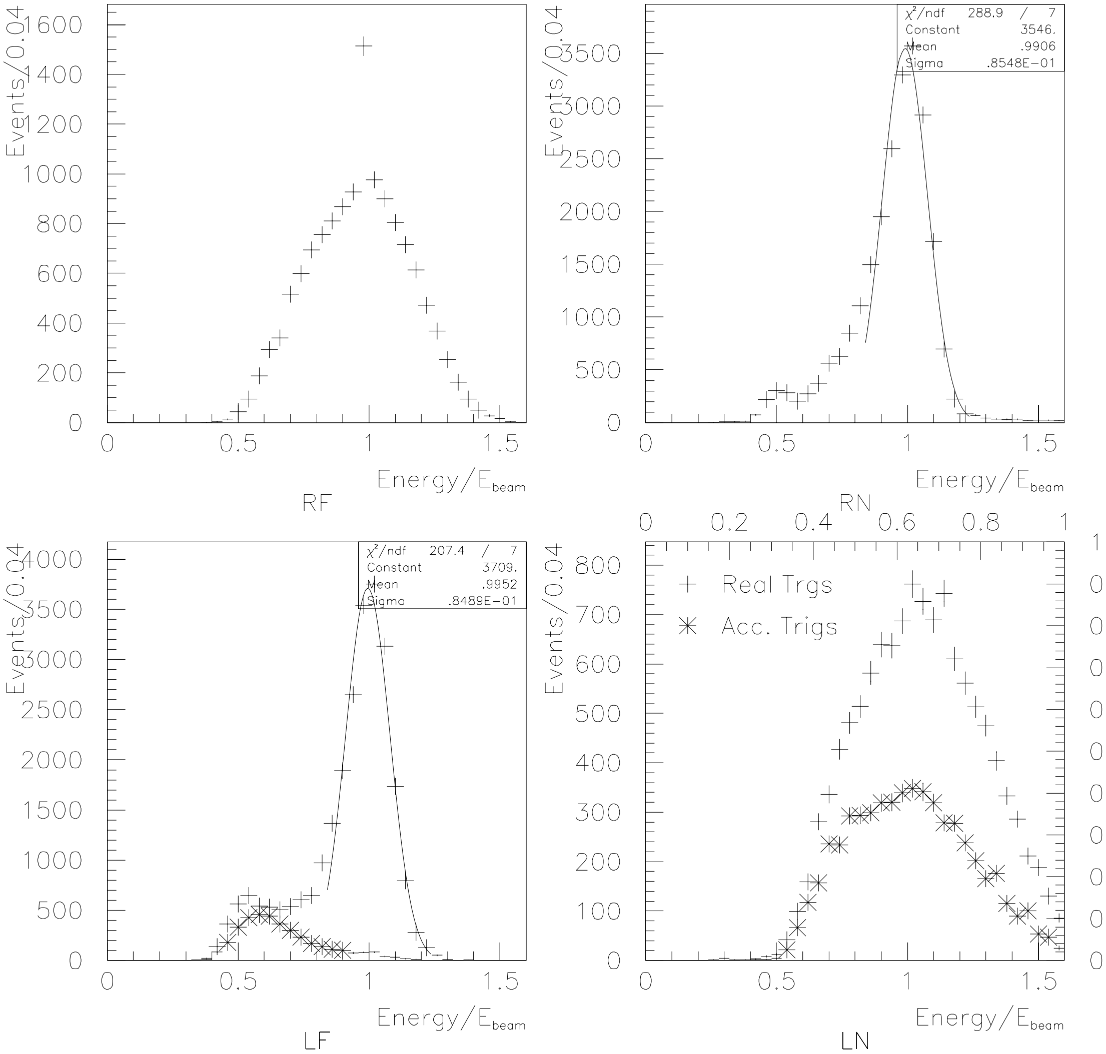

Fig. 4.21: Calibrated energy distributions for each module during Period 88. The Right Near and Left Far modules are again well calibrated, while the calibration fails for the Right Far and Left Near modules. The fraction of background in the RF-LN combination estimated by FDFARA has decreased further, but still not returned to the level of Period 85.

4.9.1 Stability of the Acceptance

Figure 4.22 shows the cross section (σ'_{FFM}) for Bhabha scattering into the FFMs after the calibration procedure has been used and Bhabha acceptance cuts applied. The acceptance cuts are $|\mathrm{Y}_{\mathrm{asym}}| < 0.9$ and $E > 0.8E^{\mathrm{Beam}}$. Figure 4.23 shows a histogram of σ'_{FFM}. The mean of the gaussian fitted to the peak is the value of σ'_{FFM} used for the detector position studies. The outlying runs have not yet been fully understood, but the width of the main body of the peak is consistent with the errors on individual runs.

4.9.2 Detector Position Estimation

The detector positions are estimated by varying some parameters of the detector simulation until the data and the simulation agree for σ'_{FFM} and for the asymmetry distributions defined in Equation 4.20 through Equation 4.22. The detector simulation has a large number of parameters which, for the sake of discussion, will be divided into several categories according to their function; internal GEANT physics parameters, mini-β quadrupole parameters, beam parameters, beam pipe parameters, FFM module position parameters, and FFM module crosstalk parameters.

The internal GEANT physics parameters control how the interaction of particles with matter is simulated. The defaults are taken for these parameters.

The parameters associated with the low-β quadrupoles are their positions, orientations, and transformation matrices. According to the LEP accelerator

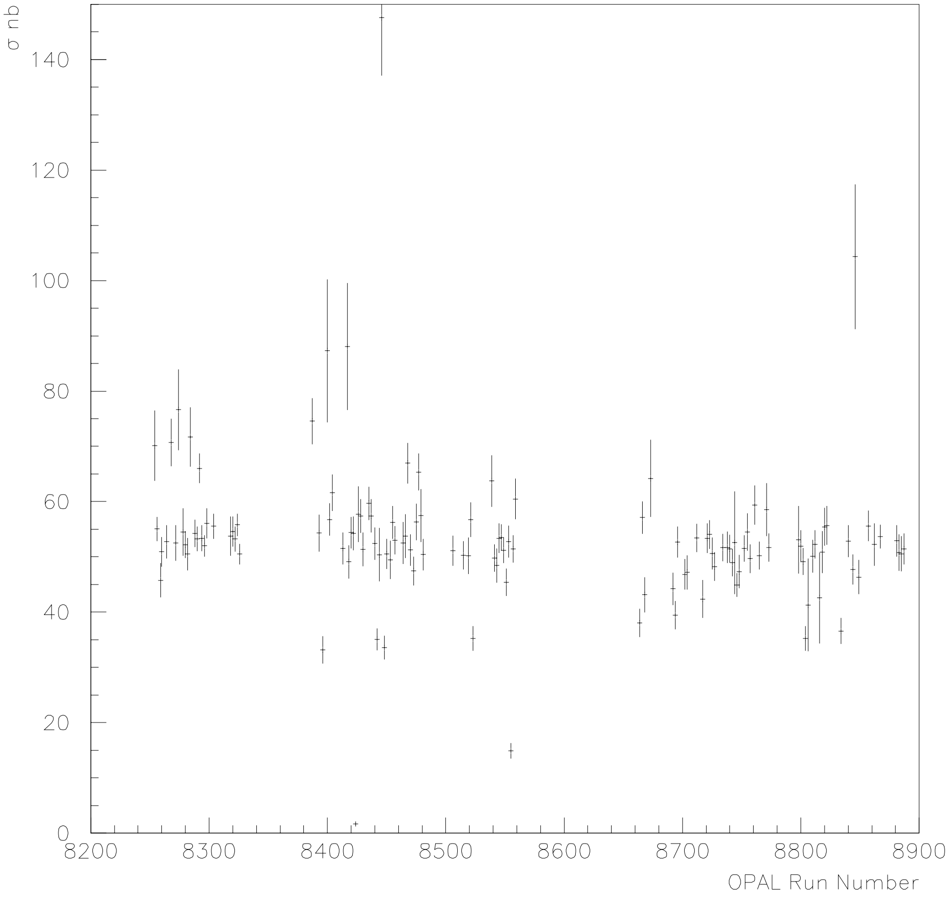

Fig. 4.22: The run to run stability of the acceptance is demonstrated by the constant value of the FFM Bhabha cross section (σ'_{FFM}). The origin of the outlying points has not yet been understood.

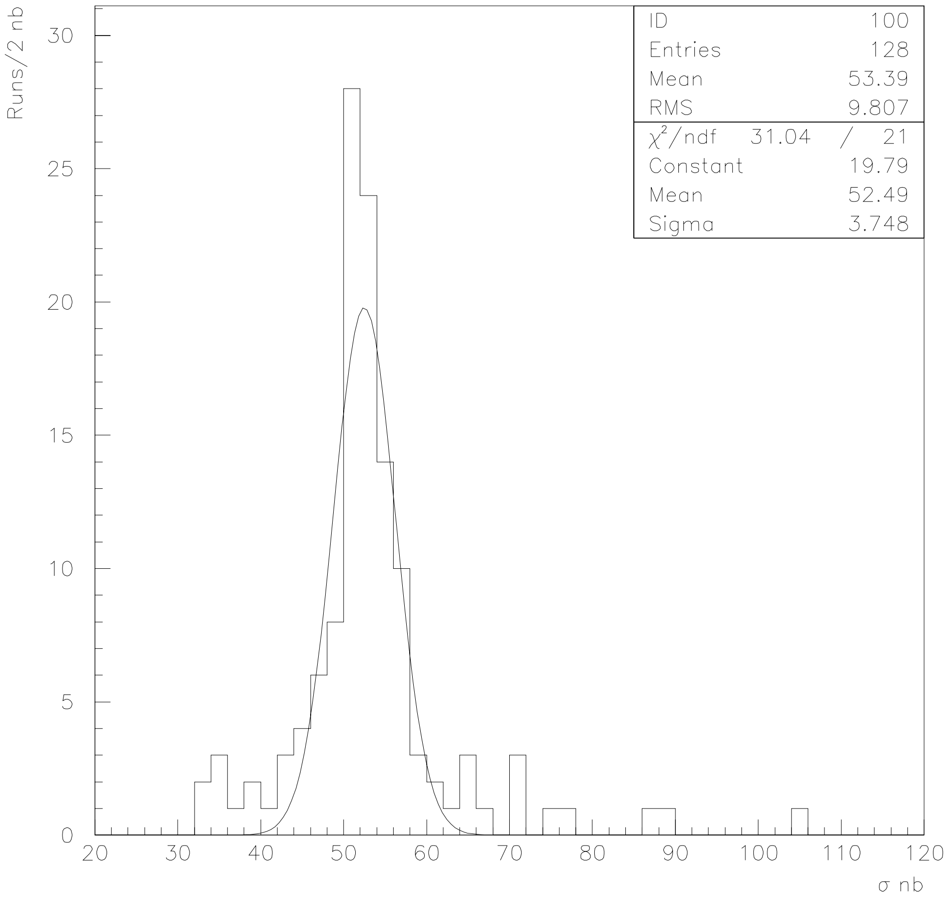

Fig. 4.23: The distribution of σ'_{FFM} for runs used in the doubly tagged analysis. The mean of the Gaussian fitted to the peak is taken to be σ'_{FFM}, for the purposes of determining the module positions.

group, the bore of these quadrupoles lies on the z axis and is aligned with an accuracy of ±0.2 mm. For the simulation, they are fixed to be on the z axis, with magnetic centers at a distance of ±4.88 m from the interaction point. The values in the transformation matrix given in Equation 4.13 should be accurate to better than 1%, and are also fixed at their nominal values.

The beam parameters describe the position of the interaction point and the angles at which the beams pass through the interaction point. The position of the interaction point in OPAL is measured using tracks from physics events and the LEP Beam Orbit Monitor system [29]. The average values for 1997 are $x \approx -0.3$ mm, $y \approx 1$ mm, and $z \approx 5$ mm. The tilts have been measured with the Silicon Tungsten Luminometers, and are consistent with zero, within the accuracy of the survey of the Silicon Tungsten Luminometers [30]. Given that there are uncertaities in the position of the FFM modules which are much larger than the uncertainties in the beam parameters, the beam spot position is taken to be at the origin, and the beams are taken to be colinear with the z axis.

The beam pipe parameters are the position and orientation of the section of beam pipe that is included in the GEANT simulation. In addition, the outermost radius at which particles are propagated to the FFMs (78 mm) is set by the inner radius of the cylindrical section of beam pipe in front of the FFMs, shown in Figure 4.1. According to the machine group, the beam pipe was aligned to be colinear with the z axis to an accuracy of ±2 mm. In the simulation, the beam pipe is assumed to be parallel to the z axis, and centered at y=0. The displacement in the x direction is varied in order to best match the data and Monte Carlo.

The FFM position parameters are the displacements and orientations of each of the FFM modules. Only the parameters for the Right Near and Left Far modules are of interest, because only these modules are used for the doubly tagged analysis. During installation in 1997, the modules were aligned by eye to be parallel to the beam pipe. This alignment is assumed to be accurate to several degrees, so for the Monte Carlo studies, the orientation parameters are fixed so that the scintillator planes are perpendicular to the z axis and the inner face of the detector is parallel to the z axis. The displacement in z from the interaction point is known with a precision of approximately one centimeter, and is fixed at its measured value. The displacement parameters in x and y for the RN and LF modules are allowed to vary in order to find the best match between data and Monte Carlo.

The final category of parameters is the set of individual module crosstalk parameters. The crosstalk for each module is parametrized by two 2 by 2 matrices. Each matrix relates the measured signal for adjacent inner and outer compartments, according to Equation 4.32. The constants a and b in Equation 4.32 are chosen so that the $\mathrm{X_{asym}}$ distributions in data and Monte Carlo match. For electronic cross talk, the amount of cross talk should be symmetric between the two compartments. Asymmetric cross talk can be caused by a misalignment of the light guides, so that one light guide sees part of the light from the adjacent compartment. Such a misalignment was observed in one module during the 1997-1998 upgrade, and may have been present in others. The best values for the cross talk parameters in 1997 are shown in Table 4.7.

$$\begin{pmatrix} n'_{\mathrm{outer}} \\ n'_{\mathrm{inner}} \end{pmatrix} = \begin{pmatrix} 1-b & a \\ b & 1-a \end{pmatrix} \begin{pmatrix} n_{\mathrm{outer}} \\ n_{\mathrm{inner}} \end{pmatrix} \tag{4.32}$$

To summarize the above discussion, the parameters which are varied in order to match the Monte Carlo simulation and the data are:

- The x displacement of the beam pipe at each end of OPAL (2 parameters).
- The displacements in x and y of the Right Near and Left Far FFM modules (4 parameters).
- The cross talk parameters for the RN and LF modules (8 parameters).

which gives a total of 14 free parameters.

The best estimates for the free parameters were found in the following way:

- An x position for the modules was chosen.
- The beam pipe position was varied until σ'_{FFM} agreed with the data.
- The cross talk parameters were varied until the peak of the $\mathrm{X_{asym}}$ distribution was at the same position in data and Monte Carlo, and the $\mathrm{X_{asym}}$ -$\mathrm{Y_{asym}}$ correlations shown in Figure 4.28 approximately agreed between data and Monte Carlo.
- If the tail of the $\mathrm{X_{asym}}$ distribution in Monte Carlo did not agree with the tail in data the process was repeated, choosing a new x position based

on whether the Monte Carlo tail was longer or shorter than the data one.

- The y positions of the modules were varied until the $\mathrm{Y}_{\mathrm{asym}}$ distributions in data and Monte Carlo showed reasonable agreement.

The process described above was time consuming and not guaranteed to converge on the correct values of the parameters in a finite amount of time. The best estimate of the parameters is thus not expected to produce perfect agreement between Monte Carlo and data. Fundamental problems include the large number of free parameters, the presence of significant backgrounds in even the best samples, and the simplifying assumption that all modules behave in the same way. (As part of the 1997-1998 upgrade, and driven by this analysis, new PMT bases were made to further reduce electronic cross-talk and survey information was obtained to determine the detector positions. These changes will reduce the number of free parameters, or at least limit them to a small range of allowed variations.)

In order to understand the effect of varying the free parameters, the distributions of the asymmetries and energy for Monte Carlo and data are shown in Figures described below for the best values of the parameters, with relevant distributions for variations of each parameter or set of parameters. The value of σ'_{FFM} from the Monte Carlo is shown for each variation in Table 4.5.

The distributions of the asymmetries and energy for Monte Carlo and data are shown in Figures 4.24, 4.25, 4.26 and 4.9. The general shapes of the distributions agree, but there are discrepancies which indicate that the

Variation	σ'_{FFM} nb
nominal	51.98 ± 2.30
$x_{\mathrm{nom}} - 2$ mm	68.75 ± 2.63
$x_{\mathrm{nom}} + 2$ mm	42.16 ± 2.06
$y_{\mathrm{RN}} = 0$, $y_{\mathrm{LF}} = 0$ mm	54.60 ± 2.35
$y_{\mathrm{RN}} = 2$ mm, $y_{\mathrm{LF}} = 0$ mm	51.05 ± 2.27
$y_{\mathrm{RN}} = 4$ mm, $y_{\mathrm{LF}} = 0$ mm	46.64 ± 2.17
$x_{\mathrm{pipe}} - 2$ mm	56.39 ± 2.39
$x_{\mathrm{pipe}} + 2$ mm	42.15 ± 2.06

Tab. 4.5: How σ'_{FFM} varies with FF module parameters. For the x position variations, the positions of both modules were varied together. For the y position variations, both modules were taken to be at y = 0, and then one module's position was varied. The variable x_{pipe} is the x position of the center of the beam pipe, and this parameter was varied simultaneously for both ends of OPAL.

Monte Carlo model with these values of the parameters does not completely describe the data. In Figure 4.24 the data peak at negative $\mathrm{X}_{\mathrm{asym}}$ is lower than the Monte Carlo peak and the tail at positive $\mathrm{X}_{\mathrm{asym}}$ does not match for the Right Near module. In Figure 4.25, both edges of the Right Near $\mathrm{Y}_{\mathrm{asym}}$ distribution disagree, while the right edge of the Left Far $\mathrm{Y}_{\mathrm{asym}}$ data distribution falls below the Monte Carlo distribution. In Figure 4.26, the shapes of the $\mathrm{Z}_{\mathrm{asym}}$ distributions for both the Right Near and Left Far modules are in reasonable agreement between Monte Carlo and data, but the means are shifted. In all cases, the discrepancies might be removed by altering the position and orientation of the modules in the detector simulation. As described earlier, improving the agreement between Monte Carlo and data is prohibitively time consuming with the large number of free parameters which can be tuned.

No reliable measurements of the FFM module positions are available for 1997 and the asymmetry distributions indicate that the best determined values of the parameters do not exactly match the actual values of the parameters for the data. The best determined values are, however, plausible; they do not require conditions which are excluded by the construction of the cantilever in which the modules and the beam pipe are located. In order to evaluate the systematic errors of the positions of the modules and beam pipe, it is assumed that the best estimated values are near the true ones. The scale of allowed variation in the parameters is somewhat arbitrary, since no obvious resolution parameter is available, and in any case the best estimated parameters are not necessarily the true ones. For this reason, it is useful to construct a figure of merit which characterizes how well the data agrees with the Monte Carlo simulation, for a given set of parameters. The figure of merit is constructed as a combined χ^2 between the values of σ'_{FFM} from data and that predicted by Monte Carlo and from the data and Monte Carlo asymmetry histograms, using

$$\chi^2 = \sum_{1}^{n} \frac{(H_i^D - H_i^M)^2}{(\sigma_i^D)^2 + (\sigma_i^M)^2} \tag{4.33}$$

where n is the number of bins in each histogram, H_i is the height of the i^{th} bin, σ_i is the error on the i^{th} bin, and the superscripts D and M stand for data and Monte Carlo, respectively. The figure of merit is defined as

$$F_{Merit} = \frac{1}{3}\left(\frac{\chi^2_{RN}}{n} + \frac{\chi^2_{LF}}{n} + \chi^2_{\sigma'_{\mathrm{FFM}}}\right). \tag{4.34}$$

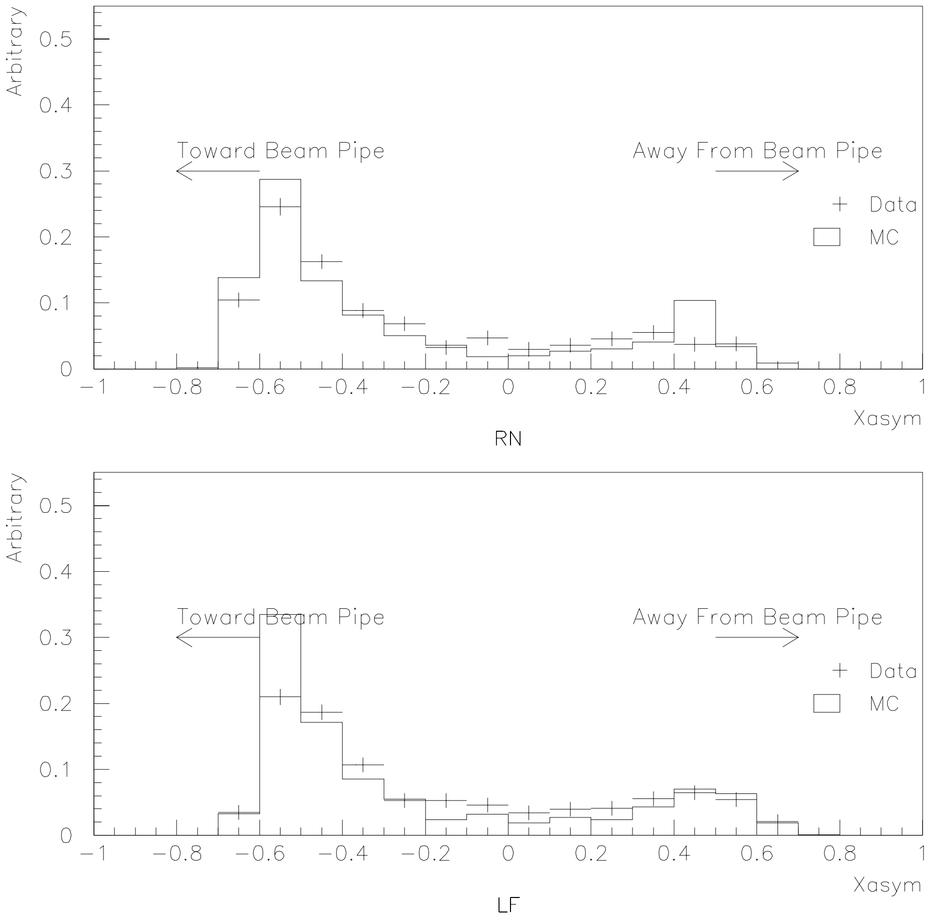

Fig. 4.24: Distribution of X_{asym} for the RN and LF modules, for data and Monte Carlo. The Monte Carlo distributions were made using the best estimate for the free parameters. Each distribution is normalized to have an area of 1, so that the shapes can be compared. This distribution is related to the distribution of Bhabha electrons in x.

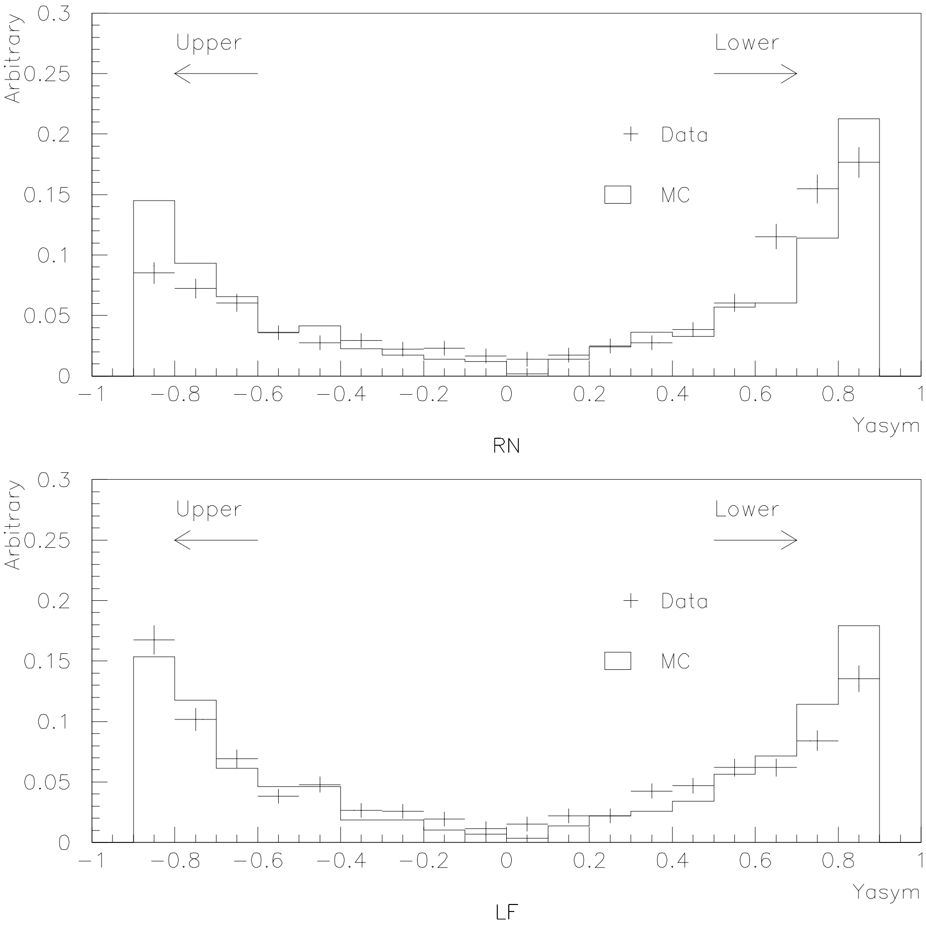

Fig. 4.25: Distribution of Y_{asym} for the RN and LF modules, for data and Monte Carlo. The Monte Carlo distributions were made using the best estimate for the free parameters. Each distribution is normalized to have an area of 1, so that the shapes can be compared. This distribution is related to the distribution of Bhabha electrons in y.

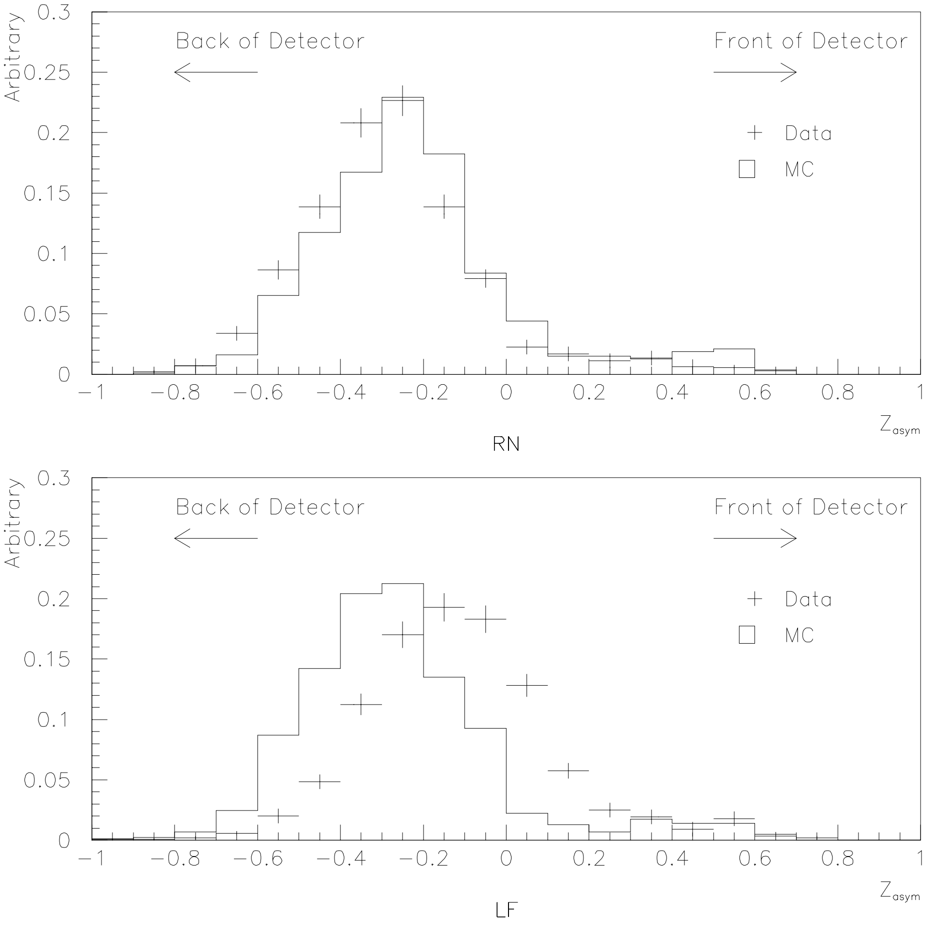

Fig. 4.26: Distribution of $\mathrm{Z_{asym}}$ for the RN and LF modules, for data and Monte Carlo. The Monte Carlo distributions were made using the best estimate for the free parameters. Each distribution is normalized to have an area of 1, so that the shapes can be compared. This distribution is related to the shower profile in depth in the detector. The shift of the peak for the LF distribution in data could be due to extra material in front of the detector.

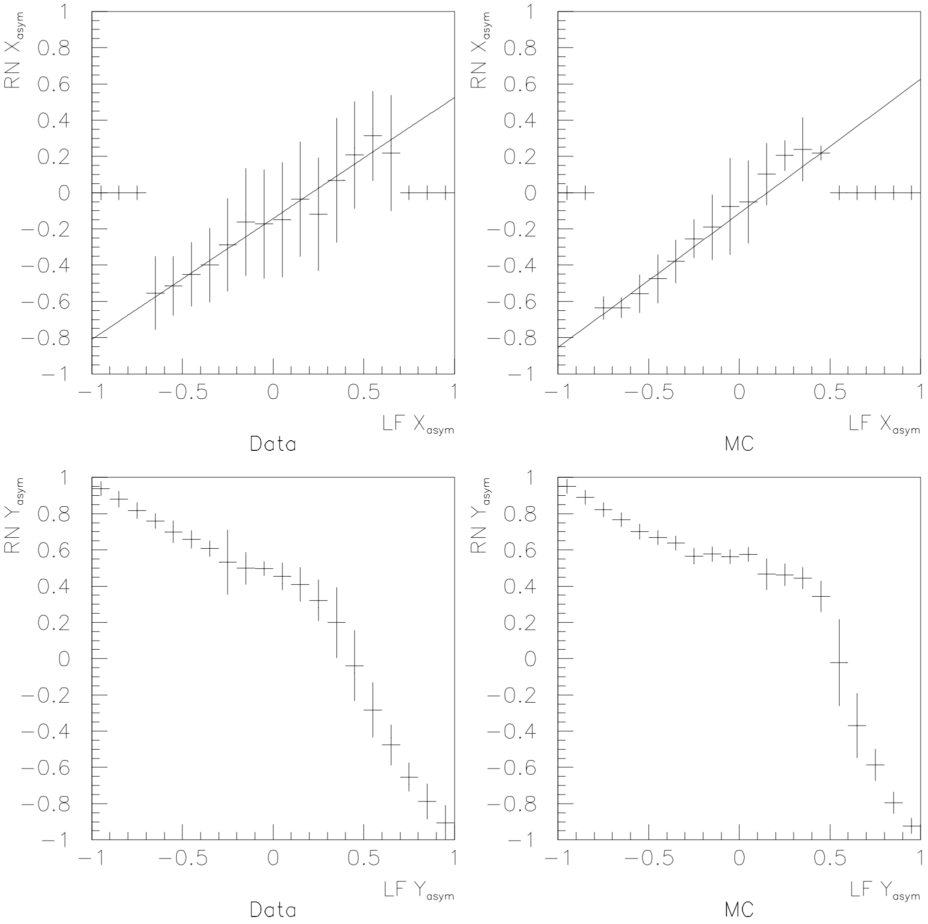

Fig. 4.27: Correlations between asymmetries in the RN and LF modules, for Bhabha events in Monte Carlo and data. The agreement between Monte Carlo and data is reasonably good, although the knee in the Y_{asym} distribution is exaggerated for the Monte Carlo. This knee is due to misalignment in y. The point at which the line of correlation crosses zero for the X_{asym} correlation is used to determine the misalignment of the modules in x, as discussed in the text. The bins where X_{asym} is zero on either end of the X_{asym} distributions contain no events.

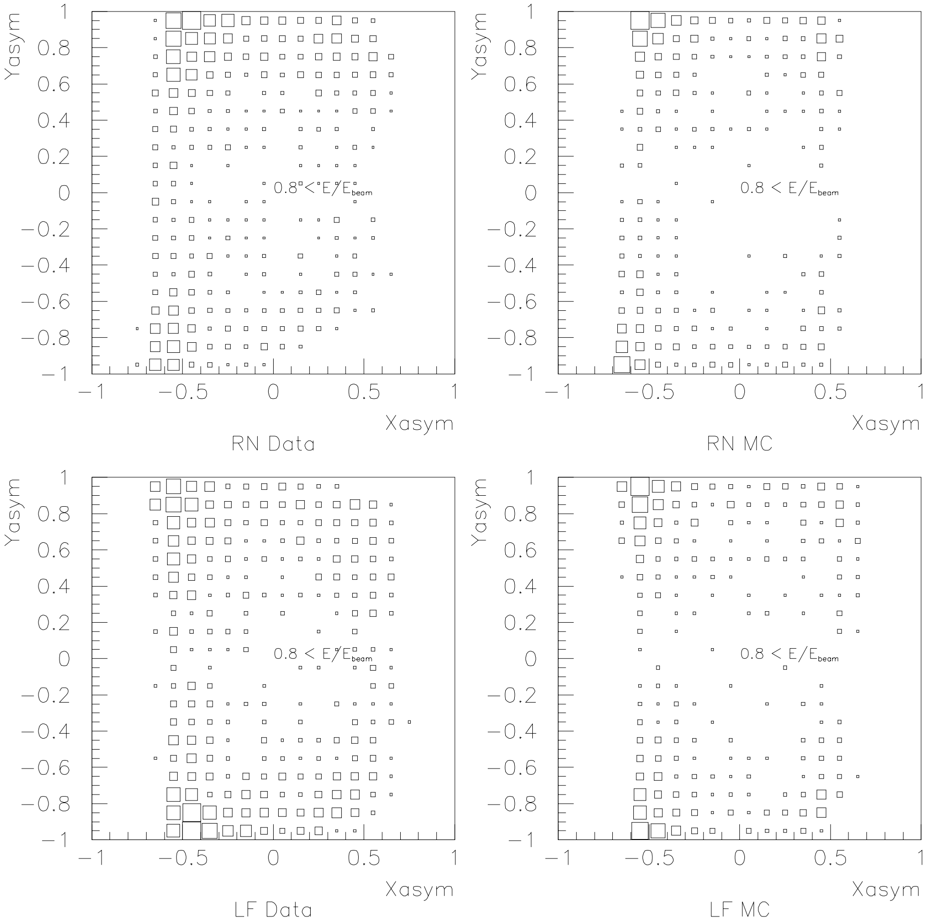

Fig. 4.28: Correlation between X_{asym} and Y_{asym} , for Monte Carlo and data, using the best estimated parameters for the Monte Carlo. These data distributions were used to tune the Monte Carlo cross-talk parameters, as described in the text.

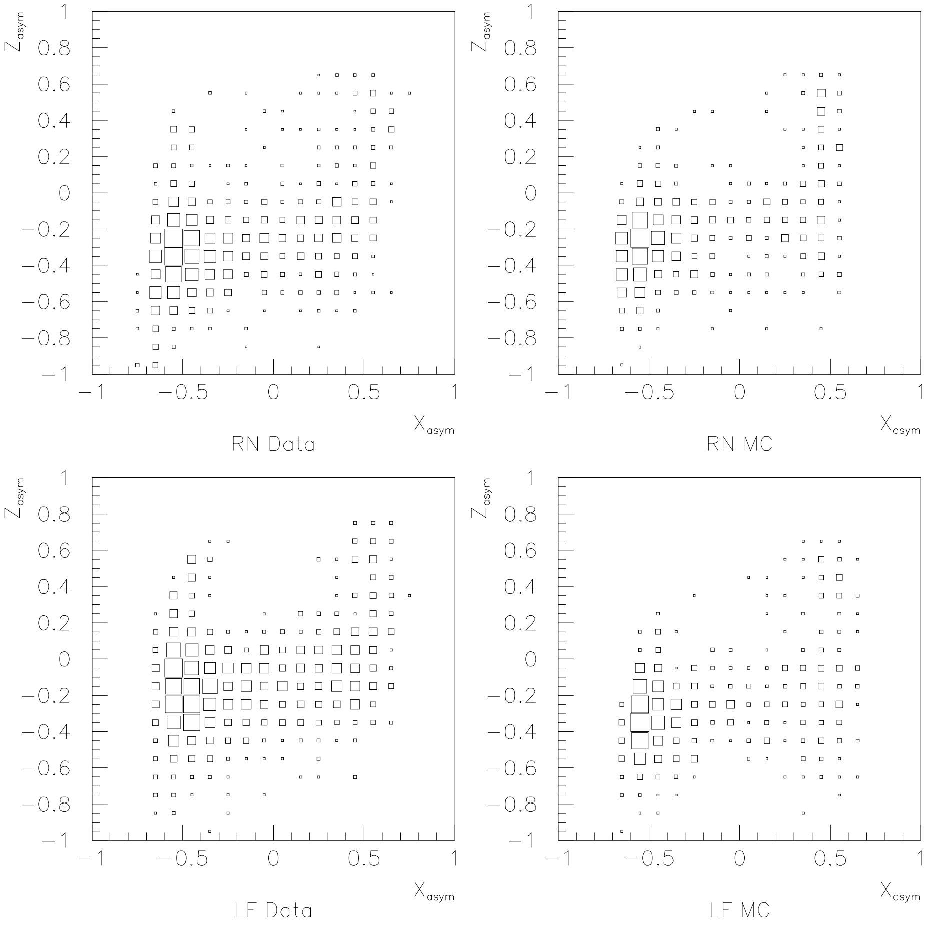

Fig. 4.29: Correlation between X_{asym} and Z_{asym} , for Monte Carlo and data, using the best estimated parameters for the Monte Carlo.

The variations are chosen so that they produce visible changes in the figure of merit, as shown in Table 4.8. These variations give a feeling for what effect changing the module positions has on the final result. (The 1997-1998 upgrade provides survey information for the detectors and also a more precise x position measurement which can be used to cleanly determine the distance from the inner to the outer edge of the acceptance from data. The procedure used here will therefore be replaced by a more precise one which has built in cross checks.)

Figure 4.30 shows the $\mathrm{X_{asym}}$ distributions for 2 mm variations in the x position of the modules. These variations change the shape of the tail of the $\mathrm{X_{asym}}$ distribution, and also result in large changes in σ'_{FFM}, as shown in Table 4.5. Because the 2 mm changes result in significant changes in the accepted cross section, a conservative error of 3 mm is taken for the x positions; this should cover any possible uncertainty in the x position.

Figure 4.31 shows changes in the $\mathrm{Y_{asym}}$ distributions for 2 mm variations from y=0 in the y position of one module. This variation was chosen to illustrate the effect of misalignment as well as to estimate the systematic error. From Figure 4.31 and from Table 4.5, it is seen that variations in the y position do not effect the measured distributions as much as those in the x position. These variations result in an imbalance between the positive and negative sides of the $\mathrm{Y_{asym}}$ distributions. As an estimate, the error on the y position of each module will be taken as 5 mm, which again should cover any possible uncertainty in the y position.

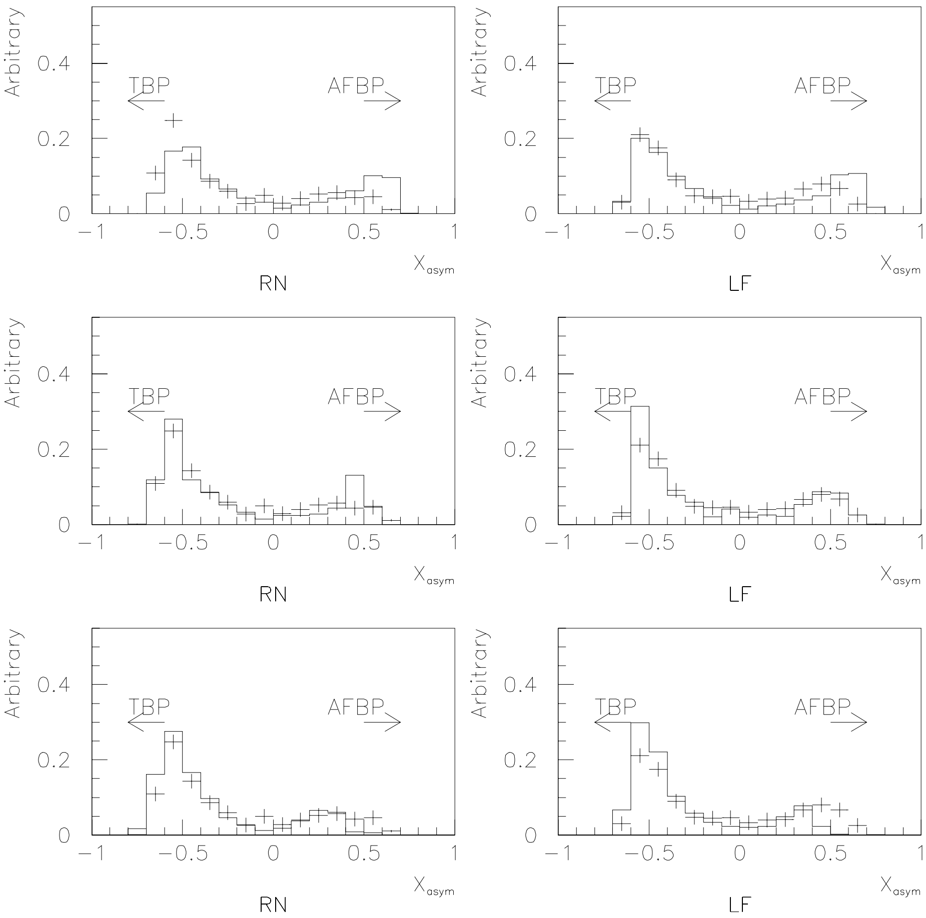

Fig. 4.30: Pairs of X_{asym} distributions for variations in the x position of the modules. The top pair shows the effects of a variation of 2 mm towards the beam pipe for both modules. The center pair shows the X_{asym} distributions for both modules at their best estimated positions. The bottom pair shows the effects of a variation of 2 mm away from the beam pipe for both modules. The abbreviations TBP and AFBP in the plots indicate, respectively, towards the beam pipe and away from the beam pipe.

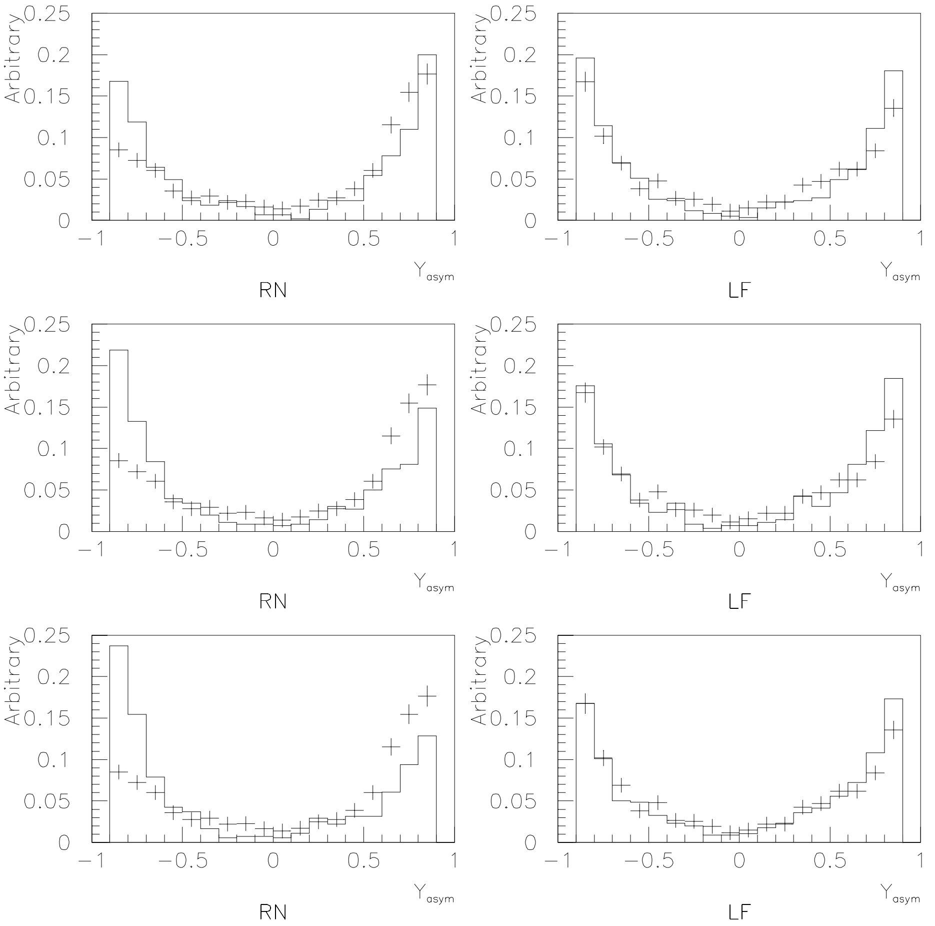

Fig. 4.31: Pairs of $\mathrm{Y}_{\mathrm{asym}}$ distributions for variations in the x position of the modules. The top pair shows the result with both modules at y = 0. The center pair shows the $\mathrm{Y}_{\mathrm{asym}}$ distributions for one module at y = 0 and the other at y = 2 mm. The bottom pair shows the results for one module at y = 0 and the other at y = 4 mm.

Figure 4.33 shows the $X_{\rm asym}$ distributions for 2 mm variations in the x position of the beam pipe. The systematic error in the x position of the beam pipe is not estimated from these variations, however. There are two degrees of freedom in x for each module, the x position of the detector and the x position of the beam pipe. The former determines the inner edge of the acceptance, while the latter determines the outer edge of the acceptance by shadowing the outer part of the detector. These two degrees of freedom can be reduced to one by requiring that $\sigma'_{\rm FFM}$ assumes a particular value, since the value of $\sigma'_{\rm FFM}$ is determined by the positions of the inner and outer edges of the acceptance. This requirement assumes that the conjugate FFM modules are perfectly aligned, so that all of the clear acceptance of each module contributes to $\sigma'_{\rm FFM}$. The effect of misalignment is shown schematically in Figure 4.32. The bending of the quadrupoles is represented by the discontinuity in the lines representing the edges of the acceptance. The solid boxes show perfectly aligned FFM modules, while the dotted box shows a misaligned module. If a module is misaligned, then $\sigma'_{\rm FFM}$ is smaller than it would be for perfect alignment. To take this into account, a systematic error on the position of the beam pipe is assigned, so that the clear acceptance of a single module can be larger than is estimated using $\sigma'_{\rm FFM}$.

Figure 4.27 shows the correlation between the $X_{\rm asym}$ values for the RN and LF modules. If the modules were perfectly aligned, the correlation line would pass through the origin. This is not the case, however, and the correlation line passes approximately through -0.2, 0.0. Using Figure 4.11, this translates

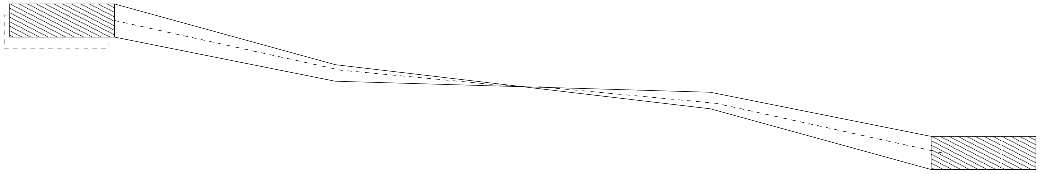

Fig. 4.32: The effect of module misalignment is to reduce σ'_{FFM}. In the case of perfect alignment, the inner and outer edges of the acceptance of both modules are the same. With misalignment, they are different, and one module determines the outer edge of the Bhabha acceptance (as shown by the dashed lines), while the other determines the inner edge.

Parameter	Best Estimated Value
x_{RN}	59 ± 3 mm
y_{RN}	-3 ± 5 mm
$x_{\mathrm{RN}}^{\mathrm{Beam\ Pipe}}$	7.5 ± 2 mm
x_{LF}	59 ± 3 mm
y_{LF}	0 ± 5 mm
$x_{\mathrm{LF}}^{\mathrm{Beam\ Pipe}}$	7.5 ± 2 mm

Tab. 4.6: The results of the position determination using data are shown. These values will be used in the determination of the acceptance correction for the doubly tagged analysis presented in Chapter 5.

to a misalignment of about 2 mm. An error of 3 mm will therefore be taken for the x position of the beam pipe, in order to take this misalignment into account in the systematic error.

The final results of the position determination are given in Table 4.6 and Table 4.7. These positions will be used in calculating the acceptance correction in Chapter 5.

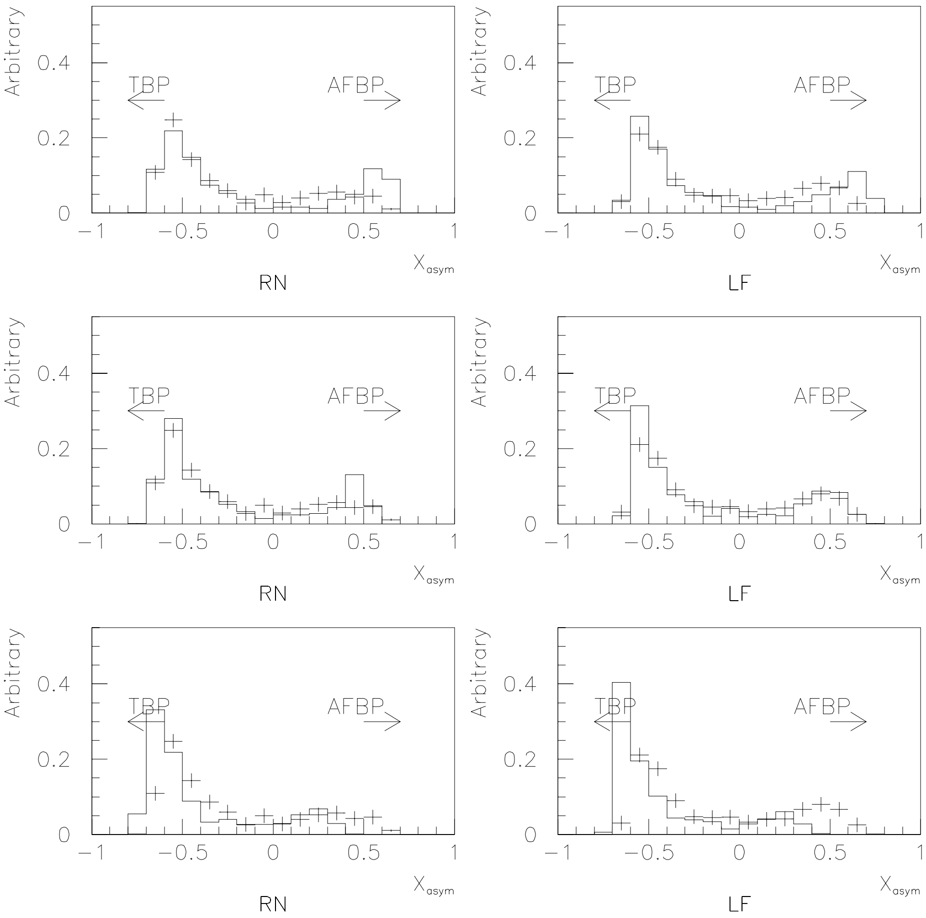

Fig. 4.33: Pairs of $\mathrm{X_{asym}}$ distributions for various displacements of the beam pipe in x. The top pair is for the beam pipe displaced from the best estimated position by 2 mm at each end of OPAL. The center pair shows $\mathrm{X_{asym}}$ for the beam pipe at the best estimated position. The bottom pair is for the beam pipe displaced by -2 mm at each end of OPAL.

Parameter	Best Estimated Value
$a_{\rm RN}^{\rm upper}$	0.23
$b_{\rm RN}^{\rm upper}$	0.04
$a_{\rm RN}^{\rm lower}$	0.08
$b_{\rm RN}^{\rm lower}$	0.07
$a_{\rm LF}^{\rm upper}$	0.05
$b_{\rm LF}^{\rm upper}$	0.02
$a_{\rm LF}^{\rm lower}$	0.26
$b_{\rm LF}^{\rm lower}$	0.05

Tab. 4.7: The best estimated values of the cross talk parameters.

Variation	RN χ^2	LF χ^2	$\sigma'_{\rm FFM}\chi^2$	FOM
BestEstimate	9.91	13.62	0.37	7.97
$x_{\rm ffm} - 3$ mm	7.66	15.78	54.07	25.83
$x_{\rm ffm} + 3$ mm	42.29	35.03	156.11	77.81
$x_{\rm pipe} + 2$ mm	16.95	15.71	8.81	13.82
$x_{\rm pipe} - 2$ mm	9.77	14.65	3.38	9.27
$y_{\rm ffm} - 5$ mm	12.20	12.01	70.19	31.47
$y_{\rm ffm} + 5$ mm	10.26	13.90	0.05	8.07

Tab. 4.8: The χ^2 per degree of freedom between data and Monte Carlo for RN asymmetries, LF asymmetries, and $\sigma'_{\rm FFM}$. The figure of merit (FOM) is the average of the three χ^2.

5. TARGET VIRTUALITY EFFECTS IN $\gamma\gamma^*$ SCATTERING

5.1 Outline of the Measurement

During data taking in 1997, a small sample of two photon events with a tag in the Silicon-Tungsten Luminometer or Forward Detector and another tag in one of the Far Forward monitors was collected by OPAL. With these events, I have performed a prototype analysis of the measurement of the cross section for DIS scattering of an electron from a virtual photon target. A result on the P^2 suppression of the hadronic content of the photon was obtained, but the statistical error was too large to allow discrimination among the available models. This analysis demonstrates the procedure for doing the measurement, and highlights the importance of understanding the detector acceptance. Future measurements, with higher statistics, should be able to distinguish among P^2 suppression models and extract a virtual photon structure function, following the same general procedure described in [31] for the real photon structure function.

The measurement proceeds in two steps. In the first step, the luminosity of the data sample is determined, signal events are selected, and backgrounds are estimated. From these measured quantities, an accepted cross section σ_{acc} is extracted. In the second step, σ_{acc} is corrected to a full cross section,

$\sigma(\overline{Q^2}, \overline{P^2})$, with $W > W_{\mathrm{min}}$.

5.2 Doubly Tagged Event Selection

The signature for a doubly tagged hadronic two-photon event is two large electro-magnetic energy clusters from the tags and several tracks from the hadronic final state. The following criteria, listed in Table 5.1, are used to select doubly tagged events for this analysis:

- The first two cuts select a tag in the clean acceptance of either the Silicon-Tungsten Luminometer or the Forward Detector.

- The second pair of cuts selects a set of tracks consistent with a hadronic final state. The variables N_{ct} and N_{tfc} are, respectively, the number of charged tracks and the number of charged tracks originating from photon conversions in the event. The requirement of more than two charged tracks not coming from photon conversions eliminates background from $e^+e^- \to e^+e^-e^+e^-$ and $e^+e^- \to e^+e^-\mu^+\mu^-$ and reduces the background from $e^+e^- \to e^+e^-\tau^+\tau^-$. The remaining $e^+e^- \to e^+e^-\tau^+\tau^-$ contribution is an irreducible background. W_{vis} is the reconstructed invariant mass of the hadronic final state. The upper cut removes backgrounds from annihilation events and the lower cut removes possible two-photon resonance production.

- The last pair of cuts selects a tag only in an FFM module. The cut on $\mathrm{Y}_{\mathrm{asym}}$ is a fiducial volume cut, and it's effect will be discussed in Section 5.3.

After the cuts on the SW-FD tag and hadronic system are applied, 2275 events are selected. Applying the additional FFM tag cuts, 7 events are

$0.035 < \theta_{\mathrm{Tag}} < 0.055$ or $0.060 < \theta_{\mathrm{Tag}} < 0.120$ radians
$0.75 * E^{\mathrm{Beam}} < E^{\mathrm{Tag}}$
$N_{\mathrm{ct}} - N_{\mathrm{tfc}} > 2$
$2.5 < W_{vis} < 40$ GeV
$0.75 * E^{\mathrm{Beam}} < E^{\mathrm{Tag2}}_{\mathrm{FFM}}$
$\lvert \mathrm{Y}_{\mathrm{asym}} \rvert < 0.9$

Tab. 5.1: Event Selection Cuts

selected.

Because of the high machine background rates discussed in Section 4.8, only the data from some of the FFMs can be used in the doubly tagged analysis. Table 5.2 shows the OPAL period number, the integrated luminosity and which FFM module data is used for the analysis. The acceptance for periods with different numbers of useable modules is different, but to simplify the analysis, the luminosity will be reweighted and the acceptance taken to be constant. The luminosity used for the analysis is the equivalent luminosity for a single module, defined as the number of useable modules times the luminosity for that period. The acceptance correction is performed as though there is only one module. The equivalent luminosity for this analysis is 73.49 pb^{-1}.

5.3 Background Estimate

Two sources of background are considered in this analysis; backgrounds arising from the overlap of a singly tagged two-photon event and a cluster from machine background in an FFM module, and background arising from gen-

OPAL Period	L (pb^{-1})	Useable FFM Modules	Equivalent L
85	7.43	RN LF	14.86
86	23.03	LF	23.03
88	14.39	RN LF	28.78
89	3.41	RN LF	6.82
Total	48.26	-	73.49

Tab. 5.2: Luminosity

uine beam-beam interactions.

The background from overlap events can be estimated by looking at the number of events selected with the two tags on the same end of OPAL versus the number of events selected with the tags on opposite ends of OPAL. Overlap events should occur with same end tags and with opposite end tags with equal frequency, since the FFM tag is uncorrelated with the singly tagged overlap event. The number of same end tagged events thus estimates the number of opposite end tagged overlap events. In the selected sample, there is one same end tagged event. This means that there are six events consistent with the doubly tagged signature (tags at opposite ends of OPAL), with an estimated background of one event. Subtracting this background event, the measured number of doubly tagged events is 5.00 ± 2.45.

In order to estimate the background from genuine physics processes, the analysis was applied to Monte Carlo samples of $e^+e^- \to W^+W^-$, $e^+e^- \to q\overline{q}$, and $e^+e^- \to e^+e^-\tau^+\tau^-$. No events were selected for the W pair and quark pair samples in, respectively, 3.28 fb^{-1} and 4.65 fb^{-1} of simulated data. For the $e^+e^- \to e^+e^-\tau^+\tau^-$ channel, 28 events were selected in 4.0 fb^{-1}, yielding an estimated background of 0.6 ± 0.11 events to be subtracted from the measured number of events.

The measured number of events after physics background subtraction is 4.4 ± 2.45. Using the reweighted luminosity of 73.49 pb^{-1}, this translates to a cross section ($\sigma_{\mathrm{accepted}}$) of 0.060 ± 0.038 pb, which will be corrected for detector acceptance in order to allow a direct comparison with theoretical predictions and other experiments.

5.4 Acceptance Correction

In order to extract a measurement which is independent of the tagging detector configuration, a correction for the geometrical acceptance of the tagging detectors is necessary. For this measurement, two correction factors are needed, as given in Equation 5.1. The correction factor f_{c1} corrects the high angle tag acceptance in SW and FD, which covers the full range of ϕ both before and after correction, from the two ranges of tag angle which have clean acceptance ($0.035 < \theta_{\mathrm{tag}} < 0.055$ and $0.060 < \theta_{\mathrm{tag}} < 0.120$) to a continous range of theta ($0.035 < \theta_{\mathrm{tag}} < 0.120$). The correction factor f_{c2} corrects the low angle tag acceptance in the FFMs. The initial region is the complicated region shown in Figure 5.1 which is corrected to the region $0.0048 < \theta_{\mathrm{tag}} < 0.0068$, $-\pi < \phi < \pi$, $E_{\mathrm{tag}} > 0.75\ E_{\mathrm{beam}}$.

$$\sigma_{\mathrm{corrected}} = \frac{\sigma_{\mathrm{accepted}}}{f_{\mathrm{c1}} f_{\mathrm{c2}}} \tag{5.1}$$

The calculation of the acceptance factors is done by factorizing the angular dependence and overall normalization of the cross section for $e^+e^- \to e^+e^- +$ Hadrons. In essence, this allows the use of QED to predict the angular distribution of tags, without making assumptions about the size of the overall cross section. Using this factorization, an extrapolation can be made from the angular region covered by the tagging detector to the desired angular region. This sort of factorization is one of the assumptions of the Equivalent Photon Approximation (EPA), as discussed in Chapter 2. It is important to check that the expected P^2 suppression over the range of acceptance of the FFMs does not spoil the factorization. Using the DrGo suppression model, the expected supresion for the minimum accepted P^2 is 92.7%, while for the maximum accepted P^2 it is 86.4%. The maximum error induced by disregarding P^2 suppression over the acceptance of the detector is 6.3%, which is much smaller than the statistical error of this measurement and will be neglected.

The differential form of the EPA is

$$\mathrm{d}\sigma_{e^+e^-\to e^+e^-X}(s) = \mathrm{d}n_1\ \mathrm{d}n_2\ \mathrm{d}\sigma_{\gamma\gamma\to X}(W^2) \tag{5.2}$$

with s the center of mass energy squared of the colliding electrons and W the invariant mass of the produced hadronic system. The differentials $\mathrm{d}n_1$ and $\mathrm{d}n_2$ are the number of tags in a given range of angle and energy; neglecting the electron mass

$$\mathrm{d}n_i = \frac{2\alpha}{\pi}\left[1 - \frac{\omega_i}{E_i} + \frac{\omega_i^2}{2E_i^2}\right]\frac{\mathrm{d}\omega_i}{\omega_i}\frac{\mathrm{d}\theta_i}{\theta_i} \tag{5.3}$$

where ω_i is the energy of the emitted photon and θ_i is the scattering angle of the electron. Integrating Equation 5.2 yields the cross section for two photon scattering for a particular range of the kinematic variables.

The acceptance correction is the ratio of the cross section for $\sigma_{e^+e^-\to e^+e^-X}(s)$ for the acceptance of the detector to some other range of the kinematic variables. The new range of the kinematic variables should be chosen to be close to the old one in θ, ω, and W in order to avoid large extrapolations.

$$
\begin{aligned}
f_{\mathrm{c}} &= \frac{\sigma_{e^+e^-\to e^+e^-X}(s)}{\sigma'_{e^+e^-\to e^+e^-X}(s)} && (5.4)\\
&= \frac{\int_A \mathrm{d}n_1 \int_B \mathrm{d}n_2 \int_C \mathrm{d}\sigma_{\gamma\gamma\to X}}{\int_{A'} \mathrm{d}n_1 \int_{B'} \mathrm{d}n_2 \int_{C'} \mathrm{d}\sigma_{\gamma\gamma\to X}} && (5.5)\\
&= \frac{\int_A \mathrm{d}n_1}{\int_{A'} \mathrm{d}n_1} && (5.6)
\end{aligned}
$$

In Equation 5.4 through Equation 5.5, the σ represent cross sections, the variables A, B, C and A', B', C' are integration regions in kinematic variable space, and the $\mathrm{d}n$ variables are defined in Chapter 2.

Equation 5.4 through Equation 5.6 show the derivation of the acceptance correction factor. In going from Equation 5.4 to Equation 5.5, the cross sections are rewritten using the EPA. In going from Equation 5.5 to Equation 5.6, we specialize to the case where the regions of integration for the second tag, the hadronic final state, and the first tag energy are the same before and after correction, as is the case for the corrections used here.

Rewriting Equation 5.3 in a form which explicitly includes the ϕ dependence yields

$$n = \int \mathrm{d}\phi \int \frac{\mathrm{d}\theta}{\theta} \int \frac{\mathrm{d}\omega}{\omega} \frac{\alpha}{\pi^2} \left[1 - \frac{\omega}{E_{\mathrm{Beam}}} + \frac{\omega^2}{2E_{\mathrm{Beam}}^2} \right] \tag{5.7}$$

for the number of tags in a range of energy and angle. The energy cutoff used for the detector and for the corrected result are the same, and the region of $\theta - \phi$ space for the corrected result goes from $-\pi$ to π in ϕ and is bounded by lines of constant θ. For a correction to this rectangular region in $\theta - \phi$ space, an acceptance correction factor has the form

$$f_{\mathrm{c}} = \frac{\int_{\phi_{\mathrm{lower}}}^{\phi_{\mathrm{upper}}} \mathrm{d}\phi \int_{\theta_{\mathrm{lower}}(\phi)}^{\theta_{\mathrm{upper}}(\phi)} \frac{\mathrm{d}\theta}{\theta}}{\int_0^{2\pi} \mathrm{d}\phi \int_{\theta_{\mathrm{min}}}^{\theta_{\mathrm{max}}} \frac{\mathrm{d}\theta}{\theta}} \tag{5.8}$$

$$= \frac{\int_{\phi_{\mathrm{lower}}}^{\phi_{\mathrm{upper}}} \mathrm{d}\phi \ln \frac{\theta_{\mathrm{upper}}(\phi)}{\theta_{\mathrm{lower}}(\phi)}}{2\pi \ln \frac{\theta_{\mathrm{max}}}{\theta_{\mathrm{min}}}} \tag{5.9}$$

This expression can be evaluated numerically, if the functions $\theta_{\mathrm{upper}}(\phi)$ and $\theta_{\mathrm{lower}}(\phi)$ are known.

The factor f_{c1} is a relatively small correction for the region between 55 and 60 mrad which is removed by the angular acceptance cuts for the high angle tag. The ratio of the cross section for the range 0.035 to 0.055 plus 0.060 to 0.120 radians to the full cross section for 0.035 to 0.120 radians is 0.931, giving f_{c1}.

The second correction is much larger, and is required to correct for the acceptance of the FFMs. The acceptance for one monitor, at the nominal position, is shown in Figure 5.1. The top plots shows the full acceptance of the monitor in θ and ϕ, while the bottom plot shows the acceptance after the $|\mathrm{Y}_{\mathrm{asym}}| < 0.9$ cut is made. This cut is used to reduce the size of the acceptance correction. Because of the shape of the detector, the effects of the quadrupole, and the shadowing caused by the beam pipe, the acceptance is a complicated function of θ and ϕ. As shown by the lines in Figure 5.1, a relatively simple model of the acceptance is adequate, however. The acceptance is bounded above and below by parabolas, and on the edges by lines of constant phi. Figure 5.2 shows the acceptance for variations of the position of the detector and beam pipe in the Monte Carlo model.

$$\theta_{\mathrm{upper}} = a^2_{\mathrm{upper}}(\phi^2 - \phi^2_{\mathrm{max}}) + \theta_{\mathrm{max}} \tag{5.10}$$

$$\theta_{\mathrm{lower}} = a^2_{\mathrm{lower}}\phi^2 + \theta_{\mathrm{min}} \tag{5.11}$$

The equations for $\theta_{\mathrm{upper}(\phi)}$ and $\theta_{\mathrm{lower}(\phi)}$ needed to calculate f_{c2} take the form shown in Equation 5.10 and Equation 5.11. The parameters for these equations for each of the systematic variations are shown in Table 5.4, and the variations used are shown in Table 5.3.

5.5 Result

Using Equation 5.1 to calculate the final cross section, and taking the largest changes in the calculated cross section using the values in Table 5.4 as the systematic error, the measured cross section is

$$\sigma(\overline{Q^2}, \overline{P^2},\ W > W_{\mathrm{min}}) = 1.39 \pm 0.77\ (\mathrm{stat})\ \ \pm^{0.18}_{0.14}\ \ (\mathrm{syst})\ \mathrm{pb}$$

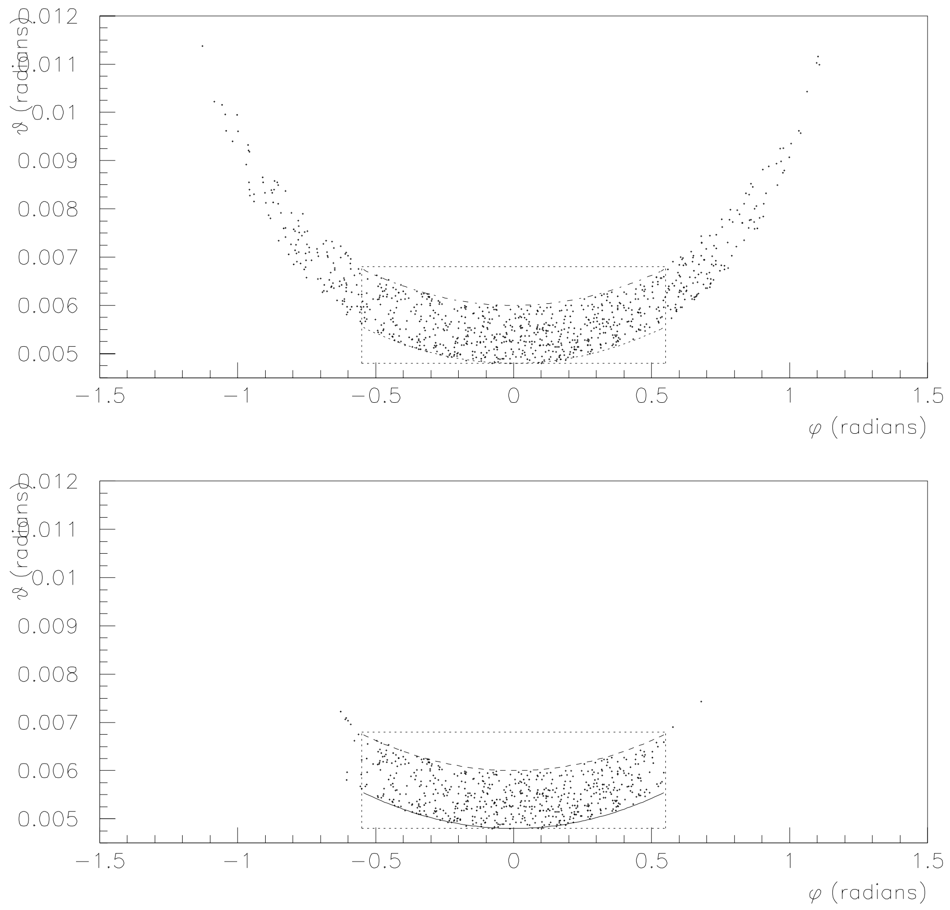

Fig. 5.1: Monte Carlo distribution of Bhabha hits in θ and ϕ for one module, without and with the $|\mathrm{Y}_{\mathrm{asym}}| < 0.9$ cut. The rectangular region outlined by dotted lines shows the area used in calculating the acceptance correction. The horizontal dotted lines indicate θ_{min} and θ_{max} and the vertical dotted lines indicate ϕ_{min} and ϕ_{max}. The parabolas are $\theta_{\mathrm{upper}}(\phi)$ and $\theta_{\mathrm{lower}}(\phi)$. Because these distributions are derived from a simulation which includes showering in material near the detector, it is possible for electrons which would not otherwise fall into the detector acceptance to be scattered into the acceptance. This effect produces the points outside the box in the lower plot.

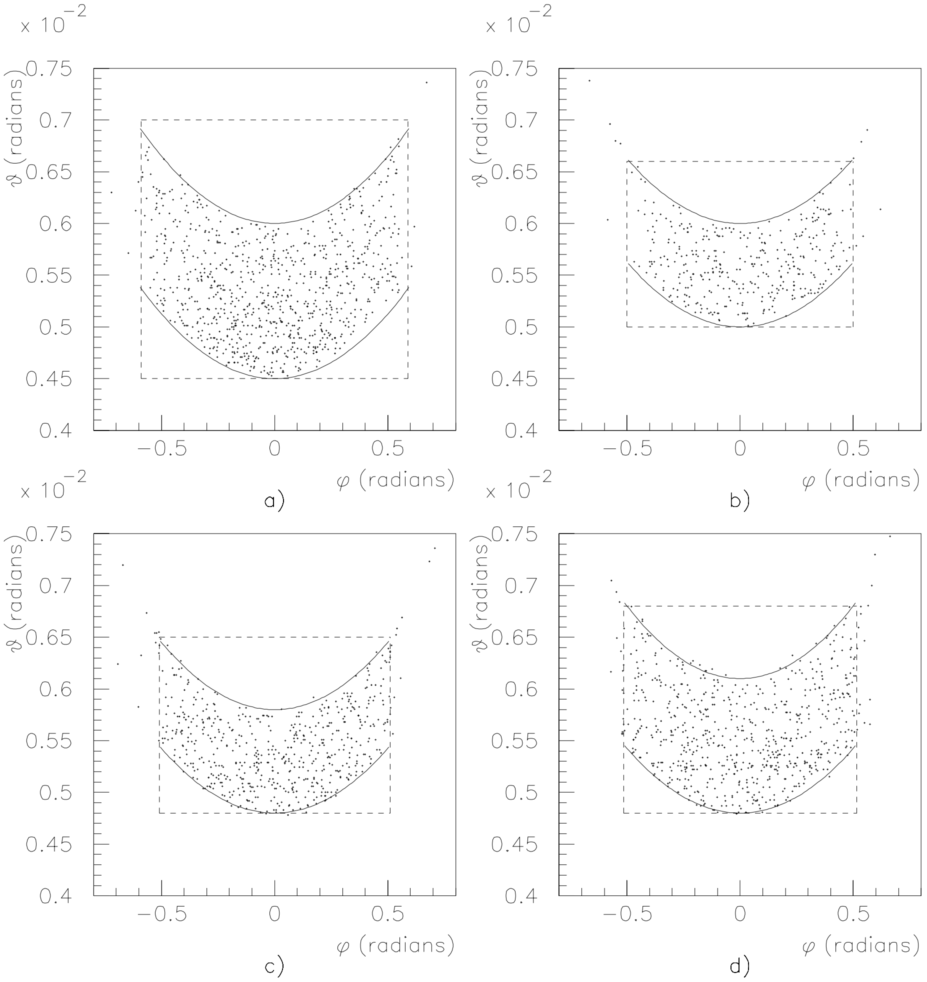

Fig. 5.2: Monte Carlo distribution of Bhabha hits in θ and ϕ for one module, for the variations in detector position given by the errors on the detector position.

Var #	x_{ff}	$x_{\text{beam pipe}}$
nominal	59 mm	7.5 mm
1	56 mm	7.5 mm
2	62 mm	7.5 mm
3	59 mm	9.5 mm
4	59 mm	5.5 mm

Tab. 5.3: Definition of Systematic Error Variations for the FFM acceptance correction factor.

Var #	θ_{min}	θ_{max}	ϕ_{min}	ϕ_{max}	a_{lower}	a_{upper}	f_{c2}
nominal	0.0048	0.0068	-0.55	0.55	0.050	0.050	0.0554
1	0.0045	0.0070	-0.59	0.59	0.050	0.051	0.0619
2	0.0050	0.0066	-0.50	0.50	0.050	0.050	0.0493
3	0.0048	0.0065	-0.51	0.51	0.050	0.051	0.0505
4	0.0048	0.0068	-0.515	0.515	0.050	0.053	0.0544

Tab. 5.4: Result of Systematic Error Variations for the FFM acceptance correction factor. Angles are given in radians, and a_{lower} and a_{upper} are defined in Equation 5.11 and Equation 5.10.

Structure Function	Suppression Model	$\sigma(\overline{Q^2}, \overline{P^2}), W > W_{\mathrm{min}}$
Data	-	1.39 ± 0.77 (stat) $\pm^{0.18}_{0.14}$ (syst) pb
GRV	DrGo [16]	1.46 ± 0.03 pb

Tab. 5.5: Comparison of data and Monte Carlo results. $\overline{Q}^2$ is 20.4 GeV^2, $\overline{P}^2$ is 0.27 GeV^2, and W_{min} is 2.5 GeV. The measured value is in agreement with the value predicted by Monte Carlo.

with $\overline{Q}^2 = 20.4$ GeV^2, $\overline{P}^2 = 0.27$ GeV^2, and $W_{\mathrm{min}} = 2.5$ GeV. The mean Q^2 and P^2 values were obtained using a Monte Carlo model of the EPA to simulate the corrected acceptance range.

This measured cross section has been compared to the results of a Monte Carlo simulation using Phojet version 1.10. The process has been observed with approximately the expected cross section. For future analyses, Phojet can be used with different models and structure functions in order to calculate $\sigma(e^+e^- \to e^+e^- + \text{Hadrons})$, allowing a direct comparison between the measured cross section and the cross sections predicted by theory.

6. CONCLUSIONS

This thesis documents the first attempt to use the OPAL Far Forward Monitor system for a physics analysis.

In the course of the analysis, a number of faults were discovered and corrected. These faults were based on incorrect wiring of the PMT bases and failure of the light guide components. The PMT bases were rewired and new lightguides were fabricated, using more robust materials. In addition, an LED test pulse system was installed to allow testing of the FFM modules, both before and after installation.

Detector Simulation software was written using the GEANT package, and tuned to the data. Energy calibration software was also written, based on minimizing the width of the Bhabha distribution observed by the FFMs. Position reconstruction software was created, based on energy sharing between the different FFM compartments.

Machine backgrounds were studied and found to have the qualitative features described by the TURTLE beamline simulation package. These backgrounds originate from particles losing energy due to beam-gas interactions. The background particles which most affect the doubly tagged $\gamma\gamma$ analysis are those which have lost only a small amount of energy. These come from the beginning of the LEP arcs where the vacuum pressure is expected to be higher than in the straight sections.

In order to improve shower position reconstruction and thus better control systematic errors, a detector upgrade was undertaken, This upgrade included rebuilding the PMT bases to reduce crosstalk, adding survey points to the detector, performing a survey, and adding shower position measurement to the detector using scintillating fingers with wavelength shifting fiber optic readout. With the upgraded detector, the determination of systematic errors will be more straightforward because of built-in crosschecks on the detector positions.

Using the 1997 data, the cross section for DIS of an electron from a virtual photon target was measured. Because of the difficulties with machine backgrounds, the statistical error is large. The final result is

$$\sigma(\overline{Q^2}, \overline{P^2},\ W > W_{\mathrm{min}}) = 1.39 \pm 0.77\ (\mathrm{stat})\ \pm^{0.18}_{0.14}\ (\mathrm{syst})\ \mathrm{pb}$$

with $\overline{Q}^2 = 20.4$ GeV^2, $\overline{P}^2 = 0.27$ GeV^2, and $W_{\mathrm{min}} = 2.5$ GeV.

Assuming a luminosity of 350 pb^{-1} for the remainder of LEP running and taking the measured cross section, plus a 20% increase in statistics due to changes in the beam pipe configuration, $\sim$ 100 events are expected for the final OPAL FF-SW/FD doubly tagged sample. This will allow a measurement with 10% statistical error. With the upgraded detector, the systematic error can be reduced below this level. As discussed in Chapter 2, there are differences of up to 30% between predictions for the P^2 dependence of the hadronic structure function in this region of $\overline{Q}^2$ and $\overline{P}^2$. Given the results of this thesis, the prospects are good for a measurement of the virtuality suppression which will choose between available models.

APPENDIX

A. PAPER PRESENTED AT CHEP '97

A compilation and analysis of the data management and computing in the OPAL experiment, 1989 to 1996.

J. Baudot [a], C. Bondila [a], D. Charlton [b], D. Deatrich [c],
L. del Pozo [d]. J. Letts [c], E. McKigney [e], S. O'Neale [b],
M. Schröder [a], A. Williamson [f]

[a] *CERN, CH 1211 Geneva 23, Switzerland*
[b] *University of Birmingham, Birmingham B15 2TT, United Kingdom*
[c] *Indiana University, Bloomington, Indiana 47405, USA*
[d] *University of California, Riverside, California 92521, USA*
[e] *University College London, London WC1E 6BT, United Kingdom*
[f] *University of Alberta, Edmonton AB T6G 2N5, Canada*

We present a quantitative review of data collection, reconstruction, simulation and analysis in the OPAL collaboration. The evolution of the sample sizes, code and computing resources will be presented. The present system will be analysed with modern tools for modelling and metrics which are now available. [a]

---

[a] More details can be found at http://opalinfo.cern.ch/Opal/offline.html

Key words: OPAL; batch; interactive service; SHIFT; Monte Carlo; code management

1 The Data Flow

In OPAL, the data reconstruction and analysis computers are closely integrated with the data acquisition system [1]. Events are first recorded on disk at the filter [2], which is composed of a cluster of VME-based HP-UX workstations. At all stages, subsequent data transfers take place over local area networks (LAN) using disk buffers and permanent storage, which allows almost complete automation of the dataflow chain.

The compressed raw data is written to optical disks loaded into jukeboxes at the experiment. As well, it is written to tapes in the CERN computer cen-

Year	1990	1991	1992	1993	1994	1995	1996
Int. Lumi. / pb^{-1}	7	14	25	33	58	33 [6]	1 [20]
Events / 10^6	4.0	9.0	15.0	21.3	27.4	21.0 [2.7]	1.6 [8.4]
Hadronic events / 10^6	0.15	0.35	0.77	0.72	1.62	0.74	0.03
Raw Data size / GB	59	96	186	333	406	338 [50]	39 [200]
[D]DST size / GB	6.2	15.2	32.7	59.3	93.7	63	[88]
SHIFT Disk Space / GB	20	100	190	340	680	880	1100

Table 1
Number of events and sample sizes. Values in [] for running above the Z

tre over the LAN. A workstation farm at the experimental site reconstructs the raw data as it is collected, using the OPAL standard reconstruction program ROPE. This “Rope farm” consists of HP PA-RISC workstations. When the farm is not being used for reconstruction, it participates in Monte Carlo Production. There are currently 14 CPUs, with a capacity of 375 CERN units.

After a loose physics selection the DSTs are transferred over the LAN to the CERN computer centre, where they are recorded permanently on a large disk array in the SHIFT system[3]. These data are also backed up on magnetic tape media in the CERN computer centre. The data is accessible for the users about two hours after it has been collected. In general the data is not exported to outside institutes.

2 SHIFT - Scalable Heterogeneous Integrated Facility

Essentially all subsequent analyses of the data are performed on the SHIFT batch system, developped by an OPAL/CN collaboration. This system consists of two SGI Challenge XLs, providing 780 CERN Units of computing power and over 1 TB of disk storage. Files are mounted with NFS and read via RFIO.

Data from the highest reconstruction pass for each year and popular Monte Carlo samples are stored on disk. All other data are stored on tapes and catalogued by Fatmen. User analyses typically proceed by passing through the full DST data sample, producing ntuples or micro-DST summaries for further study. The permanent storage of the DST data on disk allows the analyses to proceed efficiently by directly accessing specific events using lists of file offsets (dadlists). Users can also make their own dadlists whenever appropriate, reducing the I/O and CPU needs for the analysis jobs.

SHIFT uses a modified version of NQS as batch system. Among the additional features added are dynamic load balancing and queue ordering. Jobs can be submitted from within CERN (80%) and from remote sites outside of CERN (20%), with log files returning to the original site, and other output files wherever specified. A project to test LSF as an NQS replacement is under

Year	1991	1992	1993	1994	1995	1996
CERN Units in SnOPAL			92.8	243.7	418.7	737.7
Events from OPAL workstations	583748	1166491	1376634	3078492	7233124	11336976
Events from central facilities	199133	440383	1577264	2871995	2855856	3973298
Events from outside CERN	337642	550156	568452	1555783	6607794	5319079

Table 2
Monte Carlo production : SnOPAL capacity and number of events produced

way.

3 Interactive Services

OPAL uses a cluster of HP workstations, called SnOPAL ("Snakes on OPAL") for most of the interactive work and some batch jobs with little network I/O. Free CPU capacity is used for Monte Carlo Production.

The cluster has two boot node/file servers, which provide redundant copies of user applications. Because of the importance of stability for the Monte Carlo Production, the cluster is constructed in such a way that all nodes can continue running Monte Carlo jobs, even if both boot nodes are down. It is not possible to use the nodes interactively while the bootnodes are down, however, because some critical software is served.

There are currently 90 workstations in the cluster, of which 46 are used for Monte Carlo Production, the CERN Units shown in table 2 apply only to these.

IT Division is developing an "interactive benchmark" to model the typical interactive load on the CERN Work Group and Public Login Unix Servers. This model has been used to analyse the OPAL users profile on HPPLUS.

The readily available Unix accounting data is taken as the starting point for the model. The model groups commands into a small number of classes and an analysis of usage patterns for a 5 weeks period on HPPLUS shows three different categories of usage for OPAL. We interpret these as physics analyses, general usage and idle users. As a comparison, the ATLAS user analysis identifies a fourth category of usage, code development.

The differences in the usage between ATLAS and OPAL users are probably due to the fact that most OPAL users have accounts on SnOPAL, where they do the more CPU intensive tasks and code development.

Users/Server	Gen. Activ.	Idle	Analyses	Code Dev.
ATLAS/ATLAS_WGS	65%	12%	15%	8%
OPAL/HPPLUS	76%	16%	8%	-

Table 3
The proportion of users found in different categories

4 The Monte Carlo Production

The OPAL Monte-Carlo Production (MCP) system [4] is designed to manage the processing of generated events through the OPAL simulation package. It is organised around a central process which generates and distributes computing jobs to exploit free cycles on SnOPAL CPUs or the ROPE farm and dedicated simulation facilities. DDST generated offsite are shipped on DAT or DLT as international network bandwidth is inadequate for such transfers.

The control system was developed in Rexx. In 96 it has been moved to UNIX, and is now implemented in PERL. A WWW interface is used to get the physics needs and to provide documentation about the production status.

Whereas the system performs well, it has become quite complicated and inhomogeneous due to its development on different architectures with different languages. An attempt to re-design the system using object oriented modelling techniques (Booch-OMT) and a graphical tool (StP) has started.

5 The Code Management

OPAL created coding conventions early on for all reconstruction and analysis software. The purpose of these conventions is to ensure strict FORTRAN77 compliance, except for a mandatory 'IMPLICIT NONE' and MIL bit functions. Such conventions ensure that OPAL software works properly on all supported platforms.

The standard compliance of the code is verified by using compiler options and ftnchek on HPPLUS. Additional testing of the software is done on an SGI machine, with the help of compiler options for debugging. Recently we have started to use logiscope for measuring the quality of our code and identifying routines which might be difficult to test or maintain.

References

[1] J.T.M. Baines et al., Nuclear Instrum. and Meth. A325 (1993) 271-293

[2] D.G. Charlton, F. Meijers, T.J. Smith, P.S. Wells, Nuclear Instrum. and Meth. A325 (1993) 129-141

[3] B. Panzer, CHEP92, p. 483

[4] S. O'Neale, CHEP92, p. 471

BIBLIOGRAPHY

[1] G. Breit and J. A. Wheeler. Collision of two light quanta. *Physical Review*, 46:1087–1091, 1934.

[2] C. Bamber The E-144 Collaboration et al. Positron production in multiphoton light-by-light scattering. *Physical Review Letters*, 79(9):1626–1629, 1997.

[3] S. J. Maxfield. *A First Measurement of the Virtual Photon Structure Function.* PhD thesis, University of Maryland, 1985.

[4] The PLUTO Collaboration, C. Berger et al. Measurement of deep inelastic electron scattering off virtual photons. *Physics Letters B*, 142:119–124, 1984.

[5] R. J. Belcinski. *A Measurement of the Virtual Photon Structure Function.* PhD thesis, University of Massachusetts, Amherst, 1994.

[6] V.M. Budnev, I.F. Ginzburg, G.V. Meledin, and V.G. Serbo. The two-photon particle production mechanism. physical problems. applications. equivalent photon approximation. *Physics Reports*, 15(4):181–282, 1975.

[7] Particle Data Group. Review of particle physics. *Physical Review D*, 54(1):1–720, July 1996.

[8] Ch. Berger and W. Wagner. Photon photon reactions. *Physics Reports*, 146(1):1–134, 1986.

[9] M. Glück, E. Reya, and A. Vogt. Photonic parton distributions. *Physical Review D*, 46(5):1973–1979, September 1992.

[10] Gerhard A. Schuler and Torbjörn Sjöstrand. Low- and high-mass components of the photon distribution functions. *Zeitschrift Für Physik C*, 68:607–623, 1995.

[11] Francis Halzen and Alan D. Martin. *Quarks and Leptons.* John Wiley and Sons, New York, 1984.

[12] R. K. Ellis, W. J. Stirling, and B.R. Webber. *QCD and Collider Physics.* Cambridge University Press, Cambridge, 1996.

[13] C. T. Hill and G. G. Ross. QCD prediction for the structure functions of the photon. *Nuclear Physics*, B148:373–399, 1979.

[14] M. Glück, E. Reya, and M. Stratmann. Parton content of virtual photons. *Physical Review D*, 51(7):3220–3229, April 1995.

[15] Gerhard A. Schuler and Torbjörn Sjöstrand. Parton distributions of the virtual photon. *Physics Letters B*, 376:193–200, 1996.

[16] M. Drees and R. M. Godbole. Virtual photon structure functions and the parton content of the electron. *Physical Review D*, 50(5):3124–3133, 1994.

[17] Stephen Myers. The LEP collider from design to approval and commissioning. The John Adams Memorial Lecture, CERN, November 1990. http://www.cern.ch/CERN/Divisions/SL/history/lep_doc.html.

[18] The OPAL Collaboration. The OPAL detector at LEP. *Nuclear Instruments Methods in Physics Research*, A305(2):275–319, 1991.

[19] M. Arignon et al. The trigger system of the OPAL experiment at LEP. *Nuclear Instruments Methods in Physics Research*, A313(1-2):103–125, 1992.

[20] LeCroy Research Systems Corporation. *Catalog*, 1985.

[21] W. R. Leo. *Techniques for Nuclear and Particle Physics Experiments.* Springer-Verlag, Heidelberg, 1987.

[22] CERN, Geneva, Switzerland. *GEANT - Detector Description and Simulation Tool*, 1993.

[23] Ph. Lebrun, S. Pichler, T.M. Taylor, T. Tortschanoff, and L. Walckiers. Design, test and performance of the prototype superconducting quadrupole for the LEP low-beta insertions. In *Proceedings of the 10th International Conference on Magnet Technology*, September 1987.

[24] Helmut Wiedemann. *Particle Accelerator Physics*. Springer-Verlag, New York, 1993.

[25] W. R. Leo. *Introduction to experimental particle physics.* Cambridge University Press, Cambridge, 1986.

[26] S. Jadach, W. Placzek, E. Richter-Was, B.F.L. Ward, and Z. Was. Upgrade of the monte carlo program BHLUMI for Bhabha scattering at low angles to version 4.04. *Computer Physics Communications*, 102:229–251, 1997.

[27] CERN, Geneva, Switzerland. *MINUIT - Function Minimization and Error Analysis*, 1994.

[28] K.L. Brown and C. Iselin. *DECAY TURTLE, a Computer Program for Simulating Charged Particle Beam Transport Systems, including Decay Calculations.* CERN, 1974. 74-2.

[29] R.Hawkings, F.W.Jones, J.Pinfold, and J.S.Rogers. Beamspots, bunchlets, bananas and boms : Studies of the beamspot in 1995 opal data. OPAL Technical Note 372, The OPAL Collaboration, April 1996.

[30] The SiW Group. Precision luminosity for Z^0 lineshape measurements with the opal silicon-tungsten luminometer. OPAL Technical Note 528, The OPAL Collaboration, December 1997.

[31] The OPAL Collaboration, K. Ackerstaff et al. Analysis of hadronic final states and the photon structure function F_2^γ in deep inelastic electron-photon scattering at LEP. *Zeitschrift Für Physik C*, 74:33–48, 1997.

[32] Sun Myong Kim and Thomas F. Walsh. Moments of the virtual photon structure function. *Zeitschrift Für Physik C*, 72:123–131, 1996.

[33] The OPAL Collaboration, K. Ackerstaff et al. Measurement of the Q^2 evolution of the photon structure function F_2^γ. *Physics Letters B*, 411:387–401, 1997.

[34] David Edward Goldberg. *Genetic Algorithms in Search, Optimization, and Machine Learning.* Addison-Wesley, Reading, Mass., 1989.

[35] Argonne National Laboratory, 9700 South Cass Avenue, Argonne, IL 60439, USA. *Users Guide to the PGAPack Parallel Genetic Algorithm Library*, 1995.

[36] M. Glück, E. Reya, and M. Stratmann. Parton content of virtual photons. *Physical Review D*, 51(7):3220–3229, 1995.

[37] Gerhard A. Schuler and Torbjörn Sjöstrand. A scenario for high-energy gamma gamma interactions. *Zeitschrift Für Physik C*, 73(4):677–688, 1997.

[38] J. D. Bjorken. Asymptotic sum rules at infinite momentum. *Physical Review*, 179(5):1546–1553, 1969.

[39] M. Glück, E. Reya, and A. Vogt. Radiatively generated hadronic photon structure at low q^2. *Physics Letters B*, 222(1):149–51, 1989.

[40] S. J. Brodsky, F. Hautmann, and D. E. Soper. Virtual photon scattering at high energies as a probe of the short distance pomeron. *Physical Review D*, 56(11):6957–6979, 1997.

[41] S.M. Kim and T. F. Walsh. Moments of the virtual photon structure function. *Zeitschrift Für Physik C*, 72(1):123–131, 1996.

[42] M. Arignon et al. The trigger system of the OPAL experiment at LEP. *Nuclear Instruments Methods in Physics Research*, A313:103–125, 1992.

[43] D. W. Duke and J. F. Owens. Quantum-chromodynamic corrections to deep-inelastic Compton scattering. *Physical Review D*, 26(7):1600–1609, 1982.

[44] H. Abramowicz, K. Charchula, and A. Levy. Parametrization of parton distributions in the photon. *Physics Letters B*, 269:458–464, 1991.

[45] R. Enomoto The TOPAZ Collaboration et al. Observation of highly virtual photon-photon collisions to hadrons at TRISTAN. *Physics Letters B*, 368:299–303, 1996.

[46] M. A. Ahmed and G. G. Ross. Deep inelastic photon-photon scattering in an asymptotically free gauge theory. *Physics Letters*, 59B(4):369–376, 1975.

[47] M. Glück, E. Reya, and A. Vogt. Parton structure of the photon beyond the leading order. *Physical Review D*, 45(11):3986–3994, 1992.

[48] M. Glück, E. Reya, and A. Vogt. Photonic parton distributions. *Physical Review D*, 46(5):1973–1979, 1992.

[49] E. Witten. Anomalous cross section for photon-photon scattering in gauge theories. *Nuclear Physics B*, 120:189–202, 1977.

[50] T. Uematsu and T. F. Walsh. Virtual photon structure to non-leading order in QCD. *Nuclear Physics B*, 199:93–118, 1982.

[51] T. Uematsu and T. F. Walsh. Virtual photon structure. *Physics Letters*, 101B(4):263–266, 1981.

[52] T. F. Walsh and P. Zerwas. Two-photon processes in the parton model. *Physics Letters*, 44B(2):195–198, 1973.

[53] T. F. Walsh and P. Zerwas. Scaling behaviour in off-shell photon-photon scattering. *Nuclear Physics B*, 41:551–556, 1972.

[54] G. Rossi. X-space analysis for the photon structure functions in QCD. *Physical Review D*, 29(5):852–868, 1984.

[55] C. D. Anderson. The positive electron. *Physical Review*, 43:491–494, 1933.

[56] P. Aurenche et al. The production of jets from quasi real photons in e^+e^- collisions. In *Workshop on Two-Photon Physics at LEP and HERA*, May 1994.